

CONVECTIVE BOILING HEAT TRANSFER IN A SINGLE MICRO-CHANNEL

THÈSE N° 4024 (2008)

PRÉSENTÉE LE 8 FÉVRIER 2008

À LA FACULTÉ DES SCIENCES ET TECHNIQUES DE L'INGÉNIEUR
LABORATOIRE DE TRANSFERT DE CHALEUR ET DE MASSE
PROGRAMME DOCTORAL EN MÉCANIQUE

ÉCOLE POLYTECHNIQUE FÉDÉRALE DE LAUSANNE

POUR L'OBTENTION DU GRADE DE DOCTEUR ÈS SCIENCE

PAR

Lorenzo CONSOLINI

M.Sc. in mechanical engineering, University of Illinois, Chicago, Etats-Unis
et de nationalité italienne

acceptée sur proposition du jury:

Prof. P. Monkewitz, président du jury
Prof. J. R. Thome, directeur de thèse
Prof. A. Cavallini, rapporteur
Prof. D. Favrat, rapporteur
Prof. G. Guglielmini, rapporteur



Suisse
2008

Acknowledgements

I would like to express my gratitude to all those people who contributed in different ways to this thesis. I am particularly grateful to my defense committee, Prof. Peter Monkewitz (EPFL), Prof. John R. Thome (EPFL), Prof. Alberto Cavallini (Università degli Studi di Padova, Italy), Prof. Daniel Favrat (EPFL), and Prof. Giovanni Guglielmini (Università degli Studi di Genova, Italy), for their valued comments and suggestions. My special appreciation goes to Prof. John R. Thome, who guided me in this study without imposing his personal viewpoint, but rather encouraging a fruitful discussion and debate. I would also like to acknowledge all the friends and colleagues who, at different stages, have participated in the life of LTCM during my doctoral course. Above all I would like to thank my family for their unremitting support during these years of hard work. Thank you all,

Lorenzo Consolini
January 2008

“An expert is a man who has made all the mistakes which can be made in a very narrow field.” Niels Bohr

Abstract

The current industrial need for compact high heat density cooling devices has conveyed an increasing interest on convective boiling in micro-channels. Although there is general agreement that these systems may be able to dissipate potentially very high heat fluxes, their heat transfer characteristics are still unclear and require investigation. The present study aims at providing further insight on two-phase single micro-channel heat transfer, through a sensitivity analysis on the effect of the different operational parameters, fluid properties, and channel size on thermal performance. The current database includes results for three different refrigerants, R-134a, R-236fa and R-245fa, two channel diameters, 510 and 790 μm , and a multitude of heat fluxes and mass velocities, for a total of over 1800 data points. Two-phase flow instability, which represents one of the factors that has prevented a well-established understanding of the micro-scale phenomenon, has been also investigated, with results showing the potential error it may induce on the estimation of the heat transfer coefficients. Finally, a one-dimensional analysis based on the effect of interfacial shear on the temporal evolution of film thickness is proposed for a heat transfer model for slug flow, which has been shown to be the dominant flow mode at low and intermediate vapor qualities in micro-channel evaporators.

Keywords: boiling, micro-channel, heat transfer, two-phase flows.

Version Abrégée

L'exigence actuelle de l'industrie pour des systèmes de contrôle thermique compacts et capables de dissiper des flux de chaleur toujours plus élevés, a développé l'intérêt d'explorer les possibilités d'utiliser l'ébullition en convection forcée dans des micro-canaux. Même si ces systèmes sont réputés pour leurs fortes dissipations thermiques, leurs caractéristiques de transfert de chaleur restent mal connues et demandent à être étudiées plus en détail. L'étude présente un large aperçu du transfert de chaleur biphasique dans un micro-canal, à travers une analyse des effets des différents paramètres opératifs, des propriétés du fluide, et de la taille du système sur les performances thermiques. La base de donnée comprend des résultats pour trois différents réfrigérants, R-134a, R-236fa et R-245fa, deux diamètres de tube, 510 et 790 μm , et plusieurs flux thermiques et débits, pour un total de 1800 points expérimentaux. En outre, une analyse des instabilités biphasiques, qui représentent un obstacle à la compréhension du phénomène microscopique, est aussi réalisée, avec des résultats qui montrent l'erreur associée dans l'estimation des coefficients d'échange thermique. Enfin, une description unidimensionnelle, basée sur l'effet de l'effort de cisaillement à l'interface liquide/vapeur sur l'évolution temporelle de la couche liquide, est proposée pour l'écoulement de type *slug*, qui se rencontre dans les micro-évaporateurs à titre de vapeur bas et intermédiaire.

Mot-clés: ébullition, micro-canal, transfert de chaleur, écoulements biphasiques.

Table of Contents

CHAPTER 1	1
INTRODUCTION	1
CHAPTER 2	3
OVERVIEW OF TWO-PHASE HEAT TRANSFER IN MICRO-CHANNELS	3
2.1 <i>Vapor Formation and Flow Development</i>	4
2.2 <i>Single-Channel Heat Transfer</i>	7
2.3 <i>Multi-Channel Heat Transfer</i>	9
2.4 <i>Two-Phase Oscillatory Instabilities in Micro-Channel Evaporators</i>	11
2.5 <i>Heat Transfer Prediction Methods</i>	15
2.6 <i>Conclusive Remarks</i>	23
CHAPTER 3	25
THE EXPERIMENTAL PROGRAM	25
3.1 <i>The Experimental Stand</i>	25
3.2 <i>The Test-Section</i>	26
3.3 <i>Data Reduction</i>	29
3.4 <i>Experimental Validation and Uncertainty</i>	32
CHAPTER 4	47
HEAT TRANSFER RESULTS AT STABLE TEST CONDITIONS	47
4.1 <i>Refrigerant Properties</i>	47
4.2 <i>Flow Boiling Curves</i>	48
4.3 <i>Micro-Channel Two-Phase Heat Transfer Data</i>	49
4.4 <i>Heat Transfer Predictions to the Experimental Data</i>	56
4.5 <i>Summary</i>	59
CHAPTER 5	61
HEAT TRANSFER WITH FLOW INSTABILITIES	61
5.1 <i>Temperature Fluctuations Associated to Compressible Volume Instabilities</i>	61
5.2 <i>Estimating Steady Heat Transfer Coefficients from Unstable Flows</i>	66
5.3 <i>Summary</i>	67
CHAPTER 6	69
ONE-DIMENSIONAL ANALYSIS OF CONFINED SLUG FLOW	69
6.1 <i>Dynamic Thin Film Evaporation</i>	69
6.2 <i>Liquid and Vapor Velocities at the Bubble Nose</i>	73
6.3 <i>Bubble Nose Velocity</i>	74
6.5 <i>Bubble Nose Position and Film Thickness</i>	75
6.5 <i>Liquid and Vapor Residence Times</i>	77
6.6 <i>Local Heat Transfer Coefficients</i>	78
6.7 <i>Heat Transfer Predictions to the Experimental Data</i>	82
CHAPTER 7	87
CONCLUSIONS	87

APPENDIX	89
MATHEMATICAL DESCRIPTION OF A COMPRESSIBLE VOLUME OSCILLATORY INSTABILITY .	89
CITED LITERATURE.....	95
VITAE	99

List of Figures

1. Bubble nucleation images (top view) from [17] at (a) 10, (b) 30, and (c) 70ms from the onset of boiling.....	4
2. Bubble departure frequency versus heat flux from [17] for de-ionized water in a trapezoidal channel with a $D_h = 41.3\mu\text{m}$, and (b) bubble passage frequency versus exit vapor quality for R-134a in a 0.5mm tube from [9].....	4
3. Bubbly, wavy, and annular vapor detachments from [18].....	5
4. Micro-channel flow patterns: (a) bubbly, (b) slug, (c) churn, and (d) annular flows.....	6
5. Flow pattern map by Chung and Kawaji [20] for a nitrogen-water flow in a $530\mu\text{m}$ circular micro-channels. Symbols: \circ – bubbly flow; ∇ – slug flow; \square – churn flow; \diamond – slug-annular flow; Δ – annular flow.....	6
6. Flow pattern map by Revellin and Thome [19]: ib – isolated bubble flow, cb – coalescing bubble flow, a – annular flow, pd – post dry-out flow. Values for a flow of R-134a at 30°C in a 0.5mm channel, 70mm in length, and a uniform heat flux of 50kW/m^2	7
7. Heat transfer data from (a) Lazarek and Black [5] for R-113 and (b) Bao <i>et al.</i> [26] for R-123.....	8
8. Heat transfer data from (a) Lin <i>et al.</i> [23] for R-141b in a 1.1mm channel and a mass velocity of $510\text{kg/m}^2\text{s}$, and (b) Saitoh <i>et al.</i> [28] for R-134a in a 0.51mm channel.....	8
9. Heat transfer data for (a) R-12 from Tran <i>et al.</i> [25] for different heat fluxes and mass velocities, with a wall superheat above 2.75°C , and (b) R-11 from Bao <i>et al.</i> [26] at a heat flux of 125kW/m^2 and a mass velocity of $560\text{kg/m}^2\text{s}$	9
10. A schematic diagram of the multi-channel test-section used in [30].....	10
11. Heat transfer data from (a) Yan and Lee [31] for R-134a at 31°C in 28 2mm parallel circular channels, at a mass velocity of $200\text{kg/m}^2\text{s}$, and (b) Lee and Mudawar [32] for R-134a in parallel rectangular micro-channels.....	11
12. Schematic model for the analysis of oscillatory instabilities.....	11
13. The internal and external characteristic curves for an evaporating flow at constant heat flux. The external characteristic is representative of a constant flow delivery system.....	12
14. Schematic representation of the boiling features occurring during one cycle of an oscillatory instability.....	13

15. Heat transfer data from (a) Xu <i>et al.</i> [30] for acetone in 10 triangular channels with a hydraulic diameter of 155.4 μ m, (b) Hetsroni <i>et al.</i> [37] for water in 21 parallel triangular micro-channels, and (c) Cortina Díaz and Schmidt [40] for water in a single rectangular channel with a hydraulic diameter of 0.59mm.....	14
16. The three-zone evaporation model.....	19
17. Predicted two-phase heat transfer coefficients. Values for R-134a at 7bar, with $q = 50\text{kW/m}^2$, $G = 500\text{kg/m}^2\text{s}$, in a $D = 0.5\text{mm}$ circular, stainless steel channel.....	21
18. Predicted heat transfer coefficients versus vapor quality at different (a) heat fluxes, (b) mass velocities, (c) channel diameters, and (d) saturation pressures.....	22
19. A schematic diagram of the experimental facility during data acquisition.....	25
20. A schematic diagram of the pumping loop for charging of vessel A.....	26
21. Schematic diagram of the flow boiling test-section showing the two pressure taps (p) at the inlet and exit, and the locations of the pre-heater (PH) and evaporator (EV) thermocouples.....	27
22. Magnified image of the open section of the 510 μ m micro-channel utilized for the measurement of inner roughness.....	29
23. One-dimensional radial heat conduction model to assess the tube-side temperature.....	30
24. Schematic of the system for the assessment of conductive heat losses.....	32
25. Axial wall temperature distribution as given by Eq. (3.18) for a flow of R-134a with a mass velocity of 500 $\text{kg/m}^2\text{s}$ and an inlet temperature of 31 $^{\circ}\text{C}$	34
26. Relative losses by conduction versus the tube Biot number, as predicted by Eq. (3.21).....	34
27. Single-phase heat balance for a sub-cooled liquid flow of R-134a in the 510 μ m tube.....	35
28. Single-phase Nusselt numbers for sub-cooled liquid flows of (a) R-134a, and (b) R-245fa in 510 μ m tubes. Data is compared to the Gnielinski and Dittus-Boelter correlations for $Re > 3000$, and conventional laminar flow theory for $Re < 2000$	36
29. Data for sub-cooled liquid R-134a flowing with a mass velocity of 1235 $\text{kg/m}^2\text{s}$ ($Re = 3200$), and an applied heat flux of 8.90 kW/m^2 : (a) inner wall temperature data and computed flow temperature, and (b) measured local heat transfer coefficients compared to conventional correlations.....	37
30. Graphical representation of the procedure for measuring temperatures from uncalibrated thermocouple readings. Note that $\delta T \leq \delta T_{\text{max}}$, for δT given by Eq. (3.30).....	38
31. Fractional uncertainty on the measured mass velocity for two tube sizes.....	40

32. Relative errors on (a) the heating efficiency and (b) the heat flux for flow boiling of R-134a in the 510 μ m channel, at a saturation temperature of 31°C and a mass velocity of 964kg/m ² s.....	41
33. The absolute uncertainty on the pressure at the inlet to the evaporator for a flow in the 510 μ m micro-channel. The step changes in the different curves correspond to laminar-turbulent transitions.....	43
34. The absolute error on local pressure for flow boiling of R-134a at 31°C in the 510 μ m channel with (a) a heat flux of 72kW/m ² , and (b) a mass velocity of 309kg/m ² s.....	43
35. The fractional uncertainty on vapor quality at different locations and for different operating conditions, for flow boiling of R-134a in the 510 μ m channel: white markers – variable mass velocity, black markers – variable heat flux.....	45
36. Relative error on the heat transfer coefficient for flow boiling experiments on R-134a and R-236fa in the 510 μ m channel at a nominal mass velocity of 400kg/m ² s..	45
37. Schematic comparison of the physical properties of the three refrigerants tested at 31°C.....	47
38. Flow boiling curves and flow patterns for (a) R-134a and (b) R-245fa, in the 510 μ m channel, relative to the last temperature acquisition location.....	48
39. Heat transfer coefficients versus vapor quality for saturated flow boiling of R-134a in the 510 μ m micro-channel for (a) 309, (b) 386, (c) 964, and (d) 1435kg/m ² s. The flow enters the channel as a sub-cooled liquid at 29°C, and exits as a saturated two-phase fluid at 31°C.....	49
40. Experimental heat transfer coefficients for R-134a in the 510 μ m channel, over a range of mass velocities at two heat fluxes. The flow enters the channel as a sub-cooled liquid at 29°C, and exits as a saturated two-phase fluid at 31°C.....	50
41. (a) Experimental heat transfer coefficients for R-134a at 31°C and different inlet temperatures, and (b) average heat transfer coefficients versus heat flux for three different outlet fluid temperatures. The results refer to the 510 μ m channel at a nominal mass velocity of 400kg/m ² s.....	50
42. (a) Heat transfer coefficients versus vapor quality in the 790 μ m channel, and (b) average heat transfer coefficients versus heat flux for the two tube sizes. The data refer to flow boiling of R-134a with T _{out} = 31°C and a nominal mass velocity of 1000kg/m ² s.....	51
43. Comparison with present data to those of Shiferaw <i>et al.</i> [45] for R-134a. Black markers refer to the data from [45] (G = 300kg/m ² s and 8bar), while white markers refer to the current database (G = 309kg/m ² s and p _{out} = 7.92bar).....	51
44. Heat transfer coefficients versus vapor quality for flow boiling of R-236fa in the 510 μ m tube for (a) 386 and (b) 957kg/m ² s. The flow enters the channel as a sub-cooled liquid at 29°C, and exits as a saturated two-phase fluid at 31°C.....	52

45. Experimental heat transfer coefficients for flow boiling of R-236fa in the 510 μ m channel for (a) different mass velocities with $T_{in} = 29^{\circ}\text{C}$ and $T_{out} = 31^{\circ}\text{C}$, and (b) different saturation conditions and a nominal mass velocity of 700kg/m ² s.....	52
46. (a) Heat transfer coefficients of R-236fa versus vapor quality in the 790 μ m channel, and (b) average heat transfer coefficients versus heat flux for the two tube sizes. The data refer to flow boiling with $T_{out} = 31^{\circ}\text{C}$ and a nominal mass velocity of 400kg/m ² s.....	53
47. Figure comparing the heat transfer results for (a) R-236fa and (b) R-134a in the 510 μ m channel with $T_{in} = 29^{\circ}\text{C}$ and $T_{out} = 31^{\circ}\text{C}$	53
48. Experimental heat transfer coefficients for R-245fa and local flow patterns, plotted versus vapor quality for flow boiling (510 μ m channel) at a mass velocity of 400kg/m ² s, with an inlet temperature of 30 $^{\circ}\text{C}$ and exiting at 32 $^{\circ}\text{C}$	54
49. Heat transfer coefficients versus vapor quality for flow boiling of R-245fa in the 510 μ m tube for (a) 305 and (b) 812kg/m ² s. The flow enters the channel as a sub-cooled liquid at 30 $^{\circ}\text{C}$, and exits as a saturated two-phase fluid at 32 $^{\circ}\text{C}$	54
50. Heat transfer coefficients versus vapor quality for flow boiling of R-245fa in the 790 μ m tube for (a) 300 and (b) 500kg/m ² s. The flow enters the channel as a sub-cooled liquid at 27 $^{\circ}\text{C}$, and exits as a saturated two-phase fluid at 31 $^{\circ}\text{C}$	55
51. Predicted versus experimental heat transfer coefficients. The predicted values refer to the methods by Lazarek and Black [5], Tran <i>et al.</i> [25], Kandlikar and Balasubramanian [41], and Zhang <i>et al.</i> [42]. O - R-134a, \square - R-236fa, Δ - R-245fa	55
52. Three-zone model [12] predictions versus the experimental heat transfer coefficients for (a) the entire database, and (b) only data for isolated bubble and coalescing bubble flows. O - R-134a, \square - R-236fa, Δ - R-245fa.....	56
53. Comparison of individual data sets with the predictions of the methods described in Chapter 2. The plots illustrate the local flow patterns, as classified in [19] (ib – isolated bubble, cb – coalescing bubble, a – annular).....	57
54. (a) Steady outer wall temperature during flow boiling, and (b) wall temperature during flow instability (black curve) as compared to the steady profile (shown in gray). Values refer to R-245fa in the 510 μ m tube, a heat flux of 50kW/m ² , and mass velocities of 500kg/m ² s (steady case) and 400kg/m ² s (unstable case). The signal sampling rate is of 1000S/s over 3s.....	61
55. Schematic showing the test-section, the valve, and the upstream compressible volume, as would occur in the present test facility.....	62
56. Wall temperature fluctuations taken 65mm downstream of the entrance to the evaporator, for an R-236fa flowing with a mass velocity of 700kg/m ² s.....	62
57. Wall temperature fluctuations and corresponding power spectrums for unstable flow boiling of R-245fa at different heat fluxes (510 μ m tube). The temperatures refer to the last thermocouple on the heated length.....	63

58. Fluctuations in the fluid temperature at the exit of the evaporator and corresponding power spectrums for flow boiling of R-245fa at different heat fluxes (510 μ m tube).....	64
59. Wall temperature fluctuations from the first and last thermocouples (19 and 65mm from the inlet respectively) on the heated length, for unstable flow boiling of R-236fa at a heat flux of 87kW/m ² and an average mass velocity of 400kg/m ² s.....	65
60. (a) Liquid compressibility of the three fluids tested from 25 to 35°C, and (b) the change in the internal characteristic for different fluids.....	66
61. (a) Stable and unstable heat transfer coefficients for R-245fa with D = 510 μ m, T _{in} = 30°C and T _{out} = 32°C, and (b) fluctuations in the pressure at the exit to the evaporator for the fully unstable flows.....	67
62. Heat transfer coefficients computed from stable and unstable flow data for (a) R-236fa at 30°C, and (b) R-134a at 31°C. D = 510 μ m in both cases.....	67
63. Heat transfer coefficients computed from unstable flow data for (a) R-245fa at 32°C, and (b) R-236fa at 31°C. The coefficients are shown for two levels of heat flux and a range of mass velocities and D = 510 μ m.....	68
64. Heat transfer coefficients computed from unstable flow data for fixed mass velocities and different heat fluxes, D = 510 μ m, and (a) R-245fa at 33°C with G = 400kg/m ² s, (b) R-245fa at 33°C with G = 600kg/m ² s, (c) R-236fa at 31°C with G = 700kg/m ² s, and (d) R-236fa at 31°C with G = 900kg/m ² s.....	68
65. Schematic representation of an elongated bubble, and the control volume for the analysis of the liquid film.....	70
66. Temporal evolution of the liquid film and the bubble nose before bubble-slug departure (the bubble tail is not shown). The film thickness, the axial coordinate, and time are reduced respectively by the initial film thickness, the bubble-slug departure length, and the passage period.....	72
67. The control volume for the determination of the liquid slug velocity.....	73
68. Control volume and mass flows for the evaluation of the bubble nose velocity.....	75
69. Nose film thickness versus time, as predicted by Eqs. (6.33) and (6.36) for a slug flow of R-134a at different levels of heat flux. Time is normalized by the bubble-slug passage period, Δt (Eq. (6.42)).....	76
70. Bubble-slug nose and rear positions in time for R-134a in a 500 μ m channel, flowing with a mass velocity of 400kg/m ² s and exposed to a wall heat flux of 25kW/m ²	78
71. Predicted heat transfer coefficients for R-134a at 7bar, flowing with a mass velocity of 400kg/m ² s in a 500 μ m channel.....	80
72. (a) Liquid, vapor and total heat transfer coefficient predictions for a slug flow of R-134a, and (b) the relative residence times of the two phases.....	80

73. Heat transfer coefficients versus vapor quality over a range of heat fluxes for (a) R-236fa and (b) R-245fa at 31°C, flowing with a mass velocity of 400kg/m ² s, in a 500µm channel.....	81
74. (a) Average heat transfer coefficients for R-134a at different saturation temperatures, and (b) average heat transfer coefficients for R-245fa in different diameter channels.....	81
75. R-236fa heat transfer coefficients versus vapor quality, for different mass velocities	82
76. Heat transfer predictions compared to the experimental data for the 510µm channel (ib – isolated bubble, cb – coalescing bubble, a – annular).....	83
77. Heat transfer predictions compared to the experimental data for the 790µm channel (ib – isolated bubble, cb – coalescing bubble, a – annular).....	84
78. Comparison with of heat transfer predictions with the experimental data for isolated bubble and coalescing bubble flows.....	85
A-1 Schematic of the model for the analysis of oscillatory instabilities, where subscript 1 refers to the flow through the heated length, while subscript 2 refers to the flow into the compressible volume.....	89
A-2 Control volume for the definition of inertia.....	90

List of Tables

1. Size and material characteristics of the evaporator and pre-heater tubes.....	28
2. Measurement instrumentation description and specifications.....	28
3. Specifications for the power supply and data acquisition units.....	28
4. The uncertainties for the set of thermocouples used during heat transfer data acquisitions.....	39
5. Uncertainties on mass velocity, heat flux, and heat transfer coefficients for the three fluids.....	46

Nomenclature

Latin

Symbol	Description	Units
A	cross-sectional area	m^2
Bi	Biot number	-
Bo	Boiling number	-
C	Chisholm parameter	-
Co	Confinement number	-
Cv	Convection number	-
c	specific heat	J/(kgK)
D	diameter	m
E	internal energy	J
F	two-phase factor	-
f	bubble passage frequency	Hz
Fr	Froude number	-
f	friction factor	-
G	mass velocity	$kg/(m^2s)$
g	gravitational acceleration	$9.81m/s^2$
h	specific enthalpy	J/kg
I	current	A
	inertia	kg/m^4
i	unit imaginary number	-
k	thermal conductivity	W/(mK)
j	superficial velocity	m/s
L	channel length	m
	Laplace operator	-
Nu	Nusselt number	-
Pr	Prandtl number	-
p	pressure	Pa
Q	heat	J
	volumetric flow rate	m^3/s
q	heat flux	W/m^2
R	radius	m
Ra	Rayleigh number	-
Re	Reynolds number	-
r	radial coordinate	m
S	boiling suppression factor	-
s	Laplace variable	-
T	temperature	$^{\circ}C$
t	time	s
u	specific internal energy	J/kg
V	volume	m^3
	Voltage	
v	specific volume	m^3/kg
W	mean velocity component in the z direction	m/s
We	Weber number	-

w	local velocity in the z direction	m/s
X	Martinelli parameter	-
x	vapor quality	-
z	axial coordinate	m

Greek

Symbol	Description	Units
α	heat transfer coefficient	W/m ² K
	thermal diffusivity	m ² /s
β	volumetric expansion coefficient	1/°C
δ	liquid film thickness	m
ε	relative heat loss	
η	heating efficiency	-
Φ	frictional multiplier	
μ	dynamic viscosity	Pa s
ν	kinematic viscosity	m ² /s
ω	frequency	Hz
ρ	density	kg/m ³
σ	surface tension	N/m
	standard deviation	°C
θ	uncalibrated temperature	°C
τ	shear stress	Pa

Subscripts

Symbol	Description
b	bubble
CV	control volume
cb	coalescing bubble
cond	conductive
conv	convective
cv	convective vaporization
d	dry-zone
do	dry-out
evp	evaporative
ex	exit
f	fluid
G	Gnielinski
g	internal generation
h	hydraulic
i	interfacial
ib	isolated bubble
in	inlet
l	liquid
lam	laminar
lo	liquid-only
lv	liquid-vapor

min	minimum
N	normal projection
	bubble nose
nb	nucleate boiling
out	exit
r	reference
S	side surface
SL	Shah and London
sat	saturation
sf	surface-fluid
T	bubble tail
turb	turbulent
th	threshold
tt	turbulent-turbulent
v	vapor
w	wall
l	outer wall
∞	ambient

Chapter 1

Introduction

Since the early 1980s the growing need of industry for compact, high heat flux cooling devices has elevated the interest in understanding the mechanisms and potential of convective boiling in small-size channels to a “global” level. From the experience developed on conventional heat sinks, a two-phase flow in a micro-channel is expected to present several important benefits compared to other competing methods for thermal control. Convective boiling often combines (1) high heat transfer at low mass flow rates, as well as (2) a nearly constant flow temperature due to the thermally saturated nature of a liquid-vapor mixture. Although boiling flows generally exhibit higher pressure drops than their single-phase counterparts, the substantial gain in heat transfer and the reduction in mass flow rate yield lower wall temperatures and potentially reduced pumping power consumption, while limiting system size and fluid charge. In addition, a more uniform flow temperature will dampen the axial temperature excursion in the channel wall, with beneficial effects on the degree of thermal stress and on the behavior of any temperature-sensitive component in contact with the cooling element.

Whereas for conventional systems the practicing engineer may rely on an extensive knowledge base concerning two-phase flow heat transfer and pressure drop, the design of a “micro” evaporator utilizing “macro” methods would result in extremely poor optimization, underperformance, or even material failure. The extent to which the system size will affect the flow morphology and the bubble nucleation process will depend on the fluid properties. Surface tension, for example, is expected to play an important role, since smaller channels present higher liquid-vapor interfacial curvatures. Identifying the threshold, or the transition band, beyond which a two-phase flow may be considered “micro” is an open issue. Several authors have proposed the Confinement number (Co),

$$Co = \frac{1}{D} \sqrt{\frac{\sigma}{(\rho_l - \rho_v)g}} \quad (1.1)$$

as the distinguishing parameter. The Confinement number represents the ratio between the capillary length scale (the square-root term) and the characteristic size of the channel (the channel diameter, D , for circular geometries), and is a measure of the relative importance of surface tension, σ , to the forces induced by gravity (buoyancy and liquid weight). Among the different threshold values proposed for Co , the most stringent is that of Suo and Griffith [1] who set $Co_{th} = 3.3$. Kew and Cornwell [2] suggest the flow assumes confined characteristics for values of Co above 0.5, while Brauner and Moalem-Maron [3] set the limit to 0.16.

As will be illustrated in the literature survey in Chapter 2, the current understanding of two-phase heat transfer in micro-channels is still far from being well-established. The large variety of trends in the experimental heat transfer coefficients lacks a solid theoretical basis and physical explanation. Crucial issues, such as the importance of nucleate boiling relative to convective vaporization, are still unclear. Micro-channel evaporators have been shown to be extremely sensitive to two-phase instabilities, thus posing an added difficulty to the already cumbersome experimental effort due to the minute sizes involved. At times, results for similar flow conditions from different research groups differ substantially in both trend and order of magnitude (see, for example, the recent review by Ribatski *et al.* [4]).

The present investigation aims at studying the effect of fluid properties, flow parameters and tube size on confined convective boiling heat transfer, in a single channel. The objective is to provide further insight into the heat transfer performance of these systems, analyzing the outcomes of stable and unstable flows, and suggesting possible explanations to the complex experimental trends.

A brief description of the contents of the chapters that follow is given below:

- Chapter 2. A literature review of the main topics of micro-channel flow boiling heat transfer, covering both theoretical and experimental work from the earliest studies to the latest results.
- Chapter 3. Description of the test facility, the test-sections and instrumentation, and the experimental procedures adopted during this research campaign, illustrating the data processing scheme, and the procedure for test validation.
- Chapter 4. The presentation and discussion of the experimental heat transfer results for stable two-phase flows.
- Chapter 5. Compressible volume instabilities and their effect on wall temperature and on the assessment of two-phase heat transfer coefficients.
- Chapter 6. A one-dimensional analysis of confined slug flow.
- Chapter 7. Concluding remarks and recommendations.

Chapter 2

Overview of Two-Phase Heat Transfer in Micro-Channels

The initial purpose of the studies on two-phase heat transfer in micro-channels was (and still is, to a certain extent) aimed at understanding the mechanisms controlling the convective vaporization process. The earliest results of Lazarek and Black [5] showed values for the heat transfer coefficient that were unaffected by vapor quality, but a function of heat flux, leading them to conclude that nucleate boiling was the dominant heat transfer mechanism as in macro-scale flow boiling. While others followed confirming this behavior, other new trends arose as the amount of experimentation in the sector grew. A significant number of studies found decreasing curves in the α -x plane rather than flat ones (with α the heat transfer coefficient and x the thermodynamic vapor quality), and even some increasing trends in α versus x, giving rise to a rather puzzling scenario with respect to the macro-scale knowledge base (these were documented, for instance, in Agostini and Thome [6]).

The relative importance of nucleate boiling and convection in the individual flow patterns that are characteristic to a micro-channel flow is thus still unclear. The studies directed specifically to flow patterns (see, for example, [7] and [8]), many of which were for air-water flows, found general agreement as to the four main modes: (i) bubbly flow, at very low mass fractions of air, (ii) slug flow, i.e. the passage of long bubbles separated by liquid slugs, (iii) churn flow, a transition mode between slug flow and fully annular flow, and (iv) annular flow, occurring at the highest gas superficial velocities. Recently, similar flow patterns have also been reported for the flow of refrigerants (cfr. [9]), confirming the absence of any stratified regime in the micro-scale. Cornwell and Kew [10] coupled flow patterns and heat transfer, by arguing that different flow modes presented different heat transfer mechanisms, varying from essentially nucleate boiling, to confined bubble boiling, and finally to purely convective evaporation for annular flows. Jacobi and Thome [11] and Thome *et al.* [12] postulated that during slug flow, nucleate boiling is completely suppressed and heat is transferred primarily by conduction through the thin evaporating film surrounding the elongated bubbles.

An added element to the discussion concerned the possible presence of periodic dry-out of the channel wall (see [2, 12, 13]). This mechanism however was not entirely understood, and very few gave a clear opinion as to how and when it occurred. The work presented in [12] was among the few that attempted to address this issue, suggesting the development of a dry-zone at the tail of an evaporating bubble.

In recent years, a number of studies provided evidence to the sensitivity of two-phase micro-channel systems to flow instabilities. Oscillating pressure drops and wall temperatures, and visualizations showing cyclical backflow, were encountered in many experiments. Bergles and Kandlikar [14] classified these as compressible volume instabilities, relating them to the presence of compressibility prior to the heated channels. Relative to a stable mode, an unstable system presents entirely different flow features, and may bring about substantial differences in the heat transfer mechanisms.

In summary, convective boiling in micro-channels has revealed to be much more complex than originally thought. The roles played by nucleate boiling, thin film evaporation, convective vaporization, flow patterns, periodic dry-out, instabilities, etc. are still unclear. What follows is a literature survey that will cover with further detail some of these issues.

2.1 Vapor Formation and Flow Development

Although many of the principles concerning the bubble nucleation process in conventional size systems are assumed to maintain validity at the micro-scale (Liu *et al.* [15] and Kandlikar [16], for example, extended Hsu's analysis for heterogeneous bubble nucleation to micro-scale flow boiling), the confined nature of a micro-channel may induce some notable differences. In particular, the channel diameter acts as a limiting value to bubble size in the transverse direction, favoring longitudinal growth and increased drag due to blockage of the channel. Lee *et al.* [17] observed the nucleation process for a flow of water in a trapezoidal micro-channel with a hydraulic diameter of $41.3\mu\text{m}$. Their visualizations reported two bubble growth stages, i.e. (1) isotropic growth, in which the bubble maintained its spherical shape, and (2) anisotropic growth, in which the bubble appeared distorted, sliding along the wall in the flow direction before detachment. Figure 1 shows three images taken from [17] illustrating different moments of the bubble growth process. In the last image, which illustrates the moment of departure, the bubble is seen to be actually larger than the channel depth, i.e.

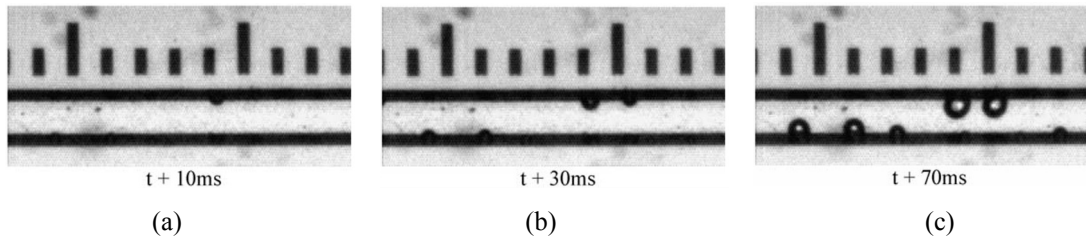


Figure 1. Bubble nucleation images (top view) from [17] at (a) 10, (b) 30, and (c) 70ms from the onset of boiling (flow is from right to left). Flow of water for a mass velocity of $341\text{kg/m}^2\text{s}$ and a heat flux of 189kW/m^2 .

the bubble is constrained by the top and bottom walls but not yet by the side-walls. Their measurements of bubble size, made by means of a ruler etched to the channel side (see Fig. 1; each minor division represents a $65\mu\text{m}$ interval), showed a linear variation of bubble radius with time during the isotropic growth stage, as to indicate an inertia controlled process. However, the estimated

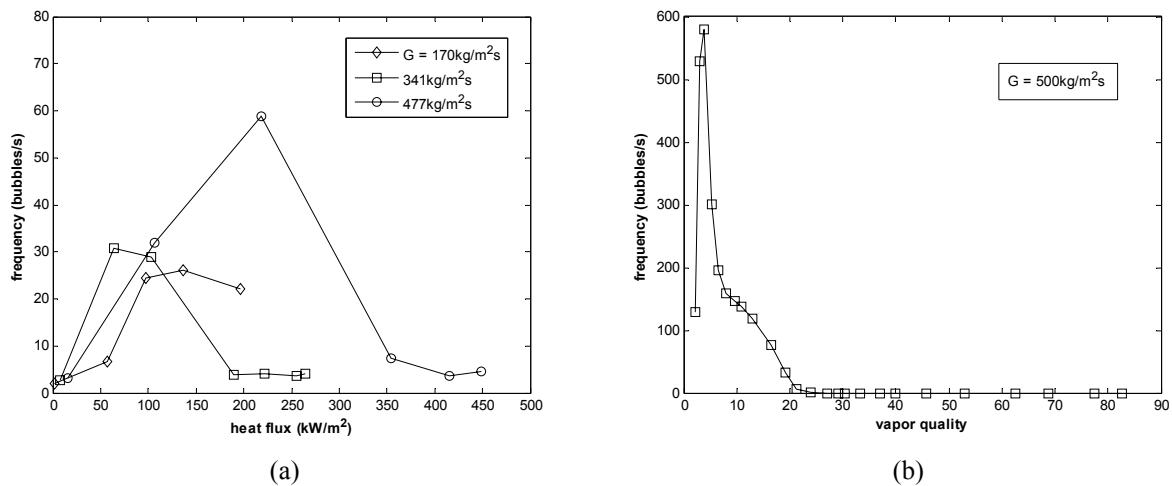


Figure 2. (a) Bubble departure frequency versus heat flux from [17] for de-ionized water in a trapezoidal channel with a $D_h = 41.3\mu\text{m}$, and (b) bubble passage frequency versus exit vapor quality for R-134a in a 0.5mm tube from [9].

growth rates were generally much lower than the values calculated by the Rayleigh equation. A constant bubble growth rate was also reported in [15]. Although the authors were unable to correlate the bubble departure frequency with the corresponding radius, their data showed frequencies that increased with heat flux reaching a peak value that then decreased with added power (as shown in Fig. 2).

Li and Peterson [18] performed experiments on the vapor formation process, testing subcooled water in a trapezoidal channel with a hydraulic diameter of $56\mu\text{m}$. Their system was comprised of two Pyrex wafers, bonded together by epoxy glue, with the channel fabricated in between. A square $100\mu\text{m}$ platinum heater (150nm thick) was positioned central to the axis of the channel, at a downstream location that guaranteed a fully developed laminar flow of liquid. The reported roughness of the platinum surface of 5nm , corresponding to the critical radius for homogenous nucleation, conveyed an ideally “smooth” heater, and lead to rather extreme heating requirements for boiling onset. Their tests for low, moderate, and high mass flow rates (583 , 1900 and $9000\text{kg/m}^2\text{s}$, respectively) provided evidence to three different modes for vapor formation: (1) a bubbly flow at the lowest flow rate, where a cyclical bubble growth and detachment process occurred, much like in the observations of [17]; (2) a wavy flow development at the intermediate flow rate, where a wavy vapor column positioned itself over the heater, extending in the flow direction, and releasing bubbles from its tip; (3) an annular flow at the highest mass velocity, similar to that observed for the moderate flow rate, but with a smoother liquid-vapor interface and an “open” ending due to the high bubble detachment speed. Figure 3 shows an extract of the images from [18].

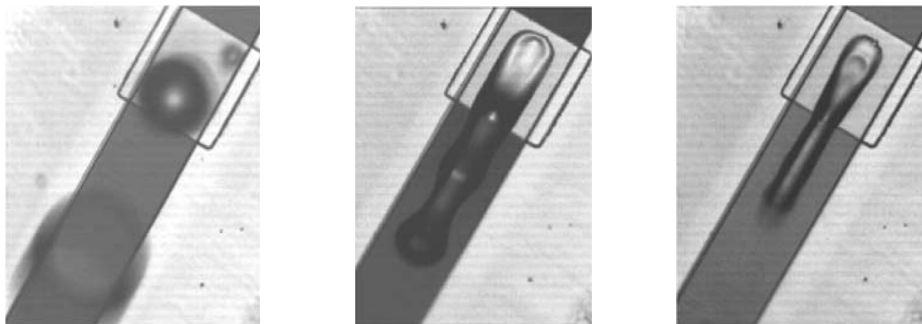


Figure 3. Bubbly, wavy, and annular vapor detachments from [18].

The flow patterns that develop downstream of the point of boiling onset may be classified into four main groups: bubbly flow, slug flow, churn flow, and annular flow (see Fig. 4 from the present study), with apparently no significant differences between the horizontal and vertical configurations since surface tension acts to reduce any effect of gravity. The bubbles leaving the heated wall form a bubbly flow, which is the flow of small bubbles with sizes less than the channel diameter. Among the numerous studies done on flow patterns in micro-channels (see [19] for a recent survey), bubbly flow has been reported to occur at high liquid superficial velocities and low vapor superficial velocities, and/or at low vapor qualities, as shown in Figs. 5 and 6. As evaporation progresses, the small bubbles grow axially and also coalesce, while being constrained by the channel wall in the radial direction. As the bubbles are no longer small with respect to the channel size, they define a new flow pattern, namely slug flow. With increasing void fraction, interfacial waves develop along the side of the elongated bubbles, with their wake inducing notable disturbances in the trailing liquid. These dynamic effects lead to the rupture of the interface at the bubble tail, creating smaller bubbles, and may also initiate coalescence, depending on the pressure field within the liquid bridges between individual bubbles. A churn flow occurs once the flow presents a substantial degree of mixing in the liquid, and the liquid-vapor interfaces are subjected to enhanced distortions. As the intermittent liquid regions

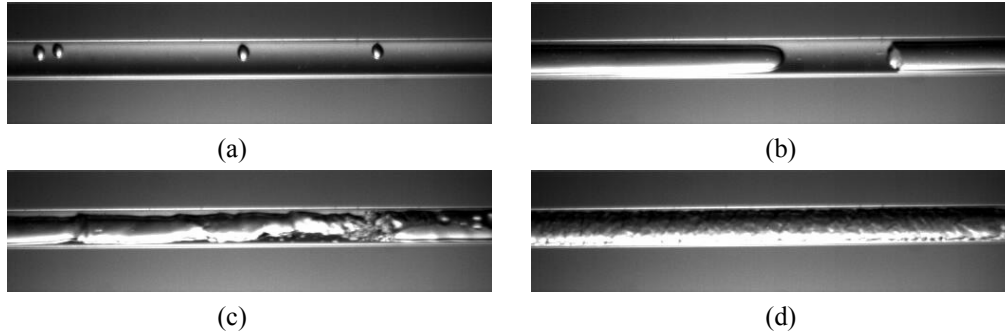


Figure 4. Micro-channel flow patterns: (a) bubbly, (b) slug, (c) churn, and (d) annular flows.

disappear, the flow assumes the characteristics of a common annular flow, where bubbles are no longer visible, and the remaining liquid forms a film in contact with the wall. In their investigation on flow patterns for refrigerants R-134a and R-245fa (two of the three refrigerants tested in the present work), Revellin and Thome [19] treated the importance of coalescence in the transition between flow patterns, introducing an intermediate flow mode, i.e. a “coalescing bubble” flow, that separates the bubbly region from the fully annular flow, and that is defined as the interval in vapor quality where the flow experiences a descent in bubble passage frequency due to coalescence (see Fig. 2b). Their flow pattern map is shown in Fig. 6. As mentioned earlier, Lee *et al.* [17] observed a similar behavior in the departure frequency of nucleating bubbles.

Different investigators have found particularities within the main flow patterns that relate to fluid properties and channel geometry. For example, in their steam-water and air-water experiments in very small channels down to 20 μm in diameter, Serizawa and coworkers [8] identified “liquid ring”

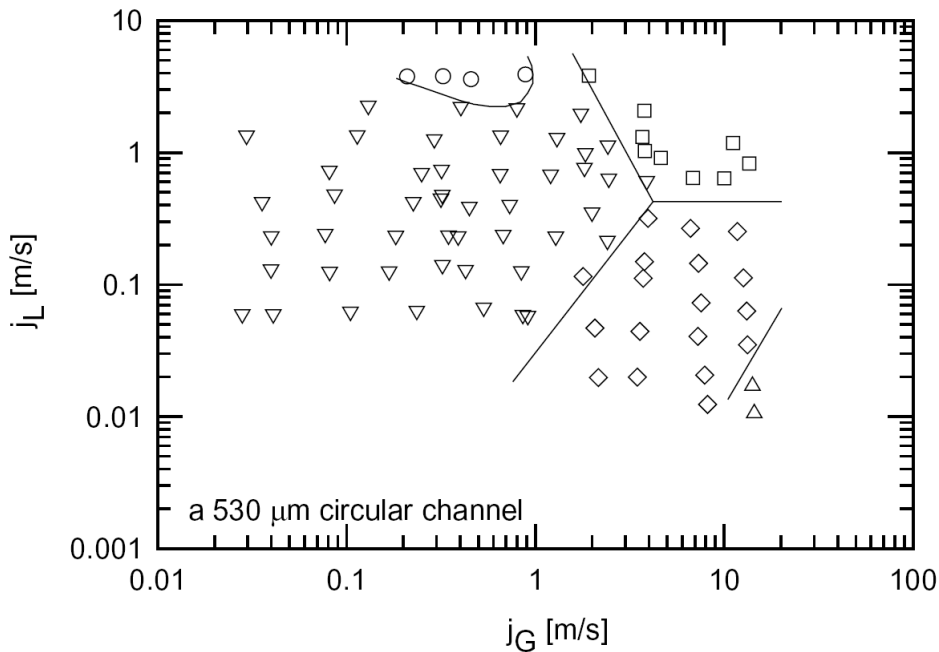


Figure 5. Flow pattern map by Chung and Kawaji [20] for a nitrogen-water flow in a 530 μm circular micro-channels. Symbols: \circ – bubbly flow; ∇ – slug flow; \square – churn flow; \diamond – slug-annular flow; \triangle – annular flow.

and “liquid lump” flows, which appeared to be crossing modes between slug and annular patterns. Dry-patches at the sides of bubbles were observed by Zhao and Bi [21], and more recently by Cubaud and Ho [22], in their visualizations for air-water in triangular and rectangular geometries, respectively. Both studies reported breakage of the liquid film due to liquid being drawn to the corners of their non-circular channels. Although it may be more likely to observe this behavior in air-water flows, due to the high surface tension of water, capillary-induced dry patches may play an important role in heated systems.

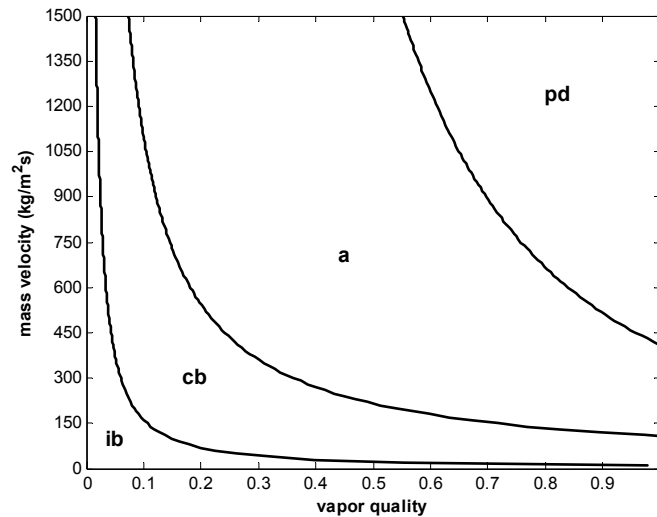


Figure 6. Flow pattern map by Revellin and Thome [19]: ib – isolated bubble flow, cb – coalescing bubble flow, a – annular flow, pd – post dry-out flow. Values for a flow of R-134a at 30°C in a 0.5mm channel, 70mm in length, and a uniform heat flux of 50kW/m².

2.2 Single-Channel Heat Transfer

Single micro-channel heat transfer experiments are often implemented using somewhat similar experimental and measurement techniques. Heat is usually provided to the flow by Joule effect, i.e. direct electrical heating of the tube wall, yielding a quasi-uniform wall heat flux boundary condition. The small system size usually prevents any direct measurements of either the fluid temperature or inner-wall temperature. In most studies the fluid temperature is estimated through the measured values at the channel inlet and outlet, while the inner-wall temperature is calculated from thermocouple measurements at the outer-wall. Recently, infrared thermography has also been used for this purpose. Heat losses from the test sections represent a common problem to any experimental work on micro-channels. To minimize losses by free convection, test set-ups have been placed at times in either temperature controlled environments [23], setting the ambient temperature as close to that of the tube wall as possible, or in vacuum chambers [24].

Among the first studies on flow boiling heat transfer in a single channel was the one by Lazarek and Black [5] who reported experimental heat transfer coefficients for flow boiling of R-113 in a vertical tube with an inner diameter of 3.1mm. Their heat transfer coefficients (see Fig. 7; negative vapor qualities refer to sub-cooled liquid flows, cfr. Eq. (3.10) in Section 3.3) had a strong dependency on the applied heat flux, but were essentially independent of vapor quality. Similar results were obtained by Tran *et al.* [25] and Bao *et al.* [26]. Tran and coworkers performed experiments on R-12 in circular and rectangular channels with sizes ranging from 2.40 to 2.92mm. Their data showed

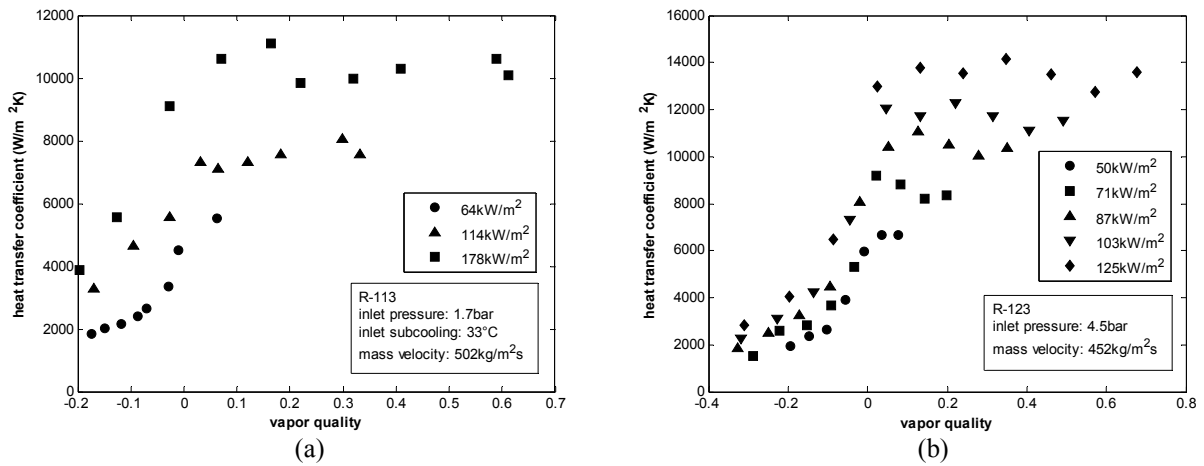


Figure 7. Heat transfer data from (a) Lazarek and Black [5] for R-113 in a 3.1mm tube and (b) Bao *et al.* [26] for R-123 in a 1.95mm tube.

that for a sufficiently high wall superheat (above 2.75°C) the values of the heat transfer coefficient were unaffected by vapor quality and mass velocity, but increased significantly with heat flux. The flow boiling experiments of Bao *et al.* again confirmed the heat transfer coefficient to be only a function of heat flux, and presented additional data showing the improvement in heat transfer with increasing saturation pressure. More recently, Lihong *et al.* [27] performed experiments on a 1.3mm circular channel for refrigerant R-134a, yielding similar results.

Added trends in heat transfer were reported in the work by Lin and coworkers [23] (Fig. 8a). In their study on R-141b (1.1mm tube), Lin *et al.* observed three distinct responses in the heat transfer coefficient to changes in heat flux and vapor quality: (1) at low heat fluxes, heat transfer improved with increasing vapor quality, (2) for intermediate values (from 30 to 53 kW/m^2 , for the case in Fig. 8) and vapor qualities within 0.40, the heat transfer coefficient increased with heat flux, much like what was observed in the investigations cited previously, and (3) at the highest heat fluxes, heat transfer was shown to gradually fall with x . While further heating increased the heat transfer coefficient for vapor fractions up to 0.40, the correspondence was much less clear beyond this threshold. Saitoh *et al.* [28]

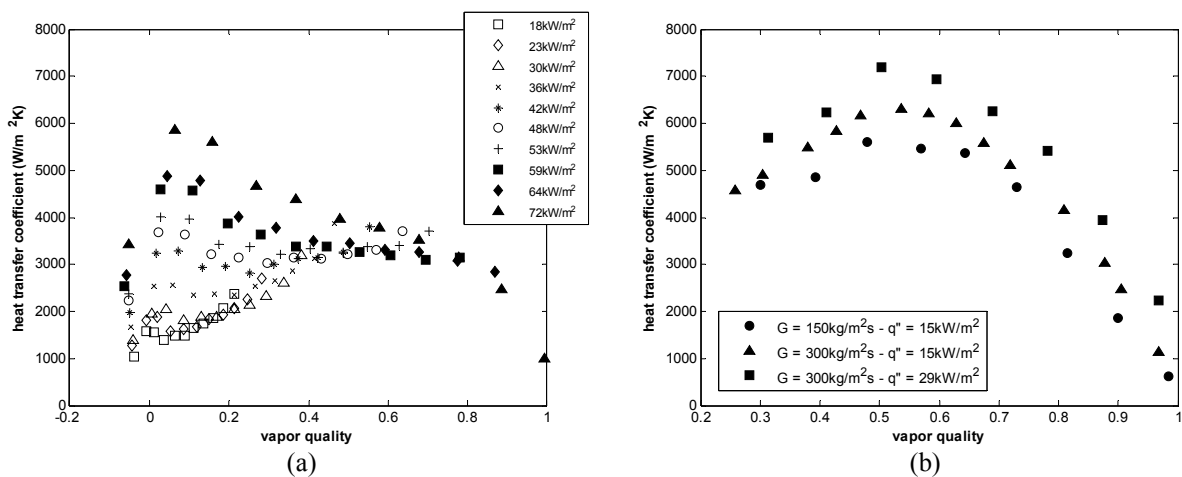


Figure 8. Heat transfer data from (a) Lin *et al.* [23] for R-141b in a 1.1mm channel and a mass velocity of 510 kg/m^2s , and (b) Saitoh *et al.* [28] for R-134a in a 0.51mm channel.

(see Fig. 8b) obtained heat transfer data for a boiling flow of R-134a in a 0.51mm tube (550mm long). Their experiments were performed at 15 and 29kW/m², for qualities extending to almost unity, and showed heat transfer coefficients with an inverted “U” shape in the α -x plane. The heat transfer data increased up to a quality of 0.60, beyond which the coefficients declined monotonically.

As for the effect of mass velocity, a number of investigations have shown heat transfer coefficients to remain unchanged when varying the fluid flow rate, as in the data from [25] (see Fig. 9a). Tran and coworkers [25] reported an improvement in heat transfer with mass velocity only for wall superheats lower than 2.75°C. The experiments from Bao *et al.* [26] on R-11 and R-123, and from Lihong *et al.* [27] on R-134a, also showed no change in heat transfer with flow rate, with the latter observing mild differences only at the lowest heat flux tested. One of the few studies on a single channel that presented a different outcome was that of Sumith *et al.* [29] (flow boiling of water in a 1.45mm vertical tube), reporting heat transfer coefficients that often decreased when increasing the flow, even at high heat fluxes.

At present, there is general agreement among the studies that addressed the effect of saturation conditions on heat transfer, that a higher saturation pressure/temperature yields higher heat transfer coefficients (see for example [26] and [27]). Figure 9b shows results from [26] for refrigerant R-11.

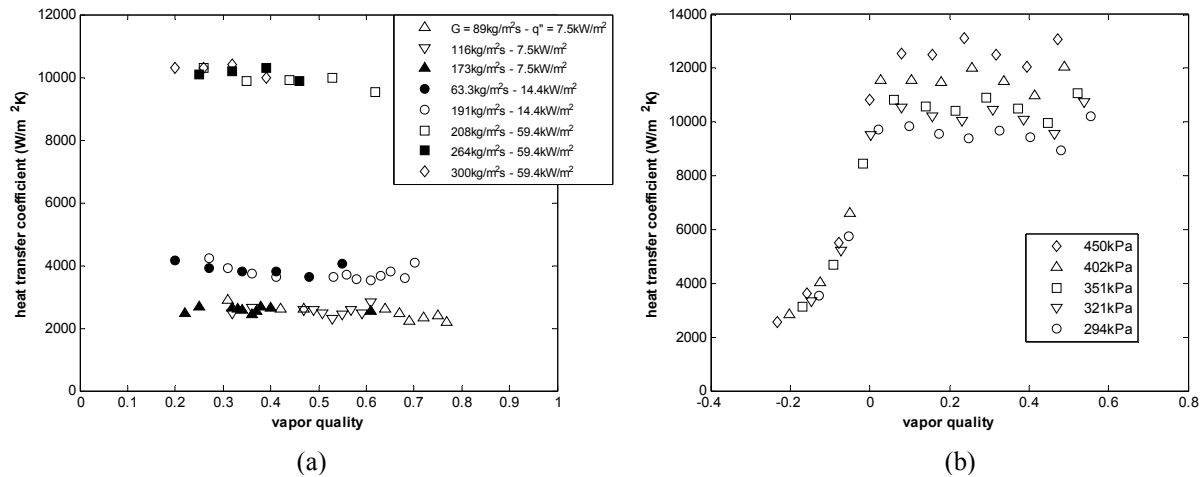


Figure 9. Heat transfer data for (a) R-12 in a 2.46mm channel from Tran *et al.* [25] for different heat fluxes and mass velocities, with a wall superheat above 2.75°C, and (b) R-11 in a 1.95mm channel from Bao *et al.* [26] at a heat flux of 125kW/m² and a mass velocity of 560kg/m²s.

2.3 Multi-Channel Heat Transfer

Multi-channel arrangements usually consist of a parallel sequence of channels in either a closed system configuration, or manufactured on the upper face of a copper or silicon block, with a transparent cover to allow for flow visualization (as in the case in Fig. 10, taken from [30]). Although some studies have utilized direct electrical heating, a number of experiments have relied on cartridge or film heating, exposing only one side of the system to the heat source (which is representative of what would occur in several applications, such as computer chip cooling). The shapes of the channel cross-sections have been many, including circular, rectangular, triangular and trapezoidal. As in the case for single channels, the wall temperatures are obtained through local measurements of the surface or by embedded thermocouples, or, when heating by a thin electrically conductive film, by infrared thermography. Multi-channel test-sections allow smaller channel sizes with respect to single channel

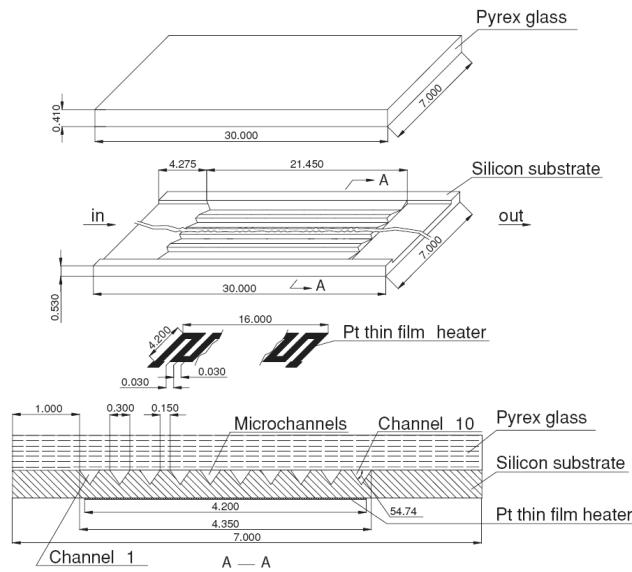


Figure 10. A schematic diagram of the multi-channel test-section used in [30].

set-ups, while permitting visualization of the flow during the vaporization process. However, the data analysis is generally more complex, since the boiling process is coupled to the quality of the flow distribution, as well as to conjugate heat transfer effects. In addition, multi-channel evaporators are also very sensitive to oscillatory instabilities.

Although most of the trends in heat transfer data reported for single channels appear also in multi-channel experiments, the latter add several elements of discussion and doubt to the overall picture. Increasing heat transfer coefficients with heat flux are observed in many investigations, and in some cases this is reportedly true only up to a limiting value of vapor quality, much like what was observed in [23] for single channels. For example, the data of Yan and Lin [31] (R-134a in 2mm circular channels) and Lee and Mudawar [32] (R-134a in rectangular channels, 231 μ m wide and 713 μ m deep) illustrated in Fig. 11, show a transition at approximately $x = 0.65$. Figure 11 also presents decreasing trends in the α - x plane that are commonly encountered in multi-channel experiments. Agostini and Bontemps [33] (R-134a in 11 parallel rectangular channels, 3.28mm wide and 1.47mm deep) and Xu *et al.* [30] (acetone in 10 triangular channels with a hydraulic diameter of 155 μ m) argued that this is related to the corresponding value of the Boiling number, $Bo (= q/Gh_{lv})$, with q the wall heat flux, G the mass velocity, and h_{lv} the latent heat of evaporation). Agostini and coworkers observed that for $Bo \times 10^3 < 0.43$ their heat transfer coefficients were weakly dependent on vapor quality and proportional to $q^{2/3}$, which is actually the same proportionality expressed by the Cooper correlation for nucleate pool boiling. This behavior was confirmed also for $Bo \times 10^3 > 0.43$, but only up to 40% in quality. For larger fractions of vapor, heat transfer was shown to decrease progressively, while maintaining the same relationship with the applied heat flux. Xu and coworkers found stationary and decreasing trends in the α - x plane for medium ($1.574 < Bo \times 10^3 < 3.219$) and high values ($3.562 < Bo \times 10^3 < 5.046$) of the Boiling number, although, as discussed in [30], these transitions were related to the extent of flow instabilities.

A change in heat transfer characteristics with Bo would imply an effect of mass velocity and of fluid properties (i.e. the latent heat). The studies on multi-channel systems that have investigated mass velocity and saturation conditions have produced contrasting results. The data from Pettersen [34] for flow boiling of CO_2 showed very little effect of mass velocity on heat transfer, particularly in the region where heat transfer was uncorrelated to vapor quality. On the other hand, the experimental work done by Qu and Mudawar [35] on water (same test section as in [32]) exhibited completely different results, showing heat transfer coefficients that increased with G . Similar conclusions were

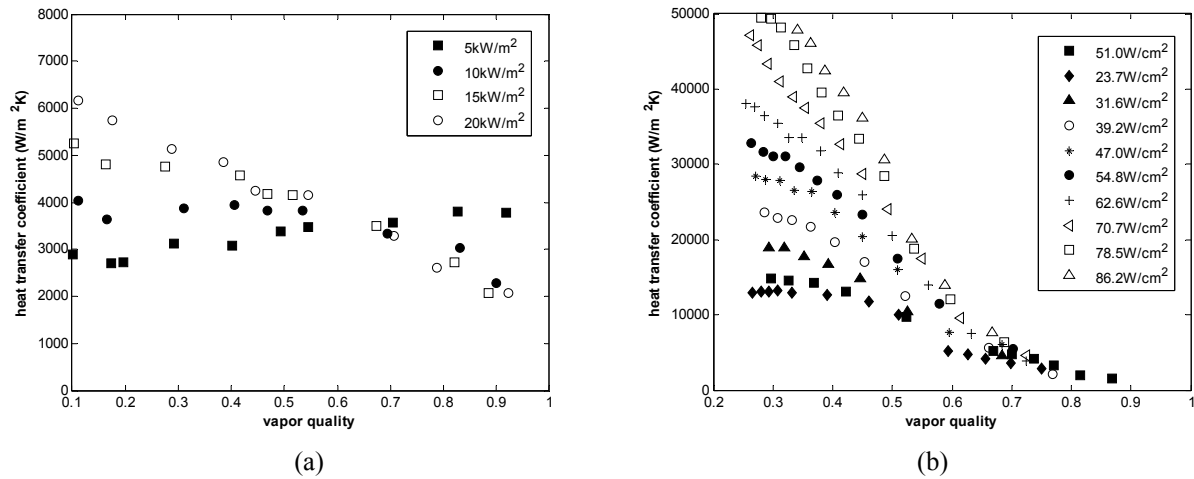


Figure 11. Heat transfer data from (a) Yan and Lin [31] for R-134a at 31°C in 28 2mm parallel circular channels, at a mass velocity of 200 kg/m²s, and (b) Lee and Mudawar [32] for R-134a in parallel rectangular micro-channels.

also reported by Yan and Lin [31]. Pettersen [34] and Agostini and Bontemps [33] also performed experiments at different saturation temperatures. While the data from [33] showed very little change in heat transfer, the measurements from [34] presented increasing heat transfer coefficients with saturation temperature, as well as a change in the overall trend with vapor quality.

Some of the studies cited above (see for example [30] and [33]) mentioned the occurrence of oscillatory phenomena during their tests. Agostini and Bontemps [33] observed that the oscillations in their wall temperature measurements increased dramatically at the high-end vapor qualities, reaching uncertainty values of above 3°C at the highest levels of heat flux. Xu and coworkers made flow visualizations through the top cover of their evaporator, and reported a cyclical boiling phenomenon, with contrasting characteristics with respect to those reported in many flow pattern studies.

2.4 Two-Phase Oscillatory Instabilities in Micro-Channel Evaporators

Among the different types of dynamic instabilities that are known to develop in two-phase systems, micro-channel flow boiling has been shown to be extremely sensitive to the “compressible volume” type (see [14]). Compressible volume instabilities may propagate in the presence of a certain degree of compressibility (a body of vapor, flexible hosing, etc.) upstream, or within, the heated length. The analysis of Maulbetsch and Griffith [36] gave very interesting insight into the phenomenon, the details of which are presented in the Appendix. To give a brief summary of their results, for the system in Fig. 12, comprised of a heated length, an upstream buffer tank, an inlet

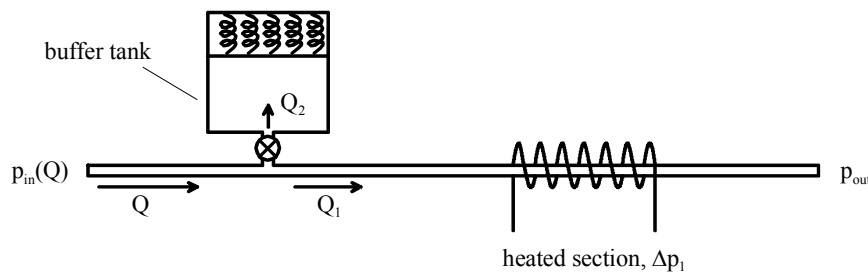


Figure 12. Schematic model for the analysis of oscillatory instabilities.

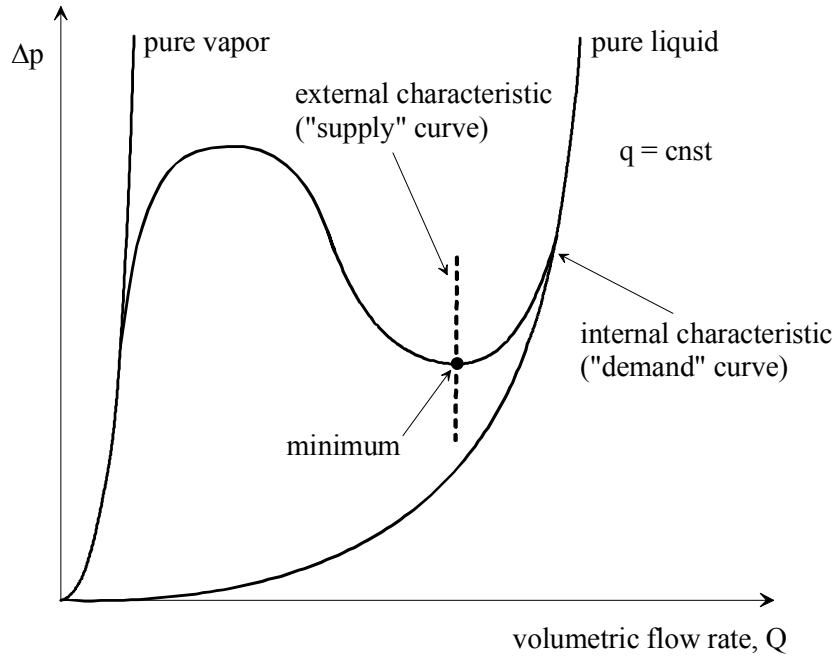


Figure 13. The internal and external characteristic curves for an evaporating flow at constant heat flux. The external characteristic is representative of a constant flow delivery system.

pressure that is function of the flow rate, and a constant exit pressure, oscillations in the mass flow and pressure drop will propagate when the gradient of the pressure drop versus flow curve (the internal characteristic, or “demand” curve, as shown in Fig. 13 for a two-phase flow) reaches a critical value,

$$\left. \frac{d(\Delta p_1)}{dQ} \right|_{\text{crit}} = \frac{\frac{dp_{\text{in}}}{dQ}(I_1 + I_2) + \sqrt{\left[\frac{dp_{\text{in}}}{dQ}(I_1 + I_2) \right]^2 + 4I_1^2 I_2 \left(\frac{dp}{dV} \right)_0}}{2I_2} \quad (2.1)$$

with Q the total volumetric flow rate, and I_1 and I_2 respectively the inertia of the flow in the heated section and of that into the buffer tank ($I = \rho L/A$, with ρ the density of the flow, L the length, and A the cross-sectional area of the corresponding sector; see Appendix). The term $(dp/dV)_0$ is a measure of the compressibility within the buffer tank, into which mass accumulates before being sent periodically back to the heated test-section. The oscillation frequency at the critical value given in Eq. (2.1), takes the form

$$\omega^2 = \frac{1}{2I_1 I_2^2} \left[- \left(\frac{dp_{\text{in}}}{dQ} \right)^2 (I_1 + I_2)^2 + \right. \\ \left. - \left(\frac{dp_{\text{in}}}{dQ} \right) \sqrt{\left(\frac{dp_{\text{in}}}{dQ} \right)^2 (I_1 + I_2)^2 + 4I_1^2 I_2 \left(\frac{dp}{dV} \right)_0} - 2I_1 I_2 \left(\frac{dp}{dV} \right)_0 \right] \quad (2.2)$$

In the two extreme cases of a constant flow delivery system and a constant pressure supply, the gradient to the external characteristic (the “supply” curve), dp_{in}/dQ , would yield: $dp_{\text{in}}/dQ \rightarrow -\infty$ and $dp_{\text{in}}/dQ = 0$ respectively. For the first case, a constant flow delivery system, a limit investigation gives:

$$\left. \frac{d(\Delta p_1)}{dQ} \right|_{\text{crit}} = 0 \quad \text{and} \quad \omega^2 = \frac{\left(\frac{dp}{dV} \right)_0}{I_1 + I_2} \quad (2.3)$$

This represents the least stable operating condition, since the oscillations would propagate as soon as the minimum is reached on the pressure drop-flow curve, as illustrated in Fig. 13. For the second case, the oscillatory instability would not occur, since only a rise in the inlet pressure could induce a flow into the compressible volume.

As the oscillations in the flow take place, the evaporator experiences a cyclical boiling phenomenon, which may be described as the periodic development of five distinct stages (see [30]): (1) single-phase liquid filling of the channel, (2) bubble nucleation over the channel length, (3) growth and coalescence of bubbles to form a vapor pouch over almost the entire cross-section, (4) a rapid expansion of the vapor that may involve the entire channel length, and (5) evaporation of the quasi-static liquid film left at the channel wall after the bubble expansion. The bubble in stage (4) may induce blockage of the flow in the heated section, or, if it grows towards the inlet, will provoke backflow of liquid into an upstream compressible volume or into adjacent channels. Figure 14 shows a schematic representation of the process. The morphology of an unstable flow is thus clearly different from what was described in the investigations in Section 2.1, where the micro-channel flow patterns were observed either in the absence of any boiling, i.e. for air-water flows, or under adiabatic conditions.

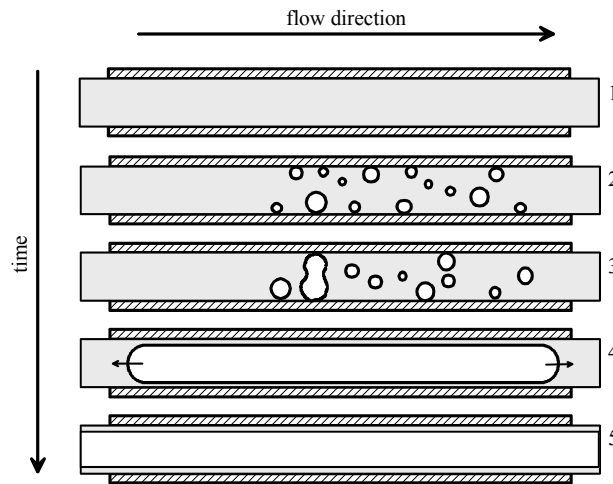


Figure 14. Schematic representation of the boiling features occurring during one cycle of an oscillatory instability.

Oscillations in pressure drop, flow, and wall temperatures are the typical symptoms of these instabilities, and are often found in the micro-channel literature. The periodic development of substantial dry-zones, along with possible fluctuations in the saturation temperature (coupled to the propagation of pressure pulses in the fluid), may explain the wall temperature oscillations. In [30] and [37] it was shown that for sufficiently high heat fluxes the liquid film left by the expanding bubble may dry-out, thus leaving the channel wall periodically in contact with only vapor. At the medium heat fluxes bubble nucleation has a stronger impact on heat transfer than the convective boiling process induced by the bubble expansion. The five-part sequence essentially reduces to the growth of the bubbles at the wall followed by liquid refilling of the channel, yielding heat transfer coefficients that are independent of vapor quality and that present the typical nucleate boiling characteristics. At

higher heat fluxes and lower mass velocities, the onset of nucleation shifts towards the channel inlet, and substantial convective vaporization results from the rapid bubble expansions. The probability of dry-out of the liquid film increases in the flow direction, thus explaining some of the reported decreasing heat transfer coefficients with increasing vapor quality. This was also suggested in the study of Agostini and Bontemps [33].

Kenning and Yan [38] reported oscillations in local pressure and wall temperature for experiments with different degrees of inlet compressibility. Their power spectrum analysis on both pressure and temperature signals gave peak values at frequencies around 6Hz. Brutin *et al.* [39] reported a stability diagram for their experiments on n-pentane flowing in a single rectangular channel with hydraulic diameter $D_h = 889\mu\text{m}$. Their experimental setup was similar to that in Fig. 12, but with a vertical heated section, and from their flow visualizations, they observed the instability and associated it with significant oscillations in pressure drop (with frequencies of about 4Hz). Using the onset of these fluctuations as a threshold between a stable and an unstable flow, Brutin and coworkers presented transition lines in terms of heat flux and mass flow rate.

Figure 15 shows the results of three studies that performed heat transfer measurements in the presence of oscillatory instabilities, or in the presence of regular oscillations in the wall temperature. The plots from [30] and [37] are for multi-channel systems, while the one from Cortina Díaz and Schmidt [40] is for a single rectangular micro-channel. As mentioned earlier, Xu *et al.* [30] argued that the extent of these flow oscillations determined different behaviors in the heat transfer coefficient (see

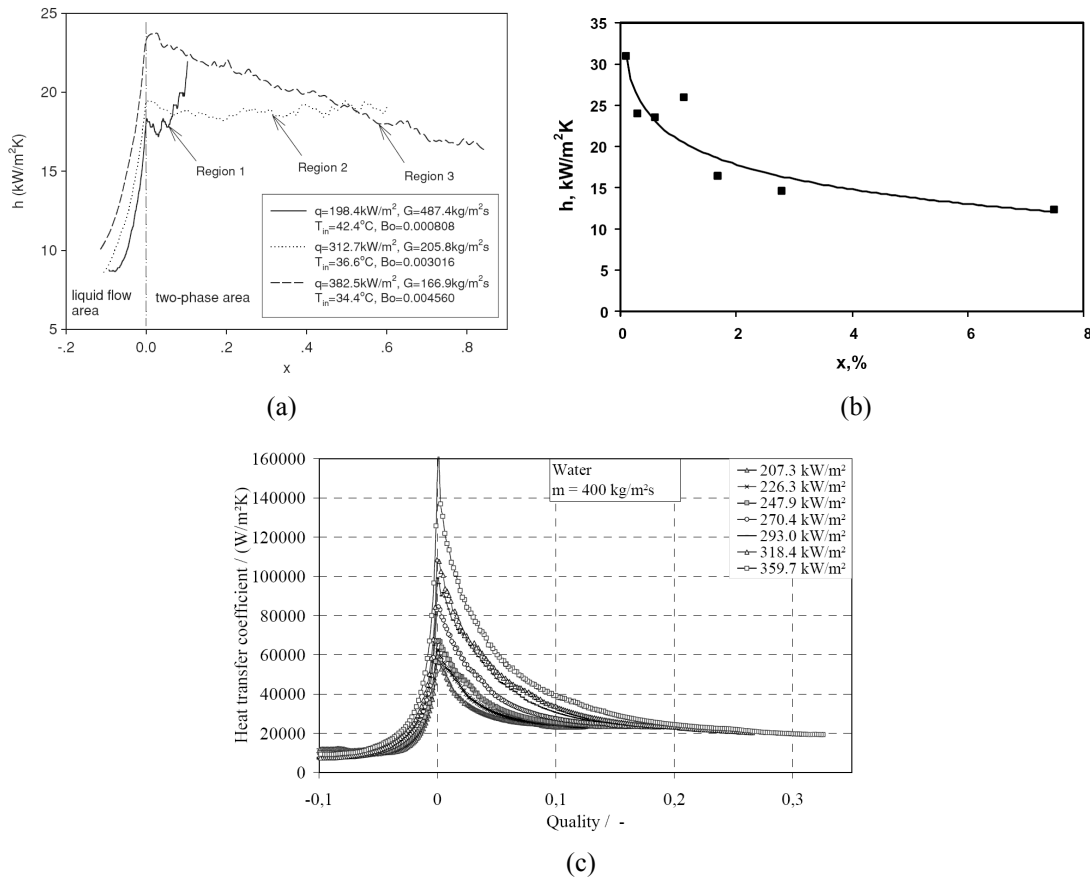


Figure 15. Heat transfer data from (a) Xu *et al.* [30] for acetone in 10 triangular channels with a hydraulic diameter of $155.4\mu\text{m}$, (b) Hetsroni *et al.* [37] for water in 21 parallel triangular micro-channels, and (c) Cortina Díaz and Schmidt [40] for water in a single rectangular channel with a hydraulic diameter of 0.59mm .

Fig. 15a), and associated each to an interval in the Boiling number (Bo). The data from [37] and [40]

were both taken for flow boiling of water, and show very high values for the heat transfer coefficient at low vapor qualities that decrease, at times dramatically, within a few units of x .

2.5 Heat Transfer Prediction Methods

The variety of trends in heat transfer data and the inherent difficulties in performing experimental work on these small systems have made it very challenging to develop a well-established understanding of convective boiling in micro-channels. Several authors have correlated their experimental results through different sets of generally non-dimensional groups. Others, on the other hand, have attempted to either extend methods previously developed for conventional macro-scale systems to the micro-scale, or define new approaches specifically for micro-channel two-phase flows. Nonetheless, the question concerning the controlling heat transfer mechanisms remains unanswered. What follows is a description of the different approaches to the prediction of two-phase heat transfer coefficients for flow boiling in micro-channels.

Lazarek and Black correlation

From their heat transfer experiments on R-113, Lazarek and Black [5] proposed the following non-dimensional correlation for the flow boiling Nusselt number ($Nu_l = \alpha D/k_l$),

$$Nu_l = 30 Re_{lo}^{0.857} Bo^{0.714} \quad (2.4)$$

with $Re_{lo} = GD/\mu_l$, the all-liquid Reynolds number, and $Bo = q/(Gh_{lv})$. Equation (2.4) expresses no dependence of the heat transfer process on the local vapor quality.

Tran *et al.* correlation

As mentioned earlier, in their experiments on R-12 and R-113 Tran and coworkers [25] observed that for wall superheats above 2.75°C their heat transfer data expressed a typical α versus q behavior, assigning this to the macro-scale mechanism of nucleate boiling. The authors therefore modified the correlation of Lazarek and Black, Eq. (2.4), by replacing the Reynolds number with the Weber number, $We_{lo} = G^2 D/(\rho_l \sigma)$, removing viscous effects in favor of surface tension. The liquid to vapor density ratio was also added to further account for variations in fluid properties, so that

$$\alpha = (8.4 \times 10^5) Bo^{0.6} We_{lo}^{0.3} \left(\frac{\rho_l}{\rho_v} \right)^{-0.4} \quad (2.5)$$

The 8.4×10^5 factor in Eq. (2.5) is dimensional, with units $W/(m^2 K)$. Equation (2.5) removes any dependence of the heat transfer coefficient on mass velocity. Furthermore, Eq. (2.5) also yields the following proportionality between the heat transfer coefficient and the channel diameter: $\alpha \propto D^{0.3}$, which is somewhat unexpected.

Kandlikar and Balasubramanian correlation

Kandlikar and Balasubramanian [41] extended the correlation proposed by Kandlikar for conventional tubes, where the local two-phase heat transfer coefficient was determined according to the value of the dominant mechanism between nucleate boiling (nb) and convective evaporation (cv):

$$\alpha = \text{larger of } \begin{cases} \alpha_{nb} \\ \alpha_{cv} \end{cases} \quad (2.6)$$

The original correlations for the two coefficients in Eq. (2.6) were developed for all-liquid Reynolds numbers, Re_{lo} , above 3000, and presented the following functional dependencies,

$$\frac{\alpha_{nb}}{\alpha_l} \quad \text{and} \quad \frac{\alpha_{cv}}{\alpha_l} = f \left[\left(\frac{\rho_v}{\rho_l} \right)^{0.5} \left(\frac{1-x}{x} \right)^{0.8}, \frac{q}{G h_{lv}}, \frac{G^2}{\rho_l^2 g D}, x \right] \quad (2.7)$$

The non-dimensional groups in Eq. (2.7) are respectively the Convection number, Cv , the Boiling number, Bo , the all-liquid Froude number, Fr_{lo} , and the vapor quality. For $Re_{lo} > 3000$, Kandlikar suggested using transition (Gnielinski) and fully turbulent (Petukhov and Popov) correlations for the single-phase liquid heat transfer coefficient, α_l , based on the all-liquid Reynolds number. However, for smaller channels the authors argued that the value of the Reynolds number was generally lower than 3000, making the above single-phase correlations inconsistent. Furthermore, the reduced effect of gravity in micro-channels justified the removal of the Froude number from Eq. (2.7). In view of both these considerations, Kandlikar and Balasubramanian proposed the following modified correlations for α_{nb} and α_{cv} :

$$\frac{\alpha_{nb}}{\alpha_l} = 0.6683 Cv^{-0.2} (1-x)^{0.8} + 1058.0 Bo^{0.7} (1-x)^{0.8} F_{sf} \quad (2.8)$$

$$\frac{\alpha_{cv}}{\alpha_l} = 1.136 Cv^{-0.9} (1-x)^{0.8} + 667.2 Bo^{0.7} (1-x)^{0.8} F_{sf}$$

with F_{sf} a constant that accounts for the surface material-fluid combination. For Reynolds numbers in the range $1600 \leq Re_{lo} < 3000$, the authors suggested interpolating between laminar and transition correlations for α_l . On the other hand, for $Re_{lo} < 1600$ the flow was considered laminar, and a laminar correlation of the form $Nu = \alpha_l D / k_l = \text{constant}$ was deemed applicable. Finally, for $Re_{lo} \leq 100$ Eq. (2.6) was modified to $\alpha = \alpha_{nb}$, with α_{nb} given by Eq. (2.8).

Zhang *et al.* extension of Chen's correlation

Zhang and coworkers [42] analyzed thirteen separate databases, confronting them with some of the most widely quoted correlations for two-phase heat transfer in conventional systems. Chen's superposition model gave the best outcome. However, the authors observed that for micro-channels, the values of the liquid Reynolds numbers, $Re_l = G(1-x)/\mu_l$, were mostly lower than 2000, i.e. lower than the laminar-transition threshold, and argued that this was inconsistent with the original form of Chen's model (a similar reasoning to that of Kandlikar and Balasubramanian). Chen's superposition model for convective boiling states that heat is transferred by two competing mechanisms, namely nucleate boiling and convective vaporization. The overall heat transfer coefficient is given by an additive law that combines these different contributions,

$$\alpha = \alpha_{nb} + \alpha_{cv} \quad (2.9)$$

The nucleate boiling term in Eq. (2.9) is expressed as the product of the nucleate pool boiling value computed at the corresponding wall superheat through the Forster-Zuber correlation, and a boiling

suppression factor, S , that accounts for the suppression of bubble nucleation due to the convective nature of the two-phase system,

$$\alpha_{nb} = S \left[0.00122 \left(\frac{k_l^{0.79} c_{p,l}^{0.45} \rho_l^{0.49}}{\sigma^{0.5} \mu_l^{0.29} h_{lv}^{0.24} \rho_v^{0.24}} \right) \Delta T_{sat}^{0.24} \Delta p_{sat}^{0.75} \right] \quad (2.10)$$

On the other hand, the convective contribution is given by the second term in Eq. (2.9), i.e. an all liquid heat transfer coefficient that multiplies a two-phase correction factor, F :

$$\alpha_{cv} = F \left[0.023 \text{Re}_l^{0.8} \text{Pr}_l^{0.4} \left(\frac{k_l}{D} \right) \right] \quad (2.11)$$

Equation (2.11) makes use of the Dittus-Boelter correlation for the single-phase heat transfer coefficient, which is generally assumed valid for fully turbulent flows (Reynolds numbers of above 10000), and the F factor was originally given as a function of the turbulent-turbulent Martinelli parameter, X_{tt} :

$$F = 2.35 \left(\frac{1}{X_{tt}} + 0.213 \right)^{0.736} \quad \text{for} \quad \frac{1}{X_{tt}} > 0.1 \quad (2.12)$$

$$F = 1 \quad \text{for} \quad \frac{1}{X_{tt}} \leq 0.1$$

Zhang and coworkers argued that Eq. (2.11) should thus be reexamined to account for the laminar nature of the liquid flowing in a micro-channel. To do so the authors observed that the top F factor in Eq. (2.12) may be expressed approximately as

$$F \cong 0.64 \left(1 + \frac{20}{X_{tt}} + \frac{1}{X_{tt}} \right)^{0.5} \quad \text{or} \quad F \cong F' = 0.64 \Phi_{l,tt} \quad (2.13)$$

with the term in parenthesis being the two-phase friction multiplier, $\Phi_{l,tt}^2$, and that the final form of the F factor was to be chosen from the largest between the value given by Eq. (2.13) and 1: $F = \max\{F', 1\}$. Equation (2.13) establishes a formal relationship between the pressure drop ratio, represented by the frictional multiplier, and the ratio in heat transfer coefficients (two-phase convective to single-phase liquid) given by the F factor. Although the expression was formulated for both phases in turbulent regimes, Eq. (2.13) was then extended to the general case as

$$F' = 0.64 \Phi_l \quad (2.14)$$

where

$$\Phi_l^2 = 1 + \frac{C}{X} + \frac{1}{X^2} \quad \text{and} \quad X^2 \equiv \left(\frac{dp}{dz} \right)_l / \left(\frac{dp}{dz} \right)_v \quad (2.15)$$

are respectively the general form of the two-phase multiplier¹ and the definition of the Martinelli parameter. From the expressions of the single-phase liquid and vapor pressure gradients, the Martinelli parameter assumes the form

$$X = \left(\frac{f_l}{f_v} \right)^{0.5} \left(\frac{1-x}{x} \right) \left(\frac{\rho_v}{\rho_l} \right)^{0.5} \quad (2.16)$$

with f_l and f_v the single-phase friction factors determined from the respective Reynolds numbers,

$$\text{Re}_l = \frac{G(1-x)D}{\mu_l} \quad \text{and} \quad \text{Re}_v = \frac{Gx D}{\mu_v} \quad (2.17)$$

Although Zhang *et al.* gave no direct proof of the existence of nucleate boiling in micro-channels (as was also not provided in [41]), the authors suggested that as in conventional flows, the bubble nucleation process should tend towards the pool boiling behavior for small values of the liquid Reynolds number. Therefore, they stated that the expression proposed by Chen for the suppression factor (S),

$$S = \frac{1}{1 + 2.53 \times 10^{-6} \text{Re}_l^{1.17}} \quad (2.18)$$

and Eq. (2.10) maintained their validity also for micro-channels.

Thome *et al.* three-zone evaporation model for slug flow

Thome and coworkers [12] developed a phenomenological method to describe heat transfer for a purely convective micro-channel slug flow (no nucleate boiling), based on the following set of assumptions:

1. The vapor and liquid travel at the same velocity (homogeneous flow).
2. The heat flux is uniform and constant with time along the inner wall of the micro-channel.
3. All energy entering the fluid is used to vaporize liquid. Thus, the temperatures of the liquid and vapor remain at the saturation value, i.e. neither the liquid nor the vapor is superheated.
4. The local saturation pressure is used for determining the local saturation temperature.
5. The liquid slug initially contains all liquid that flows past the nucleating bubble (at $x = 0$) until it grows to the channel diameter.
6. The liquid film remains attached to the wall. The influence of vapor shear stress on the liquid film is assumed negligible, so that it remains smooth without ripples.
7. The thickness of the film is very small with respect to the inner radius of the tube.
8. The thermal inertia of the channel wall can be neglected.

¹ The C parameter in Eq. (2.15), known also as Chisholm's parameter, assumes different values according to the flow modes of the liquid and vapor phases: (i) for Re_l and Re_v below 1000, $C = 5$, (ii) for $\text{Re}_l > 2000$ and $\text{Re}_v < 1000$, $C = 10$, (iii) for $\text{Re}_l < 1000$ and $\text{Re}_v > 2000$, $C = 12$, and (iv) for Re_l and Re_v above 2000, $C = 20$. For combinations of the two Reynolds numbers that are in between these four categories, Zhang *et al.* suggest using interpolated values.

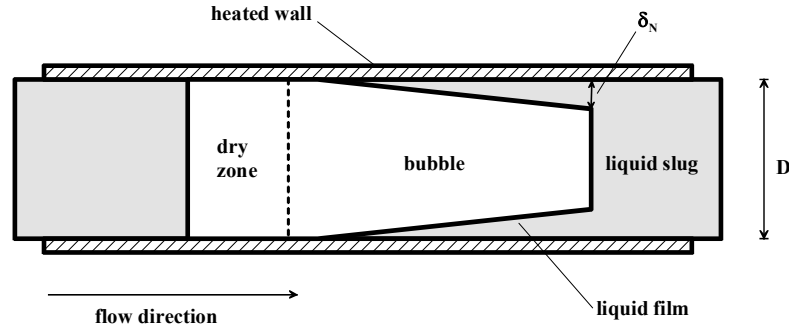


Figure 16. The three-zone evaporation model.

Slug flow was modeled as a cyclical passage of a “three zone” sequence, comprising a liquid slug, an elongated bubble surrounded by an evaporating liquid film, and an all-vapor dry-zone at the bubble tail (see Fig. 16). The first assumption yields an equal velocity, W , for the vapor and liquid, given by the homogeneous expression,

$$W = G \left(\frac{x}{\rho_v} + \frac{1-x}{\rho_l} \right) \quad (2.19)$$

with G the total mass velocity and x the thermodynamic vapor quality. The residence times of the vapor, intended as the elongated bubble plus the dry-zone, and the liquid slug, respectively Δt_v and Δt_l , were derived from the definition of vapor quality and through Eq. (2.19) as

$$\Delta t_v = \frac{G x}{\rho_v W} \Delta t = \frac{\Delta t}{1 + \frac{\rho_v}{\rho_l} \frac{1-x}{x}} \quad \text{and} \quad \Delta t_l = \frac{G(1-x)}{\rho_l W} \Delta t = \frac{\Delta t}{1 + \frac{\rho_l}{\rho_v} \frac{x}{1-x}} \quad (2.20)$$

with Δt the passage period of the three-zone structure, and having neglected the liquid mass within the film. The local film behavior was modeled as the evaporation of a stagnant liquid layer, i.e. from an energy balance at given axial position, z :

$$2\pi R q dz = -2\pi \rho_l (R - \delta) \frac{d\delta}{dt} h_{lv} dz \quad \text{therefore} \quad d\delta = -\frac{q}{\rho_l h_{lv}} \frac{R}{(R - \delta)} dt \quad (2.21)$$

with δ the thickness of the film, q the uniform wall heat flux and R the channel radius. In view of Eq. (2.21), the film thickness will vary from an initial value, corresponding to the liquid film thickness at the bubble nose, δ_N , to a value given by the bubble residence time. From assumption 7, and by integration of Eq. (2.21),

$$\delta(t, z) = \delta_N(z) - \frac{q}{\rho_l h_{lv}} t \quad (2.22)$$

Assuming the condition for dry-out of the liquid film to occur at a finite value of the film thickness, $\delta = \delta_{\min}$, equivalent to the surface roughness (a representative value of $0.3 \mu\text{m}$ was recommended for δ_{\min}), the dry-zone will be present when the time required for film dry-out,

$$\Delta t_{do} = \frac{\rho_l h_{lv}}{q} [\delta_N(z) - \delta_{min}] \quad \text{gives} \quad \Delta t_v > \Delta t_{do} \quad (2.23)$$

The expression for the bubble nose film thickness was derived from the correlations of Moriyama and Inoue as

$$\frac{\delta_N}{D} = 0.29 \left(3 \sqrt{\frac{\nu_l}{WD}} \right)^{0.84} \left[(0.07 We^{0.41})^{-8} + 0.1^{-8} \right]^{-1/8} \quad (2.24)$$

with ν_l the fluid's kinematic viscosity and We the Weber number ($= \rho_l DW^2/\sigma$).

In terms of heat transfer, the authors suggested a transient behavior of the heat transfer coefficient, determined by the local flow conditions: (1) single phase convection during the passage of a liquid slug or a dry-zone, and (2) conduction of heat through the liquid film during the passage of an elongated bubble. The local time-averaged heat transfer coefficient was thus given as

$$\alpha = \frac{\Delta t_l \alpha_l + \Delta t_b \alpha_b + \Delta t_d \alpha_d}{\Delta t}, \quad (2.25)$$

with Δt_l the residence time of the liquid slug given by Eq. (2.20), and Δt_b and Δt_d the residence times of the bubble and dry-zone respectively,

$$\begin{aligned} \Delta t_b &= \Delta t_v & \text{and} & & \Delta t_d &= 0 & \text{for} & & \Delta t_v \leq \Delta t_{do} \\ \Delta t_b &= \Delta t_{do} & \text{and} & & \Delta t_d &= \Delta t_v - \Delta t_{do} & \text{for} & & \Delta t_v > \Delta t_{do} \end{aligned} \quad (2.26)$$

The single-phase heat transfer coefficients in Eq. (2.25) were determined by asymptotic interpolation of standard correlations, i.e. Shah and London (SL) for $Re \leq 2300$ and Gnielinski (G) for $Re > 2300$:

$$Nu_{l,d} = (Nu_{SL}^4 + Nu_G^4)^{1/4} \quad (2.27)$$

with

$$Nu_{SL} = 0.91 \sqrt[3]{Pr} \sqrt{\frac{Re D}{L}} \quad \text{and} \quad Nu_G = \frac{\frac{f}{8} (Re - 1000) Pr}{1 + 12.7 \sqrt{\frac{f}{8}} (Pr^{2/3} - 1)} \left[1 + \left(\frac{D}{L} \right)^{2/3} \right] \quad (2.28)$$

the average laminar and transition to turbulent Nusselt numbers over the single-phase lengths. In Gnielinski's correlation the friction factor is taken as $f = (1.82 \log_{10} Re - 1.64)^{-2}$. The bubble heat transfer coefficient, α_b , was determined by applying simple conduction theory through the liquid film,

$$\alpha_b(z) = \frac{1}{\Delta t_b} \int_0^{\Delta t_b} \frac{k_l}{\delta(t, z)} dt \cong \frac{2 k_l}{\delta_N + \delta_T} \quad (2.29)$$

with δ_T the minimum local film thickness (the subscript 'T' stands for the bubble tail) given from Eq. (2.22) as

$$\delta_T(z) = \delta_N(z) - \frac{q}{\rho_l h_{lv}} \Delta t_v \quad \text{for} \quad \Delta t_v \leq \Delta t_{do}$$

$$\delta_T(z) = \delta_{\min} \quad \text{for} \quad \Delta t_v > \Delta t_{do}$$
(2.30)

The final equation that provided closure to the model was for the passage period, Δt , of the liquid-bubble-vapor dry-zone triplet. The authors suggested correlating Δt with the wall heat flux and fluid properties, proposing the following dimensional correlation (q in W/m^2 and Δt in s):

$$\Delta t = \left(\frac{1}{3328} p_r^{0.5} q \right)^{-1.74}$$
(2.31)

with p_r the reduced pressure (the ratio of the saturation pressure to the fluid's critical pressure; $p_r = p_{\text{sat}}/p_c$).

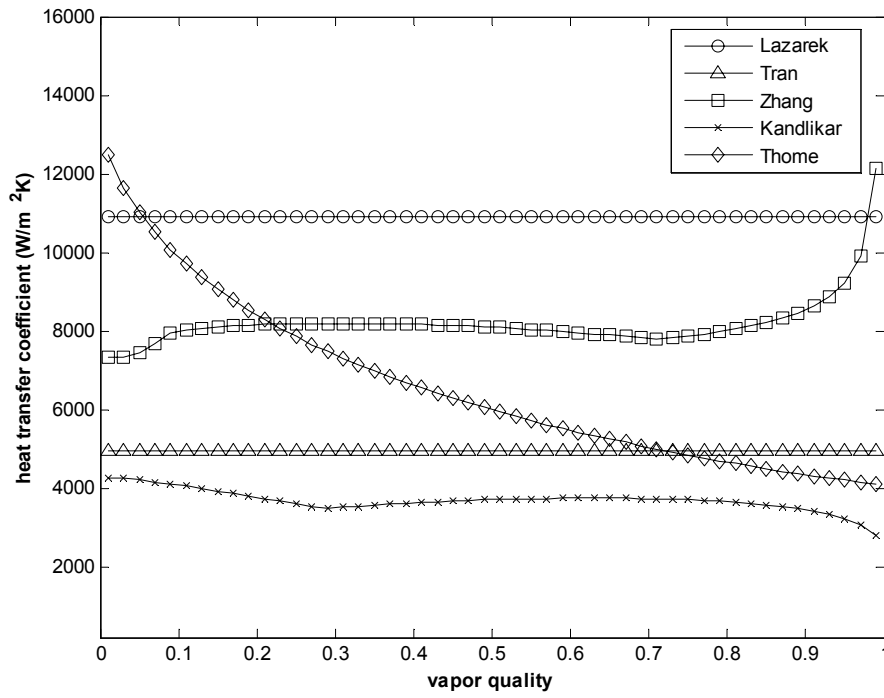


Figure 17. Predicted two-phase heat transfer coefficients. Values for R-134a at 7bar, with $q = 50\text{kW/m}^2$, $G = 500\text{kg/m}^2\text{s}$, in a $D = 0.5\text{mm}$ circular, stainless steel channel.

Figure 17 compares the predictions for flow boiling heat transfer coefficients at a given operating condition. As the figure shows, the predictions differ in trend and, at times, even in order of magnitude. The nucleate boiling and convective evaporation regions are clearly visible in the correlation by Zhang *et al.*, while the three-zone model gives decreasing coefficients with vapor

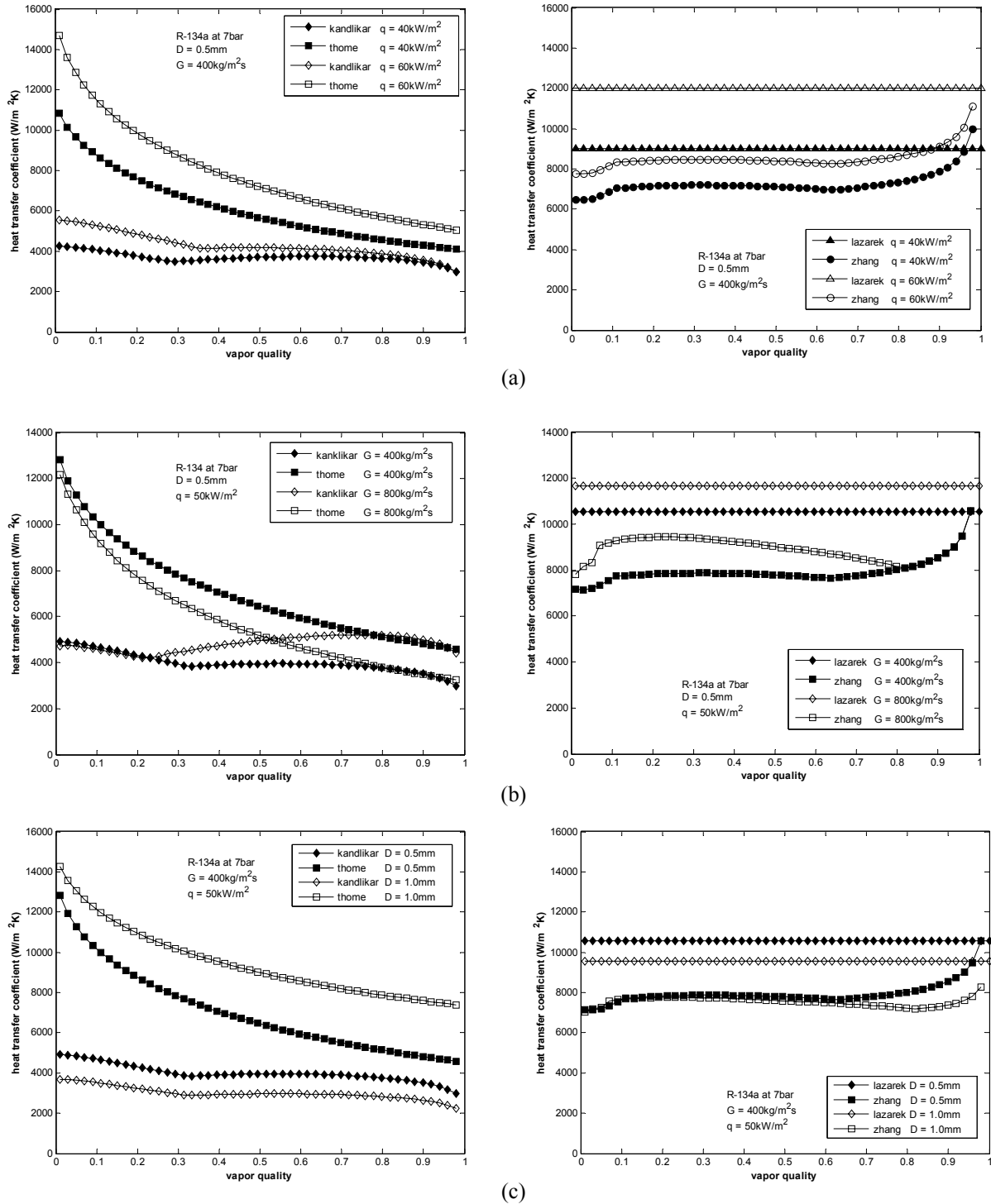


Figure 18. Predicted heat transfer coefficients versus vapor quality at different (a) heat fluxes, (b) mass velocities, (c) channel diameters, and (d) saturation pressures.

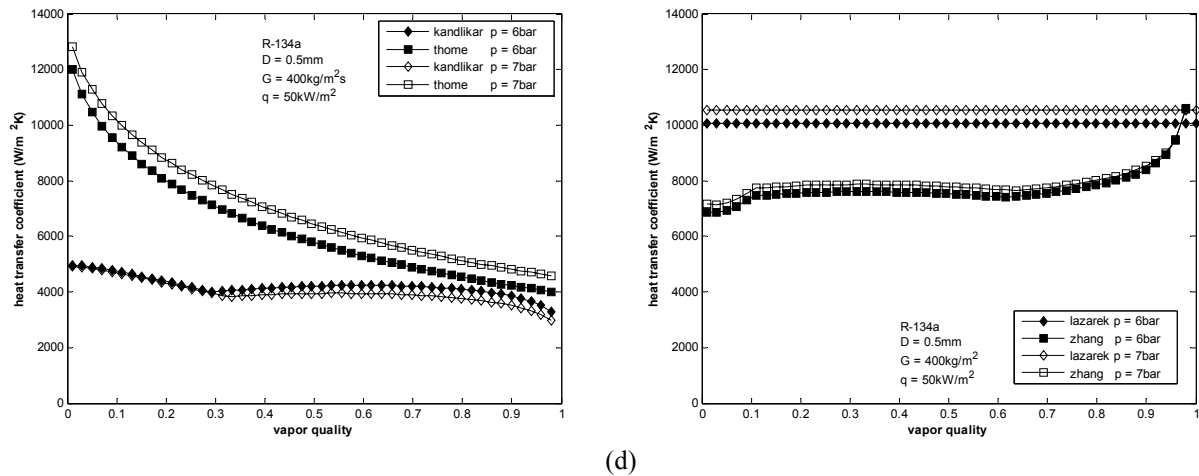


Figure 18. continued

quality, as in some of the experimental data mentioned previously. The correlations by Lazarek and Black and Tran *et al.* present no dependency of the heat transfer coefficient on vapor quality, while the method of Kandlikar and Balasubramanian gives the lowest predicted values. Figure 18 illustrates the changes in the heat transfer coefficient with heat flux, mass velocity, channel diameter and saturation pressure. While all the predicted coefficients increase with heat flux over vapor qualities from 0 to 1, substantial differences arise when varying the other parameters. For mass velocity, the three-zone model predicts a decrease in α with G , while by the other methods α is expected to improve with G . Similar differences occur when changing the channel diameter. While the three flow pattern independent correlations give an inverse relationship between heat transfer and channel diameter, the three-zone model shows higher values of α in larger channels. Finally, the Kandlikar-Balasubramanian correlation is the only one of the four that does not predict an improvement of heat transfer with saturation pressure.

2.6 Conclusive Remarks

The current review highlights that at the present state-of-the-art, numerous characteristic trends and effects have been observed in competing studies. An explanation for such dissimilar trends for what, at times, seem to be similar conditions is one of the objectives of this thesis. For example, the mixing of stable and unstable data may have created part of the confusion about the actual heat transfer tendencies (this aspect is examined in Chapter 5). From the modeling perspective, the approaches that have been proposed to date yield very different outcomes, as pointed out in the previous section. While those studies that suggest nucleate boiling as the dominant heat transfer mechanism, i.e. Lazarek and Black [5] and Tran *et al.* [25], provide an explanation to the data that show exclusively heat flux and property dependent heat transfer coefficients, they come short when it comes to different trends in the α - x plane. Furthermore, a strong presence of nucleate boiling is reasonably associated to a bubbly flow mode, which, for micro-channels, is seen to occur over an extremely limited vapor quality range (if not at very low mass velocities). The elongated bubble-slug flow approach of Thome and coworkers [12] agrees, at least qualitatively, with the quasi-invariant and decreasing trends in α versus x , and reproduces the increase in heat transfer with heat flux and physical properties. However, this approach relies on an accurate description of the temporal evolution of the local thickness of the liquid film, which for slug flow is extremely difficult to measure and thus reproduce on either a theoretical or empirical basis. Moreover, although some form of periodic dry-out may not be ruled out, the dry zones as described in [12] lack experimental proof. The three-zone

model is strictly a slug flow model, and, although extrapolating its results to ranges in vapor quality beyond the slug flow threshold is numerically possible, it is primarily applicable to this flow region. The two methods that extend macro-scale flow boiling correlations (Kandlikar and Balasubramanian [41] and Zhang *et al.* [42]) account for both nucleate boiling and convective evaporation. However, they are flow pattern independent, thus neglecting any heat transfer mechanism that may be characteristic to a specific flow mode, and rely on conclusions of proven validity only in the macro-scale.

Chapter 3

The Experimental Program

The present chapter defines the main aspects of the experimental program, which is aimed at providing a reliable database for two-phase micro-channel heat transfer for three different fluids: R-134a, R-236fa, and R-245fa. The first two sections that follow give a description of the test facility, while the remaining delineate the data reduction scheme, the experimental validation procedure, and give an analysis of the sources of error that may occur during data acquisition.

3.1 The Experimental Stand

The experimental test stand is illustrated in Fig. 19, and includes two pressurized vessels, a Coriolis Mass Flowmeter (CMF), a flow adjustment valve, and the test-section. All tubing, other than for the test-section, is 4mm in internal diameter. The flow is driven by the pressure difference between the two vessels, each of which contains a saturated liquid-vapor mixture of refrigerant. The vessels are thus maintained at different pressures/temperatures by means of external thermal regulating units that work with de-ionized water. This setup avoids having to use components with moving parts, i.e. a pump, which may induce undesirable vibrations. Saturated liquid, extracted from the bottom of the high pressure tank, crosses the CMF, enters the test-section through the valve, and is then directed into the low pressure vessel.

The inlet to the valve must be sub-cooled to avoid flashing. For this reason, the first tank (vessel A in Fig. 19) is always kept above ambient temperature. Heat is lost by the flow to the surroundings as it approaches the valve, where the liquid is at approximately ambient temperature, and an adequate degree of sub-cooling is generally guaranteed. If, however, flashing should occur, the

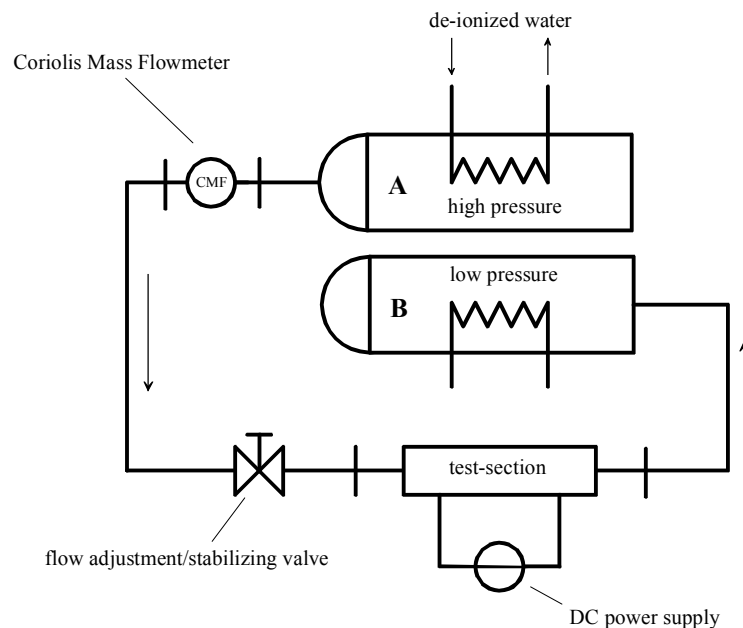


Figure 19. A schematic diagram of the experimental facility during data acquisition.

two-phase flow would be detected through a sight glass positioned immediately after the valve.

The operating conditions are set by acting on the temperature of the refrigerant within the two vessels, by adjusting the opening of the valve, and by regulating the current to the pre-heater and evaporator in the test-section (see Section 3.2 for a description of the test-section). The valve also has a stabilizing effect on the flow, avoiding the onset of (1) excursive (Ledinegg) instabilities, which may lead to critical conditions, and (2) oscillatory instabilities, by inhibiting back-flow of liquid.

Before starting any experimental run, vessel A is charged with refrigerant from vessel B, by an external pump. The pumping process is started after setting the operating temperatures in the two tanks, and after having connected them to ensure equal pressures, as shown in Fig. 20. During this stage, vessel B is always kept above ambient temperature to avoid vapor entering the pump. Once the filling procedure is completed, the connection with vessel B is closed, the pump is stopped and disconnected, and the two reservoirs are left to equilibrate at their respective temperatures.

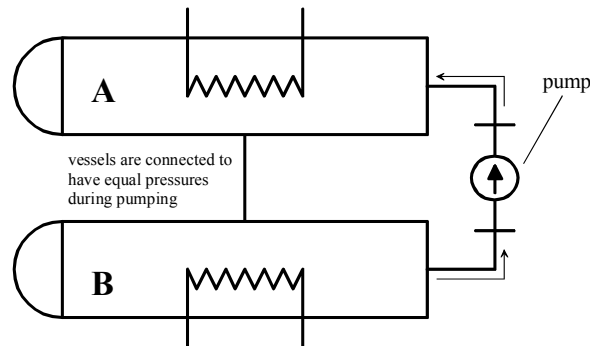


Figure 20. A schematic diagram of the pumping loop for charging of vessel A.

3.2 The Test-Section

The test-section, illustrated in Fig. 21a, includes the micro-channel, all the connections to the electric power supply units, and the instrumentation required for the measurements. The three main sectors to the test-section are (1) the pre-heater, for setting the desired inlet conditions to the evaporator, (2) the evaporator, where boiling occurs and heat transfer is measured, and (3) the glass tube for flow visualization. All three channels have the same sizes, and the junctions between each sector are manufactured to allow for precise alignment. Both the pre-heater and evaporator are made from stainless steel, and each has a pair of copper electrodes to electrically heat the channel and thus the flow (by a DC current). Two pressure taps are located immediately upstream and downstream of the test-section, while type K thermocouples (50 μ m leads) are positioned on the outer walls of both pre-heater and evaporator. The thermocouple leads are placed within individual support shells to avoid breakage, and the hot junctions are pressed against the tube wall through external springs thus reducing contact resistance (see Figs. 21b and 21c). A fine layer of insulating varnish is placed between the junction and the tube wall to avoid electrical disturbance.

Inlet and outlet fluid temperatures are obtained from wall temperature measurements taken at the two adiabatic locations before and after the heated lengths (see Fig. 21). The other thermocouples, positioned on the heated lengths (between the electrodes), provide the outer temperatures of the wall that are then used to evaluate the local heat transfer coefficients (inner wall temperatures are back-calculated from the measured values, as described in Section 3.3). The two pairs of electrodes (pre-heater and evaporator) are connected to two separate DC power supplies. The intensity of the applied

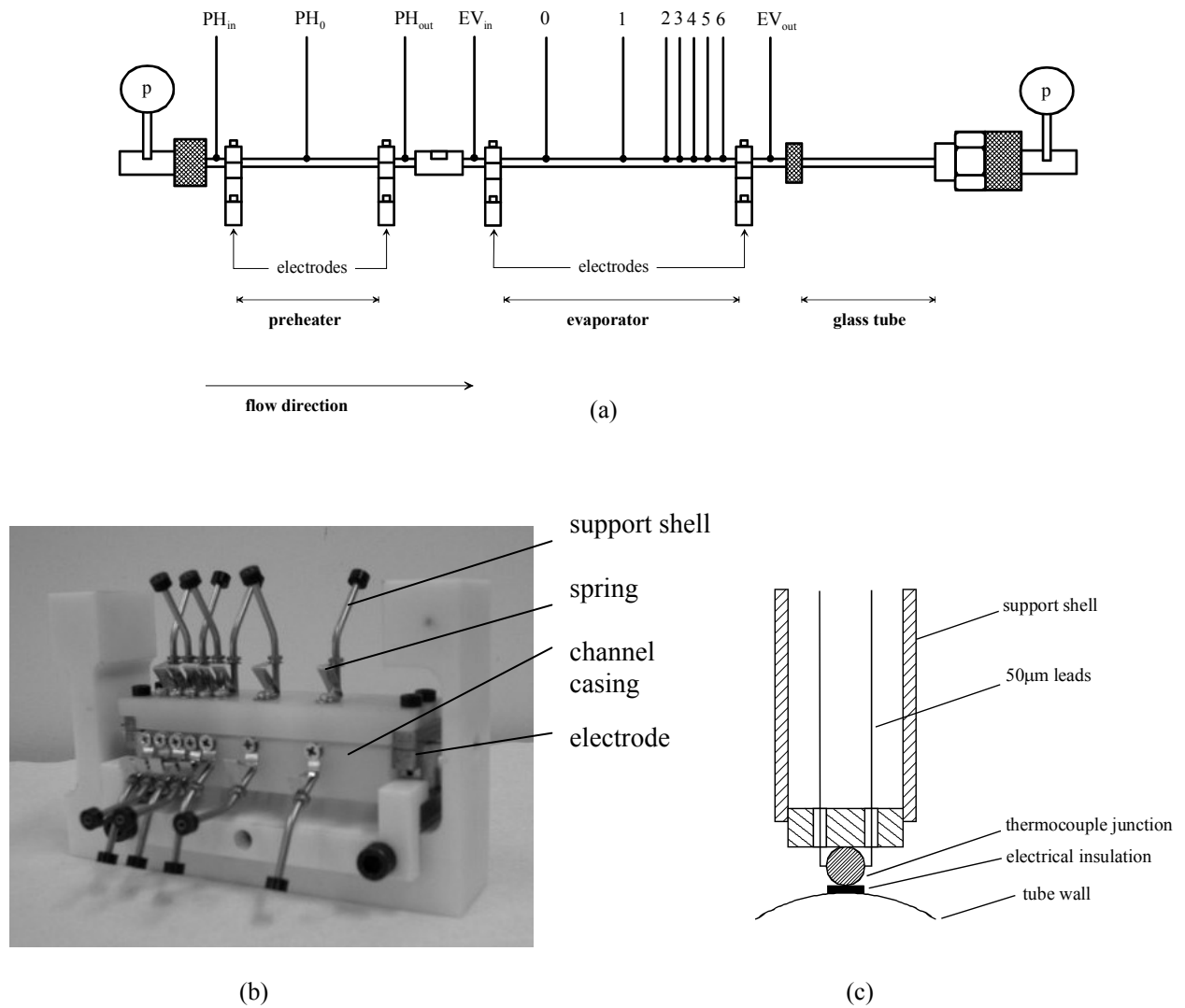


Figure 21. (a) Schematic diagram of the flow boiling test-section showing the two pressure taps (p) at the inlet and exit, and the locations of the pre-heater (PH) and evaporator (EV) thermocouples, (b) image of the evaporator, and (c) schematic diagram of an individual thermocouple on the test-section.

current is measured by a current intensity meter, while the voltage drop is measured directly at the electrodes. Tables 1, 2, and 3 illustrate all the technical specifications of the test-section.

The two measured inner diameters of the evaporator for the current study are of 510 and 790μm respectively (Table 1), and their interior roughness is measured by laser profilometry. Figure 22 shows the open section of the 510μm tube for the roughness measurement. The mean absolute roughness, R_a , is $2.41 \pm 0.12 \mu\text{m}$ for the 510μm channel, while $1.75 \pm 0.27 \mu\text{m}$ for the larger channel.

Table 1. Size and material characteristics of the evaporator and pre-heater tubes.

Tube Material	–	AISI 304
Inner Tube Diameters	μm	510 - 790
Outer Tube Diameters	μm	690 - 1000
Pre-Heater Heated Length	mm	43
Evaporator Heated Length	mm	75
Glass Tube Inner Diameter	μm	520 - 800
Glass Tube Length	mm	100

Table 2. Measurement instrumentation description and specifications.

Measured Quantity	Device	Manufacturer	Specifications
Pressure	Absolute Piezoelectric Transducer	Keller	0 – 10bar
Temperature	Type K Thermocouples	-	50μm diameter leads
Current	Z202A Current Intensity Meter	Grossen-Metrawatt	0 – 20A or 0 – 200A
Voltage Drop	PCI-6251 M Card & SCXI -1102C Module	National Instruments	±10V
Mass Flow Rate	CMF010 M	Micro Motion	

Table 3. Specifications for the power supply and data acquisition units.

Description	Device	Manufacturer	Specifications
Power Supply	DC Current Power Supply	Sorensen	0 – 8V and 0 – 125A
Data Acquisition	PCI-6251 M Card & SCXI -1102C Module & SCXI 1303 Terminal Block with Cold Junction Compensation	National Instruments	±100mV

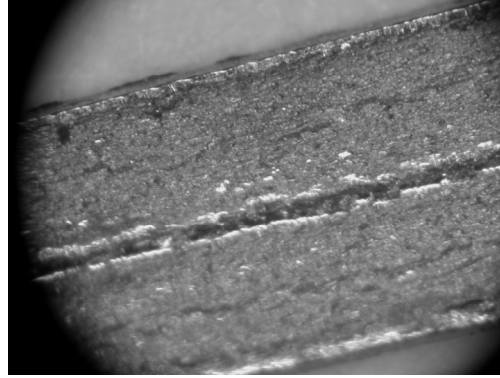


Figure 22. Magnified image of the open section of the 510μm micro-channel utilized for the measurement of inner roughness.

3.3 Data Reduction

Local heat transfer coefficients are evaluated at every temperature measurement point on the heated length of the evaporator. The heat transfer coefficient, α , is defined in terms of the magnitude of the inner wall heat flux (q), and the difference between the inner wall temperature (T_w) and that of the bulk fluid (T_f):

$$\alpha \equiv \frac{q}{T_w - T_f} \quad (3.1)$$

The temperature of the inner wall is derived from the measured values at the outer wall. Assuming the outer wall to be ideally adiabatic, and for steady-state conditions, a radial heat balance yields (see Fig. 23)

$$\frac{1}{r} \frac{d}{dr} \left(r \frac{dT}{dr} \right) + \frac{q_g'''}{k_w} = 0 \quad (3.2)$$

$$\frac{dT}{dr} = 0 \quad \text{and} \quad T = T_1 \quad \text{at} \quad r = R_1$$

with k_w the thermal conductivity of the wall, T_1 the temperature at the outer surface, and R_1 the outer radius of the tube. In Eq. (3.2), any heat transfer by axial conduction is neglected, and electrical heating of the tube material is accounted for by the volumetric heat generation term. Equation (3.2) may be solved by elementary methods to give the radial wall temperature distribution as

$$T(r) = T_1 + \frac{q_g'''}{4k_w} (R_1^2 - r^2) - \frac{q_g'''}{2k_w} R_1^2 \ln \left(\frac{R_1}{r} \right) \quad (3.3)$$

Inserting the inner tube radius, R , into Eq. (3.3) gives the corresponding temperature,

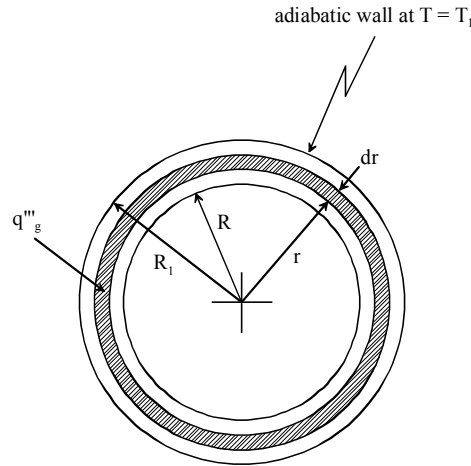


Figure 23. One-dimensional radial heat conduction model to assess the tube-side temperature.

$$T_w = T_1 + \frac{q_g'''}{4k_w}(R_i^2 - R^2) - \frac{q_g'''}{2k_w}R_i^2 \ln\left(\frac{R_i}{R}\right) \quad (3.4)$$

Equation (3.4) is thus used to correct the temperature readings of the thermocouples. The source term in Eq. (3.2) is evaluated from the voltage drop at the electrodes of the evaporator (ΔV), and the current intensity (I):

$$q_g''' = \frac{\eta I \Delta V}{\pi(R_i^2 - R^2)L} \quad (3.5)$$

with η the thermal efficiency of the system, which accounts for heat losses and is discussed in Section 3.4, and L the tube length. The wall heat flux is then given from Eqs. (3.3) and (3.5) as

$$q_w = -k_w \left. \frac{dT}{dr} \right|_{r=R} = -\frac{q_g'''}{2R}(R_i^2 - R^2) = -\frac{\eta I \Delta V}{2\pi R L} \quad \text{and} \quad q = |q_w| = \frac{\eta I \Delta V}{2\pi R L} \quad (3.6)$$

The effect of the adiabatic outer wall assumption in Eq. (3.2) on the estimated temperature of the inner wall is expected to yield negligible error. For the present operating conditions, and the 510 μm channel (100 μm wall thickness), assuming an outer wall temperature of 48°C (the upper limit on the wall temperature for the current study) and a tube-side heat flux of 73 kW/m², the temperature difference between the value given by Eq. (3.4) and that obtained assuming air-side free convection is of 0.02°C, thus well within the uncertainty of thermocouples. The correction applied in Eq. (3.6) through the thermal efficiency reduces this discrepancy to even lower values.

In most experiments, the exit to the pre-heater is sub-cooled. Thus the evaporator begins with a sub-cooled region followed by one in which the flow is saturated. Although zones with sub-cooled boiling or superheated liquid may also occur, the following procedure neglects their presence, assuming the flow to exhibit thermodynamic stability and equilibrium. The sub-cooled length, z_{sat} (having taken $z = 0$ at the entrance to the evaporator), and the local saturation pressure and temperature ($p = p_{\text{sat}}$ and $T = T_{\text{sat}}$ at $z = z_{\text{sat}}$) are given by the following set of equations:

$$q \pi D z_{\text{sat}} = \frac{1}{4} G \pi D^2 \int_{T_{\text{in}}}^{T_{\text{sat}}} c_p(p, T) dT \quad (3.7)$$

$$p_{\text{sat}} = p_{\text{in}} - 4f \left(\frac{z_{\text{sat}}}{D} \right) \frac{G^2}{2\rho_1} \quad (3.8)$$

$$T_{\text{sat}} = T_{\text{sat}}(p_{\text{sat}}) \quad (3.9)$$

Equation (3.7) is an energy balance over the sub-cooled length, with c_p the specific heat of the liquid expressed by a third degree polynomial of the local temperature (the effect of pressure is neglected). Equation (3.8) gives the pressure drop experienced by the sub-cooled liquid flow, where f is Fanning's friction factor, computed as $16/\text{Re}$ for laminar flow, or, in the case of turbulent flow, as $0.079/\text{Re}^{0.25}$ (Blasius' expression for smooth tubes). The third equation, Eq. (3.9), yields the saturation temperature as a function of pressure, and, as in the case of c_p , a third degree polynomial accurately represents the dependency in the range of conditions tested. The values of the three unknowns, namely z_{sat} , T_{sat} , and p_{sat} , are given by the simultaneous solution of the above set equations.

The evaporation of the flow is assumed to start at $z = z_{\text{sat}}$, where the local vapor quality is zero. Beyond z_{sat} , the saturated two-phase flow experiences an increase in vapor fraction primarily due to heating, although frictional and momentum pressure losses also contribute. The vapor quality, defined as the ratio of the flow rate of the vapor phase to the total mass flow rate, may be expressed in terms of local enthalpies, i.e.

$$x = \frac{h - h_l}{h_{lv}} \quad (3.10)$$

where h_l and h_{lv} are respectively the liquid specific enthalpy and the latent heat of vaporization computed at the local pressure. Equation (3.10) allows extending the concept of vapor quality to sub-cooled liquid flows, in which case it will assume negative values. The enthalpy of the fluid, h , at a location z along the channel is given by the energy balance

$$h(z) = \frac{4q}{GD} z + h_{\text{in}} \quad (3.11)$$

with h_{in} the specific enthalpy of the flow at the entrance to the evaporator (at $z = 0$). Equation (3.11) neglects the change in kinetic energy of the vaporizing flow, since it is generally small compared to the other contributions.

In order to assess the fluid properties in Eq. (3.10), and to estimate the local temperature of the two-phase flow, an expression for the pressure gradient in the saturated length must be supplied. At present however, no reliable pressure drop models or correlations are available for micro-channel two-phase flows. In this study the two-phase pressure gradient is assumed to be constant, and the local pressure is given by a linear law as

$$p(z) = p_{\text{out}} + \frac{p_{\text{sat}} - p_{\text{out}}}{z_{\text{sat}} - L} (z - L) \quad (3.12)$$

with p_{sat} the pressure at $z = z_{\text{sat}}$, as calculated from Eq. (3.8), and p_{out} the outlet pressure. The pressure p_{out} is known from the measured value of the outlet temperature, and Eq. (3.12) may thus be used to compute the local fluid temperature through the same polynomial as in Eq. (3.9).

3.4 Experimental Validation and Uncertainty

Assessing Heat Losses

Although the thermal resistance of the flow is relatively low, part of the supplied heat is dissipated elsewhere. There are five main sources of heat losses from the channel: (1) heat losses by natural convection to the surrounding ambient, (2) heat removed by axial conduction at the channel entrance and exit, (3) heat conducted through the copper electrodes that provide current to the steel tube, (4) heat conducted through the thermocouple lead wires, and (5) radiation heat losses to the ambient. The last three sources for heat losses may be neglected for the present experimental conditions, since the operating temperatures are fairly close to the ambient temperature ($T_1 \leq 48^\circ\text{C}$) and the cross-sectional area of the thermocouple leads is very small ($50\mu\text{m}$ diameter wires and a low fin efficiency). The overall heat loss, \dot{Q}_{loss} , from the evaporator may be therefore expressed as:

$$\dot{Q}_{\text{loss}} \cong \dot{Q}_{\text{cond}} + \dot{Q}_{\text{conv}} \quad (3.13)$$

where the first term on the right hand side of Eq. (3.13) refers to the losses by longitudinal conduction at the extremities of the evaporator, while the second refers to those due to natural convection. Defining the heating efficiency, η , as

$$\eta = \frac{\dot{Q}}{I\Delta V} = 1 - \frac{\dot{Q}_{\text{loss}}}{I\Delta V} \quad (3.14)$$

where \dot{Q} is the thermal power delivered to the flow, while $I\Delta V$ is the heating rate by Joule effect, Eq. (3.13) may be rewritten as

$$\eta = 1 - \varepsilon_{\text{cond}} - \varepsilon_{\text{conv}} \quad \text{with} \quad \varepsilon_{\text{cond}} = \frac{\dot{Q}_{\text{cond}}}{I\Delta V} \quad \text{and} \quad \varepsilon_{\text{conv}} = \frac{\dot{Q}_{\text{conv}}}{I\Delta V} \quad (3.15)$$

In order to provide an estimate to the relative losses by conduction, consider the system illustrated in Fig. 24. The tube in Fig. 24 is exposed to uniform generation of heat, an adiabatic outer wall, tube-side convection, and imposed temperatures at the inlet and outlet cross-sections. The one-dimensional longitudinal conductive heat transfer problem is stated as follows:

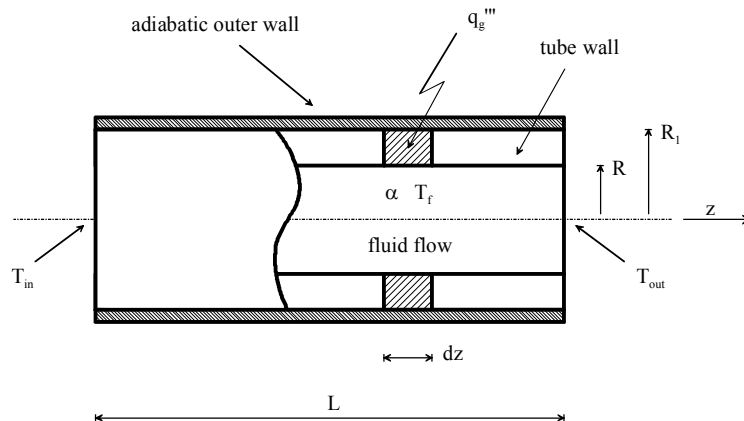


Figure 24. Schematic of the system for the assessment of conductive heat losses.

$$\frac{d^2 T}{dz^2} - \frac{\alpha}{k_w} \left(\frac{2R}{R_1^2 - R^2} \right) T = -\frac{q_g'''}{k_w} - \frac{\alpha}{k_w} \left(\frac{2R}{R_1^2 - R^2} \right) T_f(z)$$

$$T(z=0) = T_{in} \quad (3.16)$$

$$T(z=L) = T_{out}$$

Assuming a linear change in fluid temperature, i.e.

$$T_f(z) = T_{in} + \left(\frac{T_{out} - T_{in}}{L} \right) z \quad (3.17)$$

Eq. (3.16) may be solved as

$$T(z) = -\left(\frac{R_1^2 - R^2}{2R} \right) \frac{q_g'''}{\alpha} \frac{1}{\sinh \left[\sqrt{\frac{\alpha}{k_w} \left(\frac{2L^2 R}{R_1^2 - R^2} \right)} \right]} \left[\sinh \left(\sqrt{\frac{\alpha}{k_w} \frac{2R}{R_1^2 - R^2}} (L-z) \right) + \sinh \left(\sqrt{\frac{\alpha}{k_w} \frac{2R}{R_1^2 - R^2}} z \right) \right] + T_p(z) \quad (3.18)$$

with

$$T_p(z) = \frac{q_g'''}{\alpha} \left(\frac{R_1^2 - R^2}{2R} \right) + T_f(z) \quad (3.19)$$

Figure 25 shows the wall temperature, Eq. (3.18), and fluid temperature, Eq. (3.17), for the cases where $T_{in} < T_{out}$, as approximately occurs during single-phase heating, and $T_{in} = T_{out}$, as in an ideal saturated two-phase flow (neglecting pressure drop) with a constant heat transfer coefficient. The relative heat loss by conduction may thus be estimated by calculating the axial flow of heat at the extremities of the tube (at $z=0$ and $z=L$). Applying the definition of ε_{cond} , as in Eq. (3.15),

$$\varepsilon_{cond} = \frac{k_w}{q_g''' L} \left(\left. \frac{dT}{dz} \right|_{z=0} - \left. \frac{dT}{dz} \right|_{z=L} \right) \quad (3.20)$$

From the expression in Eq. (3.18), Eq. (3.20) gives

$$\varepsilon_{cond} = 2 \frac{\cosh(\sqrt{Bi}) - 1}{\sqrt{Bi} \sinh(\sqrt{Bi})} \quad \text{with} \quad Bi = \frac{\alpha}{k_w} \left(\frac{2L^2 R}{R_1^2 - R^2} \right) \quad (3.21)$$

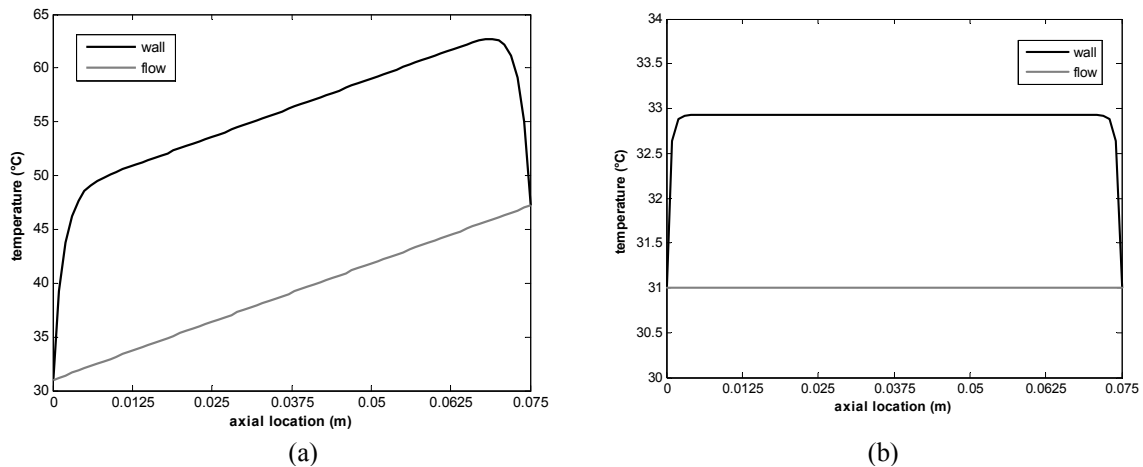


Figure 25. Axial wall temperature distribution as given by Eq. (3.18) for a flow of R-134a with a mass velocity of $500 \text{ kg/m}^2\text{s}$ and an inlet temperature of 31°C : (a) a linear increase in flow temperature with $\alpha = 785 \text{ W/m}^2\text{K}$ and $\varepsilon_{\text{cond}} = 4\%$, and (b) a constant temperature flow with $\alpha = 7000 \text{ W/m}^2\text{K}$ and $\varepsilon_{\text{cond}} < 0.5\%$. Values for a 75mm long stainless steel tube with an inner tube diameter of $500 \mu\text{m}$, a wall thickness of $100 \mu\text{m}$, and experiencing uniform heat generation of 113 W/cm^3 .

the tube Biot number. Equation (3.21), shown graphically in Fig. 26, is thus representative of the relative losses by conduction for a circular channel, perfectly insulated at the outer wall, exposed to a flow that experiences either a linear or no change in temperature, in the approximation of one-dimensional conductive heat transfer.

Assuming an adiabatic outer wall is however a rough approximation, since the test-section is always subjected to free convection. The variable axial wall temperature profile of the test-section, and the generally low ΔT between tube and ambient (especially during boiling experiments, when the tube-side heat transfer coefficient is relatively high), makes the prediction of the heat losses by convection a difficult task. An approximate value of the air-side convective Nusselt number is given

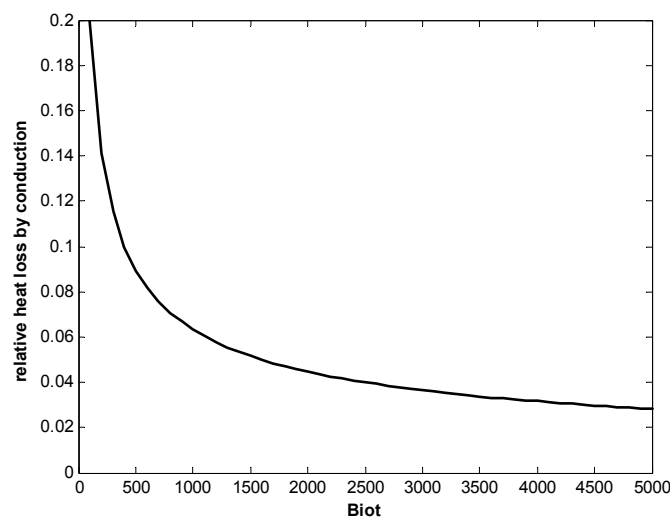


Figure 26. Relative losses by conduction versus the tube Biot number, as predicted by Eq. (3.21).

by the Churchill and Chu [43] correlation developed for horizontal isothermal cylinders ($10^{-5} < Ra < 10^{12}$),

$$Nu_{\infty} = \left\{ 0.60 + \frac{0.387 Ra^{1/6}}{\left[1 + \left(\frac{0.559}{Pr} \right)^{9/16} \right]^{8/27}} \right\}^2 \quad (3.22)$$

evaluated at the average outer wall temperature of the tube, \bar{T}_1 . The Rayleigh number in Eq. (3.22) is defined as

$$Ra = \frac{\beta g (\bar{T}_1 - T_{\infty}) D_1^3}{\nu \alpha} \quad (3.23)$$

with D_1 the outer diameter of the tube, T_{∞} the ambient temperature, and Pr , β , ν , and α respectively the Prandtl number, the volumetric expansion coefficient, the kinematic viscosity, and the thermal diffusivity of air calculated at the film temperature $T_{\text{film}} = (\bar{T}_1 + T_{\infty})/2$. From Eq. (3.15),

$$\epsilon_{\text{conv}} = \frac{C_1 Nu_{\infty} k_{\infty} \pi L (\bar{T}_1 - T_{\infty})}{I \Delta V} \quad (3.24)$$

with C_1 a correction factor that accounts for the non-uniformities in the wall temperature that may be due to the flow characteristics and to the presence of any component in contact with the test-section, i.e. measurement instrumentation, thermocouple supports, electrodes etc.

Single-phase flow experimentation allows an indirect measurement of η , since assessing the effective heat input to the flow simply requires the flow rate, the specific heat of the fluid, and the inlet and exit fluid temperatures. Figure 27 illustrates one set of heat balance results for an experiment on a sub-cooled liquid flow of R-134a. The plot, which shows η as a function of the electrical heat input ($I \Delta V$), presents an average thermal efficiency of 82%. When performing single-phase tests on heat

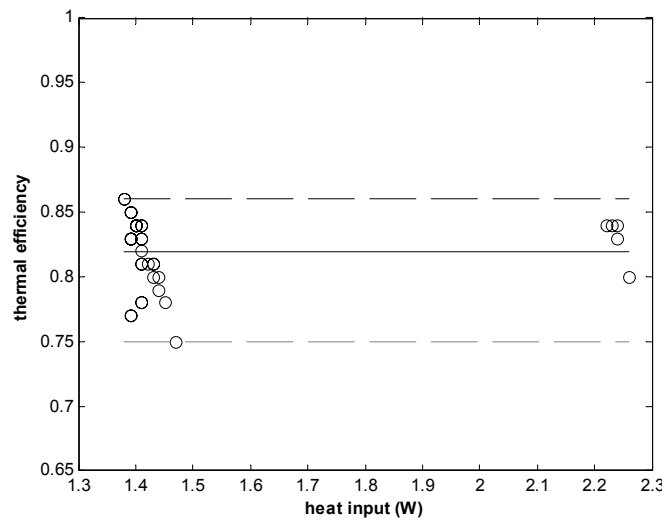


Figure 27. Single-phase heat balance for a sub-cooled liquid flow of R-134a in the 510 μ m tube.

dissipation, the level of heat flux is limited in order to maintain the wall below the corresponding fluid saturation temperature, thus avoiding the onset of sub-cooled boiling. The measured thermal efficiencies are then compared to the predictions by Eqs. (3.15), (3.21) and (3.24). Assuming the error on η to fall almost entirely on the convective contribution, the value of C_1 in Eq. (3.24) is set to provide the best fit to single-phase data. Equations (3.15), (3.21) and (3.24) are then adopted in the calculation of the wall heat flux, Eq. (3.6), during boiling tests, utilizing current wall and ambient temperatures, and applied electrical heat inputs.

Single-Phase Heat Transfer

Research on single-phase micro-channel flows has been directed to verify whether confinement induces any differences in heat transfer and pressure drop with respect to conventional theory for macro-scale systems. Although at present the issue is not entirely resolved, several recent investigations (see [44]) have provided evidence to support the conclusion that the underlying mechanisms remain unaltered. From this perspective, numerous single-phase heat transfer experiments have been performed in the present study to validate the test setup prior to the two-phase measurements. Figure 28 presents results for liquid flows of R-134a and R-245fa. Generally the data in the transition-turbulent region give satisfactory agreement with well-established single-phase correlations. When compared to the Gnielinski and Dittus-Boelter correlations, the average experimental Nusselt numbers position themselves in between the two-predictions, and the slight discrepancy may be attributed to the uncertainty in the measurement (discussed below).

As shown in Fig. 28, the correspondence with conventional theory is not as good for laminar flows. In this case, the tests are performed at extremely low heating rates, because of the limit to the degree of sub-cooling at the inlet to the test-section that can presently be obtained (the lowest temperature achievable is ambient temperature). Under these conditions, the extent of the tube experiencing an effect of longitudinal conduction may be significant, and the assumption of a uniform wall heat flux becomes questionable. In addition, in laminar mode the developing length of the flow may cover a substantial part of the channel, making the predictions for fully-developed flows misleading.

Figure 29 presents wall temperature data (corrected through Eq. (3.4)) and the corresponding heat transfer coefficients for a single-phase flow experiment. The last thermocouple on the heated

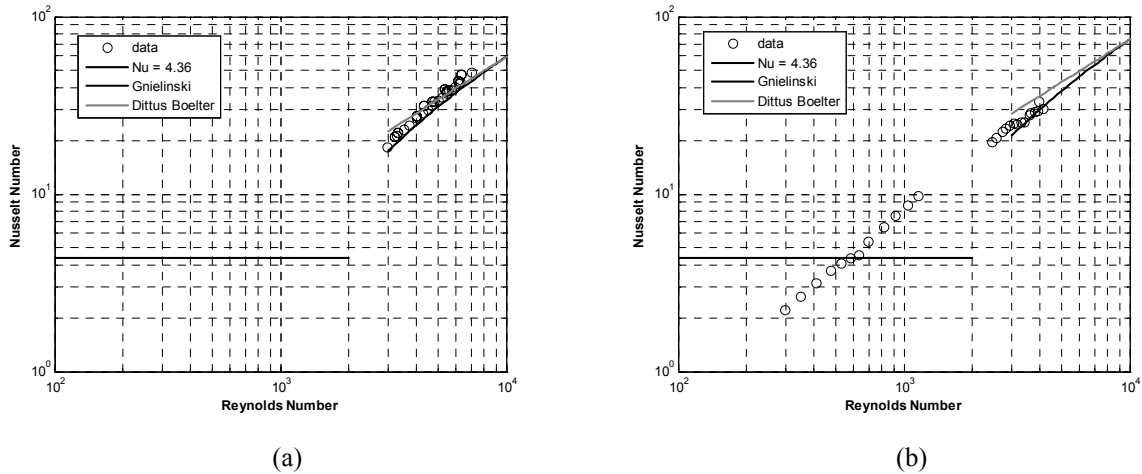


Figure 28. Single-phase Nusselt numbers for sub-cooled liquid flows of (a) R-134a, and (b) R-245fa in 510 μ m tubes. Data is compared to the Gnielinski and Dittus-Boelter correlations for $Re > 3000$, and conventional laminar flow theory for $Re < 2000$.

(evaporator) length generally experiences an effect of axial conduction, giving lower values than expected, and is therefore not used during two-phase testing. Since the only two thermocouples measuring fluid temperature are the ones at the inlet and outlet to the evaporator, the local temperatures shown in Fig. 29a are computed by an energy balance, similar to that in Eq. (3.7).

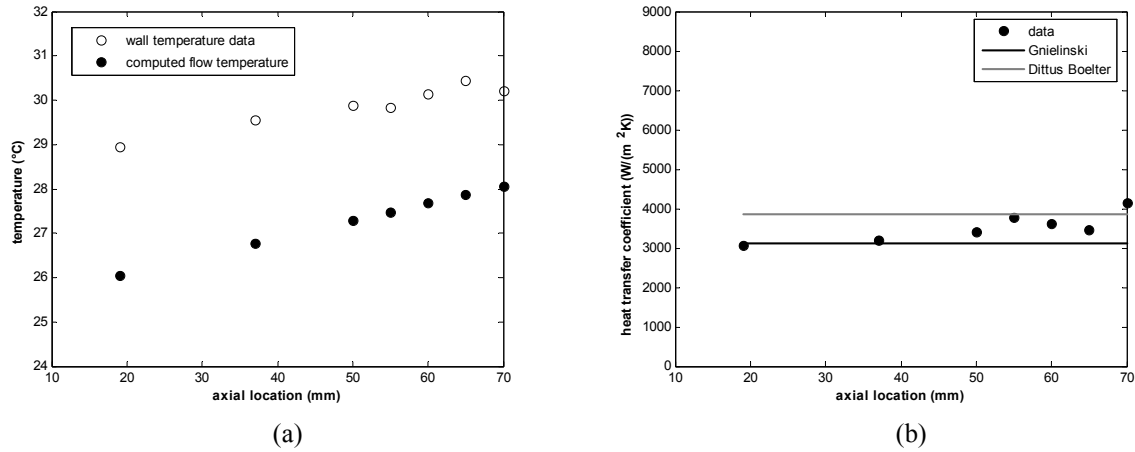


Figure 29. Data for sub-cooled liquid R-134a flowing with a mass velocity of 1235 kg/m²s ($Re = 3200$), and an applied heat flux of 8.90 kW/m²: (a) inner wall temperature data and computed flow temperature, and (b) measured local heat transfer coefficients compared to conventional correlations.

Error Analysis

The error on any directly measured physical quantity is determined utilizing the indication of the probe manufacturer and through analysis based on in-house calibration and data regression, with a 68% confidence interval. Conventional theory on error propagation is then applied to all derived parameters.

Thermocouple Temperatures

All thermocouples are calibrated before insertion onto the test-section. The calibration includes (1) positioning the sensors in a thermally controlled liquid bath, (2) varying the bath's temperature within predetermined limits, and (3) recording the readings from the thermocouples and from a set of reference thermometers. In the present investigation the calibration temperatures range from 20 to 48°C, with a step of 4°C, and yield two data sets: one including fifteen² uncalibrated values, $\{\theta_i\}$, as given by the acquisition software, and the other comprised of an equal number of reference temperatures, $\{T_i\}$. The two sets are then correlated linearly through least-squares fitting, i.e. (see Fig. 30)

$$\theta = A + BT \quad (3.25)$$

with the two coefficients given as

² The calibration interval was covered incrementing the temperature to 48°C, and then descending back to 20°C, by steps of 4°C.

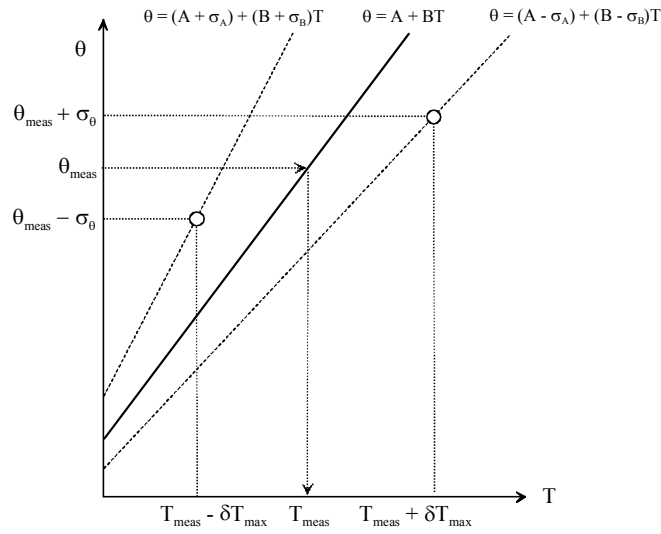


Figure 30. Graphical representation of the procedure for measuring temperatures from uncalibrated thermocouple readings. Note that $\delta T \leq \delta T_{\max}$, for δT given by Eq. (3.30).

$$A = \frac{\sum T^2 \sum \theta - \sum T \sum T\theta}{N \sum T^2 - (\sum T)^2} \quad \text{and} \quad B = \frac{N \sum T\theta - \sum T \sum \theta}{N \sum T^2 - (\sum T)^2} \quad (3.26)$$

and $N = 15$. Neglecting the uncertainty on the platinum reference probes ($\pm 0.025^\circ\text{C}$ as reported by the manufacturer), and assuming the uncalibrated temperatures to distribute themselves normally around the calibration line, the average deviation of the $\{\theta_i\}$ values from Eq. (3.25) is

$$\sigma_\theta = \sqrt{\frac{1}{N-2} \sum_{i=1}^N (\theta_i - A - BT_i)^2} \quad (3.27)$$

and is taken as the value for the uncertainty on θ . By error propagation on Eq. (3.26), the uncertainties on A and B are

$$\sigma_A = \sigma_\theta \sqrt{\frac{\sum T^2}{N \sum T^2 - (\sum T)^2}} \quad \text{and} \quad \sigma_B = \sigma_\theta \sqrt{\frac{N}{N \sum T^2 - (\sum T)^2}} \quad (3.28)$$

When performing a measurement, the uncalibrated temperature, θ_{meas} , will be thus converted to the calibrated “true” value, T_{meas} , through the inverse expression of Eq. (3.25):

$$T_{\text{meas}} = \frac{1}{B} \theta_{\text{meas}} - \frac{A}{B} \quad (3.29)$$

and its uncertainty will be

$$\delta T = \sqrt{\left(\frac{\partial T}{\partial \theta} \sigma_\theta \right)^2 + \left(\frac{\partial T}{\partial A} \sigma_A \right)^2 + \left(\frac{\partial T}{\partial B} \sigma_B \right)^2} \quad (3.30)$$

Figure 30 shows a graphical representation of the above procedure.

The last partial derivative in Eq. (3.30) is dependent on the value of θ : $\partial T/\partial B = (A - \theta)/B^2$, and will yield an increasing uncertainty with temperature. Setting the upper limit to θ equal to the highest calibration temperature value, 48°C, the corresponding δT from the entire set of thermocouples is shown in Table 4. The two thermocouples with the highest uncertainties, $\pm 0.19^\circ\text{C}$, are removed during two-phase flow experiments (one is used as the last thermocouple on the heated length during single-phase tests). Thus, of the thermocouples used in the two-phase experiments, the highest uncertainty is $\pm 0.15^\circ\text{C}$.

Table 4. The uncertainties for the set of thermocouples used during heat transfer data acquisitions.

thermocouple channel number	1	3	4	6	7	9	10	11	12	13	24	25
δT ($^\circ\text{C}$)	0.19	0.13	0.19	0.14	0.15	0.12	0.12	0.09	0.09	0.12	0.15	0.14

Channel Diameters and Length

The inner diameter of the channel is assessed using measurement needles of increasing sizes. The needles are fit into the two ends of the tube, and their size is gradually increased to the point where insertion is no longer possible. Each size step is an added $10\mu\text{m}$ in diameter. The nominal values of the two tubes tested are 500 and $800\mu\text{m}$, and size measurements are performed on all tubes within the same group (determined by nominal size) provided by the manufacturer. All the tubes present excellent size uniformity, with the following mean values and corresponding uncertainties:

$$(i) \quad D = 510\mu\text{m} \pm 10\mu\text{m} \quad \text{and} \quad (ii) \quad D = 790\mu\text{m} \pm 10\mu\text{m} \quad (3.31)$$

The uncertainty, $\pm 10\mu\text{m}$, is set to the smallest scale of the measurement needle.

The outer tube diameters are measured utilizing a micro-metric caliper that also has an uncertainty of $\pm 10\mu\text{m}$. For the two tubes:

$$(i) \quad D_1 = 690\mu\text{m} \pm 10\mu\text{m} \quad \text{and} \quad (ii) \quad D_1 = 1000\mu\text{m} \pm 10\mu\text{m} \quad (3.32)$$

The tube length is defined as the length between the two inner walls of the copper electrodes. The measurement is made with a Vernier caliper, and yields

$$L = 75.0\text{mm} \pm 0.5\text{mm} \quad (3.33)$$

Current and Voltage Drop

The current probe is based on Hall Effect technology, allowing a non-intrusive intensity measurement with an accuracy of

$$\delta I = 0.01I + 0.03 \quad (3.34)$$

as specified by the manufacturer for currents below 20A.

The value of the voltage drop across the electrodes is measured directly through the acquisition box, utilizing an input module with an accuracy of 0.035% of the reading within a $\pm 10\text{V}$ range:

$$\delta(\Delta V) = 0.00035 \Delta V \quad (3.35)$$

The bias limit (the magnitude of the fixed constant error) for the measured currents and voltages, given in Eqs. (3.34) and (3.35), are generally much larger than the values deriving from the statistical results for the precision limit, and are thus taken as the uncertainties on both parameters.

Flow Rate and Mass Velocity

The base accuracy on the reading of the CMF is given on the instrument's calibration certificate to be $\pm 0.044\%$. In order to account for flow rates that may be lower than the standard calibration values, the uncertainty is computed through the following equation

$$\frac{\delta \dot{m}}{\dot{m}} = 0.00044 + \frac{5.56 \times 10^{-7}}{\dot{m}} \quad (3.36)$$

where the first constant is the base accuracy, while the second ($5.56 \times 10^{-7} \text{ kg/s}$) is the zero stability value as given by the manufacturer. For a flow rate corresponding to a mass velocity of $500 \text{ kg/m}^2\text{s}$ in a $510 \mu\text{m}$ channel, Eq. (3.36) yields $\pm 0.60\%$.

The error on the mass velocity is estimated from its definition, $G \equiv 4\dot{m}/(\pi D^2)$, as

$$\delta G = \sqrt{\left(\frac{\partial G}{\partial \dot{m}} \delta \dot{m}\right)^2 + \left(\frac{\partial G}{\partial D} \delta D\right)^2} = G \sqrt{\left(\frac{\delta \dot{m}}{\dot{m}}\right)^2 + \left(2 \frac{\delta D}{D}\right)^2} \quad (3.37)$$

Figure 31 shows the fractional uncertainty, $\delta G/G$, as a function of mass velocity for the two channel sizes tested. The lowest mass velocity used in the flow boiling test matrix was in fact $300 \text{ kg/m}^2\text{s}$ for both channels.

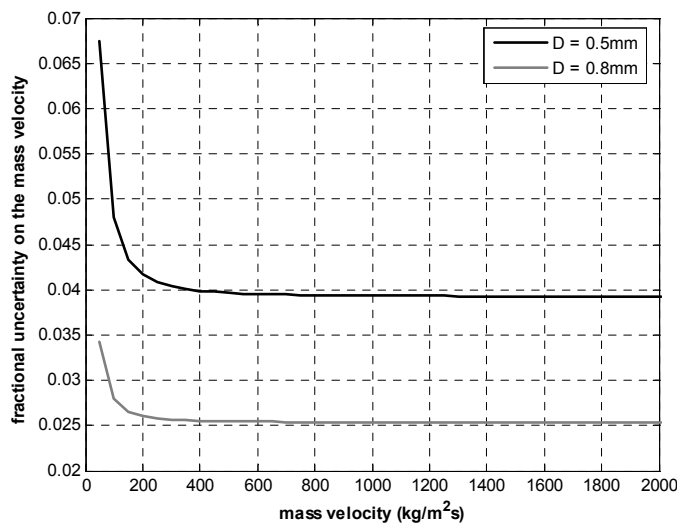


Figure 31. Fractional uncertainty on the measured mass velocity for two tube sizes.

Heating Efficiency and Heat Flux

As mentioned earlier, numerous single-phase experiments were performed in order to assess the sensitivity of the test-section to heat losses. The energy balances measured during single-phase tests provide an estimate to the value of C_1 in Eq. (3.24), and the value of η during two-phase runs is then computed from Eqs. (3.15), (3.21), and (3.24). The heating efficiency is thus subjected to error mainly deriving from the measured temperature difference between wall and ambient, the tube size, and the C_1 factor. Neglecting the contribution from the conductive term, $\varepsilon_{\text{cond}}$, and referring to Eqs. (3.15) and (3.24),

$$\delta\eta \cong \delta\varepsilon_{\text{conv}} = \sqrt{\left(\frac{\partial\varepsilon_{\text{conv}}}{\partial C_1} \delta C_1\right)^2 + \left(\frac{\partial\varepsilon_{\text{conv}}}{\partial D_1} \delta D_1\right)^2 + \left(\frac{\partial\varepsilon_{\text{conv}}}{\partial(\bar{T}_1 - T_\infty)} \delta(\bar{T}_1 - T_\infty)\right)^2} \quad (3.38)$$

The uncertainty on C_1 is estimated as the standard deviation from the set of values measured during single-phase tests. Assuming a normal distribution around the average, the data usually present a scatter with a 10% deviation: $\delta C_1/C_1 \approx 10\%$. The uncertainty on the temperature difference is taken as the sum of the uncertainties on the wall and ambient values. The accuracy on the ambient temperature is estimated to be $\pm 0.3^\circ\text{C}$, while for the tube wall, $\delta\bar{T}_1 = 0.15^\circ\text{C}$, as given in Table 4 (excluding the two thermocouples with highest uncertainties). The fractional uncertainty $\delta\eta/\eta$ generally decreases as the heat balance improves, as shown in Fig. 32a for a set of boiling experiments for R-134a.

As for the heat flux, standard error propagation theory applied to Eq. (3.6) yields

$$\frac{\delta q}{q} = \sqrt{\left(\frac{\delta\eta}{\eta}\right)^2 + \left(\frac{\delta I}{I}\right)^2 + \left(\frac{\delta(\Delta V)}{\Delta V}\right)^2 + \left(\frac{\delta D}{D}\right)^2 + \left(\frac{\delta L}{L}\right)^2} \quad (3.39)$$

As the magnitude of the heat flux increases, the relative uncertainty decreases (see Fig. 32b).

Local Pressure

Equation (3.12) gives the local pressure of the two-phase flow as a function of the saturation pressure, p_{sat} , and length, z_{sat} , as well as the downstream coordinate, z , and the fluid outlet pressure, p_{out} . Thus

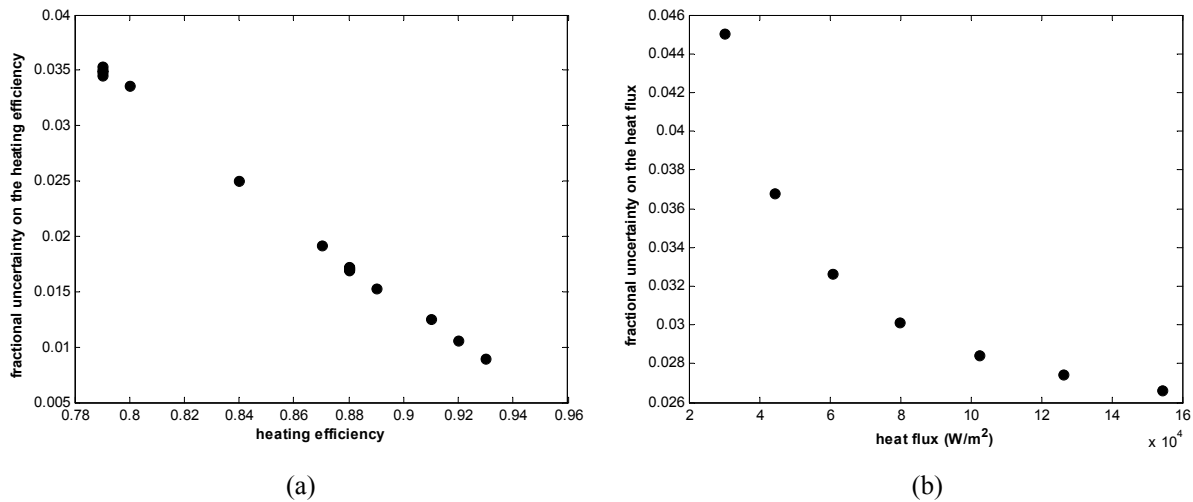


Figure 32. Relative errors on (a) the heating efficiency and (b) the heat flux for flow boiling of R-134a in the $510\mu\text{m}$ channel, at a saturation temperature of 31°C and a mass velocity of $964\text{kg/m}^2\text{s}$.

$$\delta p = \sqrt{\left(\frac{\partial p}{\partial p_{\text{sat}}} \delta p_{\text{sat}}\right)^2 + \left(\frac{\partial p}{\partial z_{\text{sat}}} \delta z_{\text{sat}}\right)^2 + \left(\frac{\partial p}{\partial p_{\text{out}}} \delta p_{\text{out}}\right)^2 + \left(\frac{\partial p}{\partial z} \delta z\right)^2 + \left(\frac{\partial p}{\partial L} \delta L\right)^2} \quad (3.40)$$

The errors on the saturation parameters are derived from Eqs. (3.7), (3.8) and (3.9) as

$$\delta z_{\text{sat}} \leq \frac{\partial z_{\text{sat}}}{\partial G} \delta G + \frac{\partial z_{\text{sat}}}{\partial D} \delta D + \frac{\partial z_{\text{sat}}}{\partial q} \delta q + \frac{\partial z_{\text{sat}}}{\partial T_{\text{sat}}} \frac{dT_{\text{sat}}}{dp_{\text{sat}}} \delta p_{\text{sat}} + \frac{\partial z_{\text{sat}}}{\partial T_{\text{in}}} \delta T_{\text{in}} \quad (3.41)$$

$$\delta p_{\text{sat}} \leq \frac{\partial p_{\text{sat}}}{\partial p_{\text{in}}} \delta p_{\text{in}} + \frac{\partial p_{\text{sat}}}{\partial G} \delta G + \frac{\partial p_{\text{sat}}}{\partial D} \delta D + \frac{\partial p_{\text{sat}}}{\partial z_{\text{sat}}} \delta z_{\text{sat}} + \frac{\partial p_{\text{sat}}}{\partial \rho_1} \delta \rho_1 + \frac{\partial p_{\text{sat}}}{\partial \mu_1} \delta \mu_1$$

having set $\delta T_{\text{sat}} = (dT_{\text{sat}}/dp_{\text{sat}})\delta p_{\text{sat}}$. Equations (3.41) imply using the explicit expression for the friction factor, since it isn't an independent quantity. Replacing the inequalities with equalities, the above two equations form a linear system in the two unknowns: δz_{sat} and δp_{sat} . The uncertainty on the inlet temperature, T_{in} , is taken as $\pm 0.15^\circ\text{C}$, while the errors on the physical parameters are computed from their third degree polynomials. For example, the liquid viscosity, given as

$$\mu_1 = b_1 + b_2 \left(\frac{T_{\text{in}} + T_{\text{sat}}}{2} \right) + b_3 \left(\frac{T_{\text{in}} + T_{\text{sat}}}{2} \right)^2 + b_4 \left(\frac{T_{\text{in}} + T_{\text{sat}}}{2} \right)^3 \quad (3.42)$$

with b_1, b_2, b_3 , and b_4 the fitting coefficients, will have the following uncertainty:

$$\delta \mu_1 \leq \frac{\partial \mu_1}{\partial T_{\text{in}}} \delta T_{\text{in}} + \frac{\partial \mu_1}{\partial T_{\text{sat}}} \frac{dT_{\text{sat}}}{dp_{\text{sat}}} \delta p_{\text{sat}} \quad (3.43)$$

As for Eqs. (3.41), changing the inequality in Eq. (3.43) to an equality will maintain the above system linear.

As for the error on the inlet pressure, the fluid pressure at the inlet to the test-section is measured with a piezoelectric transducer for pressures $\leq 10\text{bar}$, which is calibrated with an uncertainty within 5mbar :

$$\delta p_{\text{transducer}} = 5 \times 10^{-3} \text{ bar} \quad (3.44)$$

The pressure at the inlet to the evaporator, p_{in} , is computed by subtracting the total pressure drop through the pre-heater, including the contribution relative to the contraction at the test-section inlet, from the measured value of the transducer (which is inserted into the 4mm tube prior to the test-section; see Fig. 19). Figure 33 shows the calculated uncertainty on the inlet pressure to the evaporator in the case of the $510\mu\text{m}$ micro-channel for the three test fluids, when heating the flow in the pre-heater from 25 to 29°C . For mass velocities below $500\text{kg/m}^2\text{s}$ the error is approximately that of the transducer, while for higher flows the uncertainty increases, reaching almost three times the value in Eq. (3.44) at $G = 2500 \text{ kg/m}^2\text{s}$. The highest mass velocities tested never exceed $2500\text{kg/m}^2\text{s}$, and the error on p_{in} is set to $\pm 12\text{mbar}$ (see Fig. 33).

As for the fluid properties, the outlet pressure, p_{out} , is computed from the measured temperature, and its uncertainty is evaluated from the corresponding polynomial, while the uncertainty on the axial coordinate, z , is taken to be equal to that of the channel length, $\delta z = 0.5\text{mm}$.

Figure 34 shows two representative results for the absolute errors on the local pressure for a two phase flow of R-134a. The figure illustrates the effect of mass velocity, heat flux, and location on

the error. The accuracy on the pressure generally reduces when increasing z . However, the locations closest to the inlet exhibit the highest sensitivity to mass velocity and heat flux.

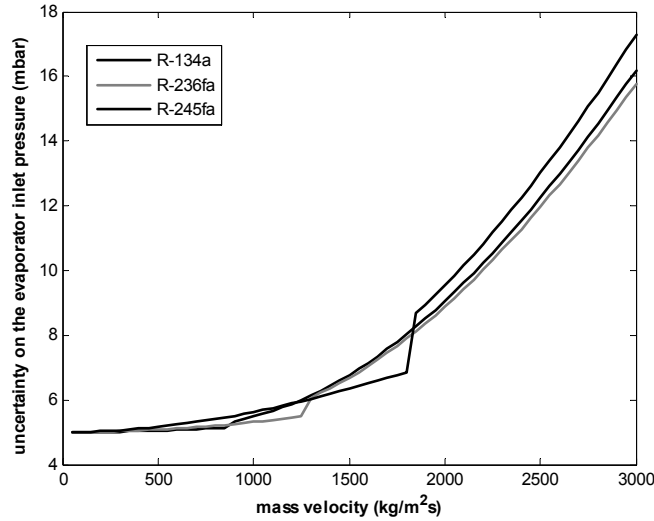


Figure 33. The absolute uncertainty on the pressure at the inlet to the evaporator for a flow in the $510\mu\text{m}$ micro-channel. The step changes in the different curves correspond to laminar-turbulent transitions.

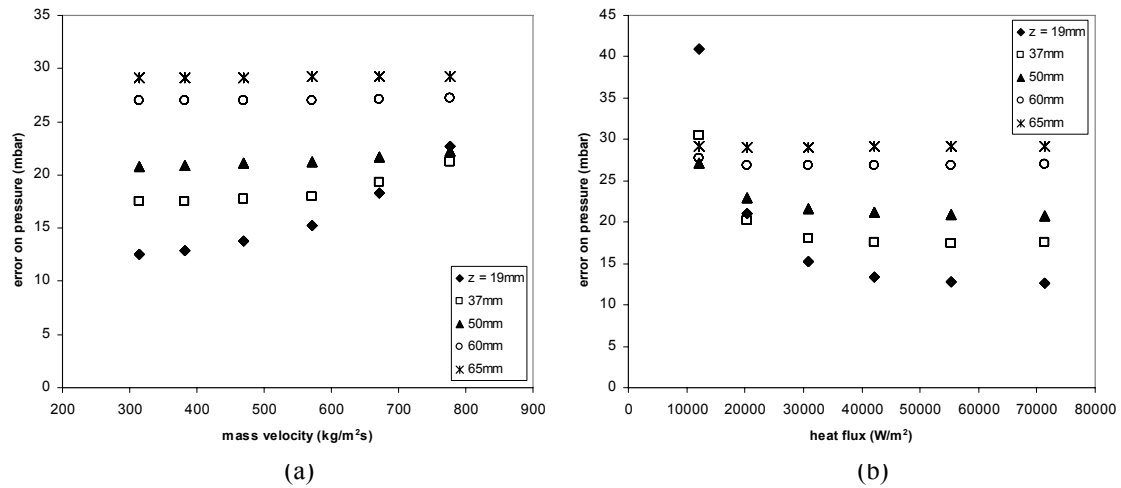


Figure 34. The absolute error on local pressure for flow boiling of R-134a at 31°C in the $510\mu\text{m}$ channel with (a) a heat flux of 72 kW/m^2 , and (b) a mass velocity of $309\text{ kg/m}^2\text{s}$.

Vapor Quality

The vapor quality, as defined in Eq. (3.10), depends on the local enthalpy of the flow, h , as well as on the two physical properties, h_l and h_{lv} , evaluated at the local pressure. The error on the vapor quality is thus

$$\delta x = \sqrt{\left(\frac{\partial x}{\partial h} \delta h\right)^2 + \left(\frac{\partial x}{\partial h_1} \delta h_1\right)^2 + \left(\frac{\partial x}{\partial h_{lv}} \delta h_{lv}\right)^2} \quad (3.45)$$

The uncertainty on the liquid enthalpy and the latent heat are determined from their respective polynomials, i.e.

$$h_1 = g_1 + g_2 p + g_3 p^2 + g_4 p^3 \quad \text{and} \quad \delta h_1 = \frac{dh_1}{dp} \delta p = (g_2 + 2g_3 p + 3g_4 p^2) \delta p \quad (3.46)$$

$$h_{lv} = r_1 + r_2 p + r_3 p^2 + r_4 p^3 \quad \text{and} \quad \delta h_{lv} = \frac{dh_{lv}}{dp} \delta p = (r_2 + 2r_3 p + 3r_4 p^2) \delta p$$

while for the local enthalpy, Eq. (3.11) gives

$$\delta h = \sqrt{\left(\frac{\partial h}{\partial q} \delta q\right)^2 + \left(\frac{\partial h}{\partial G} \delta G\right)^2 + \left(\frac{\partial h}{\partial D} \delta D\right)^2 + \left(\frac{\partial h}{\partial z} \delta z\right)^2 + \left(\frac{\partial h}{\partial h_{in}} \delta h_{in}\right)^2} \quad (3.47)$$

For an initially sub-cooled flow, the inlet enthalpy, h_{in} , is computed from the inlet temperature, T_{in} , as

$$h_{in} = h_r + \int_{T_r}^{T_{in}} c_p dT = a_1 (T_{in} - T_r) + \frac{a_2}{2} (T_{in}^2 - T_r^2) + \frac{a_3}{3} (T_{in}^3 - T_r^3) + \frac{a_4}{4} (T_{in}^4 - T_r^4) \quad (3.48)$$

with the specific heat taken as a third degree polynomial of the temperature (with coefficients a_1 to a_4), and T_r the reference temperature that by definition yields $h_r \equiv 0$. From Eq. (3.48), the error on h_{in} is

$$\delta h_{in} = \frac{dh_{in}}{dT_{in}} \delta T_{in} = (a_1 + a_2 T_{in} + a_3 T_{in}^2 + a_4 T_{in}^3) \delta T_{in} \quad (3.49)$$

Figure 35 presents a set of representative fractional uncertainties, $\delta x/x$. The errors are high at the very low vapor qualities and generally reduce to values less than 10% beyond $x \approx 0.05$.

Heat Transfer Coefficient

The heat transfer coefficient, α , is given as the ratio of the heat flux to the temperature difference between wall and fluid. The fractional error on α is thus

$$\frac{\delta \alpha}{\alpha} = \sqrt{\left(\frac{\delta q}{q}\right)^2 + \left(\frac{\delta(T_w - T_f)}{T_w - T_f}\right)^2} \quad (3.50)$$

The uncertainty on the temperature difference is taken as the sum of the individual uncertainties on wall and fluid temperature. For the wall temperature, Eqs. (3.4) and (3.5) give

$$\delta T_w = \sqrt{\left(\frac{\partial T_w}{\partial T_1} \delta T_1\right)^2 + \left(\frac{\partial T_w}{\partial \eta} \delta \eta\right)^2 + \left(\frac{\partial T_w}{\partial I} \delta I\right)^2 + \left(\frac{\partial T_w}{\partial \Delta V} \delta(\Delta V)\right)^2 + \left(\frac{\partial T_w}{\partial L} \delta L\right)^2 +}$$

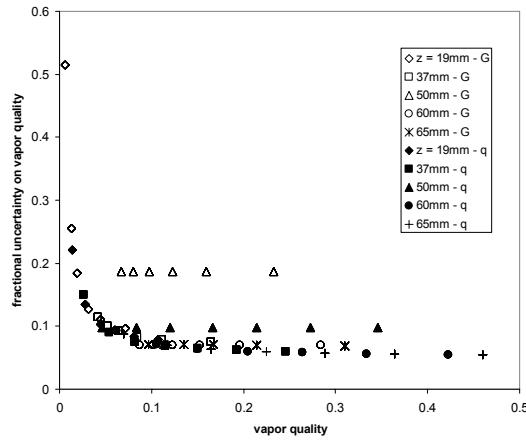


Figure 35. The fractional uncertainty on vapor quality at different locations and for different operating conditions, for flow boiling of R-134a in the 510 μ m channel: white markers – variable mass velocity, black markers – variable heat flux.

$$+ \left(\frac{\partial T_w}{\partial k_w} \delta k_w \right)^2 + \left(\frac{\partial T_w}{\partial R_1} \delta R_1 \right)^2 + \left(\frac{\partial T_w}{\partial R} \delta R \right)^2 \Bigg]^{1/2} \quad (3.51)$$

For axial locations beyond z_{sat} , the flow is assumed to be saturated and the fluid temperature is computed from the local pressure. The error on the temperature is then evaluated from the error on the pressure, as done for other fluid properties (see for example Eq. (3.46)). For the thermal conductivity, k_w , the reported value for stainless steel AISI 304 is of 16.4W/(mK), and the uncertainty is set to $\pm 10\%$. Figure 36 shows the relative uncertainty versus heat flux for different sets of two-phase flow experiments. A summary of the upper and lower limits to the errors on the main parameters that define an individual experiment is given in Table 5.

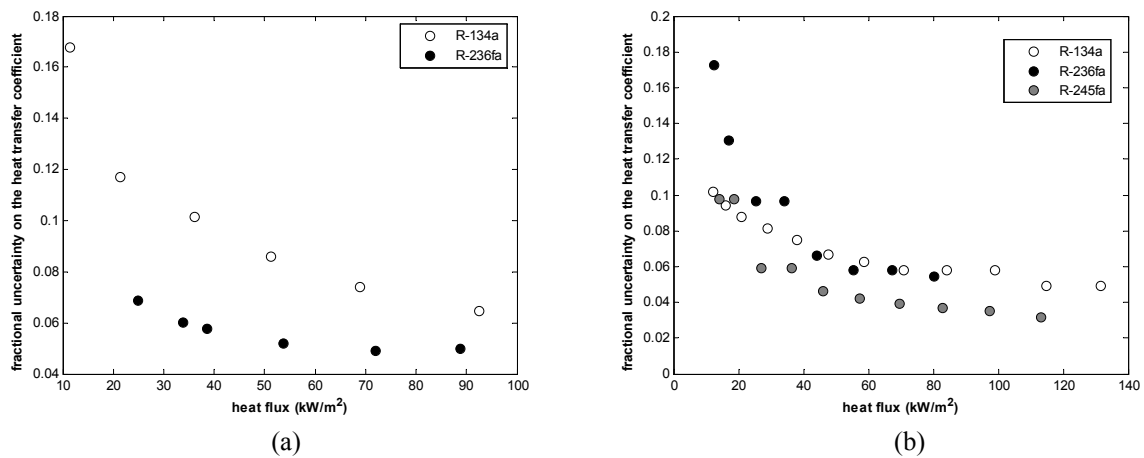


Figure 36. Relative error on the heat transfer coefficient for flow boiling experiments on R-134a, R-236fa, and R-245fa in the 510 and 790 μ m channels, at a nominal mass velocity of 400kg/m²s.

Table 5. Uncertainties on mass velocity, heat flux, and heat transfer coefficients for the three fluids.

	R-134a				R-236fa				R-245fa			
	510 μ m		790 μ m		510 μ m		790 μ m		510 μ m		790 μ m	
	min	max	min	max	min	max	min	max	min	max	min	max
	%		%		%		%		%		%	
	4		3		4		3		4		3	
mass velocity	3	11	2	5	3	4	2	8	4	10	2	5
heat flux												
heat transfer coefficient	6	22	4	24	5	20	4	27	5	20	3	25

Chapter 4

Heat Transfer Results at Stable Test Conditions

The current chapter and Chapter 5 present the heat transfer data collected during the experimental program. Stable flow heat transfer coefficients are presented and discussed in the following sections, while Chapter 5 is dedicated to unstable flow heat transfer. The distinguishing factor between experiments which are deemed as stable from those which are affected by instability, is the degree of fluctuation in the measured parameters. The following stable flow data present quasi-steady outer wall temperatures, whose fluctuations are within the uncertainty band of the individual thermocouples.

4.1 Refrigerant Properties

As was mentioned in Chapter 3, the chosen test fluids are three single-component refrigerants: R-134a, R-236fa, and R-245fa. Figure 37 compares schematically their physical properties at a saturation temperature of 31°C, which corresponds to the value for most of the present experimental runs. The three main properties that distinguish each refrigerant are surface tension, vapor density, and liquid viscosity. The surface tension of R-245fa exceeds the value of R-134a by over 80%. R-245fa also presents a vapor density that is lower than that of R-134a by 60%, while being much more viscous (over +100%). R-236fa positions itself at an intermediate level with respect to the other two fluids. While the combined effect of a low vapor density and a high liquid viscosity will enhance pressure drop, a reduction in ρ_v will increase the degree of expansion associated to phase-change. As for surface tension, the bubble departure diameter (d_d), taken to be proportional to the capillary length scale, i.e. $d_d \propto [\sigma/(\rho_l g)]^{1/2}$ for $\rho_v \ll \rho_l$, is expected to increase with σ , and may lead to a reduction in departure frequency for the high surface tension fluid.

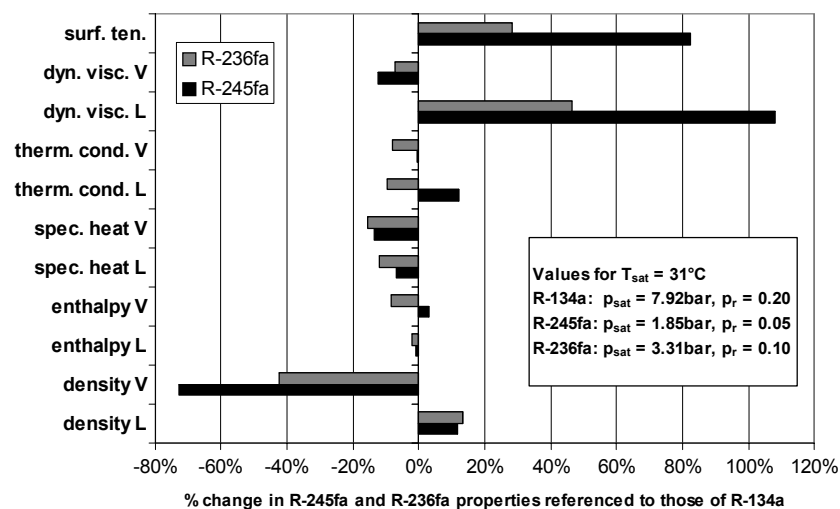


Figure 37. Schematic comparison of the physical properties of the three refrigerants tested at 31°C.

4.2 Flow Boiling Curves

Figures 38 illustrates two typical flow boiling curves for refrigerants R-134a and R-245fa in the 510 μ m channel. The data refer to the last temperature measurement location, 65mm downstream of the entrance to the evaporator, and are obtained by varying the intensity of the supplied current, or, in other terms, the heat flux. In both cases the wall superheat, defined as the difference between the inner wall temperature and the saturation temperature at the local pressure, is shown to experience a substantial excursion before reaching boiling onset when increasing the heat flux, with values as high as 30-35 $^{\circ}$ C for R-245fa and R-236fa. The boiling branches of the curves present no hysteresis, with the data for ascending and descending heat fluxes substantially in agreement with one another.

Some visualizations taken at the exit to the evaporator, assumed to be consistent with the flow patterns occurring at the last measurement site, are illustrated to the left of each boiling curve. While

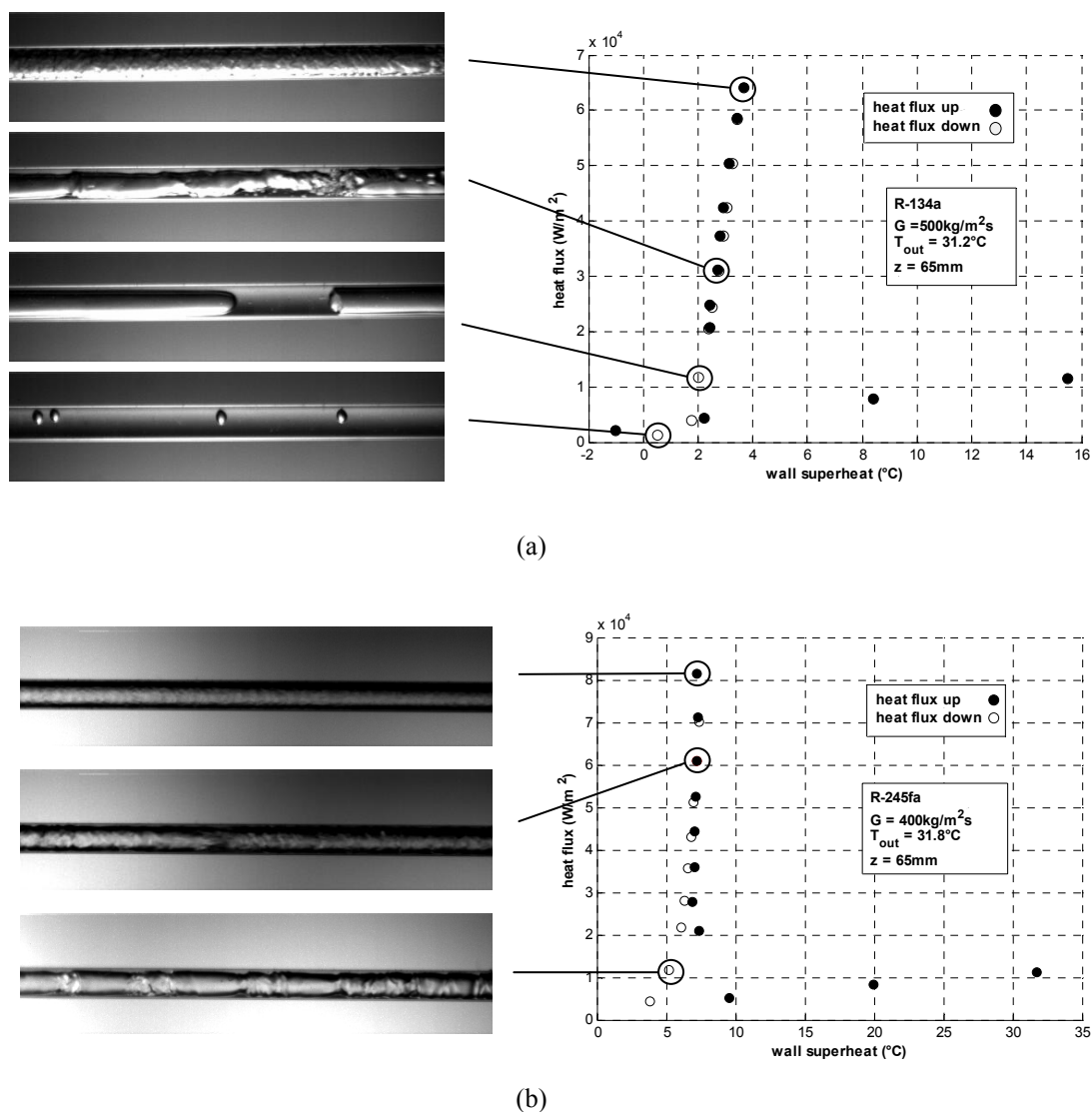


Figure 38. Flow boiling curves and flow patterns for (a) R-134a and (b) R-245fa, in the 510 μ m channel, relative to the last temperature acquisition location.

R-134a presents the four typical flow patterns as described in Chapter 2, the bubbly and slug flow patterns for R-245fa are less evident since at even very low heat fluxes the exiting flow is seen to have churn flow characteristics.

4.3 Micro-Channel Two-Phase Heat Transfer Data

While the measured heat transfer coefficients present some analogies between R-134a and R-236fa, the lowest pressure fluid R-245fa distinguishes itself in both its trends and order of magnitude.

Two-Phase Heat Transfer for R-134a

Figure 39 depicts R-134a flow boiling heat transfer coefficients for four different mass velocities at heat fluxes ranging from 12 to 200kW/m². The applied heat flux is limited by the critical heat flux (which was avoided here), which depends on the flow rate. The data, plotted on the α -x plane, show heat transfer coefficients that present relatively little change with vapor quality and that increase with heat flux. The value for α is shown to be as high as 35kW/(m²K) at a heat flux of 200kW/m². The effect of mass velocity is better seen in Fig. 40, where the heat transfer coefficients are plotted for two heat fluxes and mass velocities between 250 and 800kg/(m²s). Other than for a

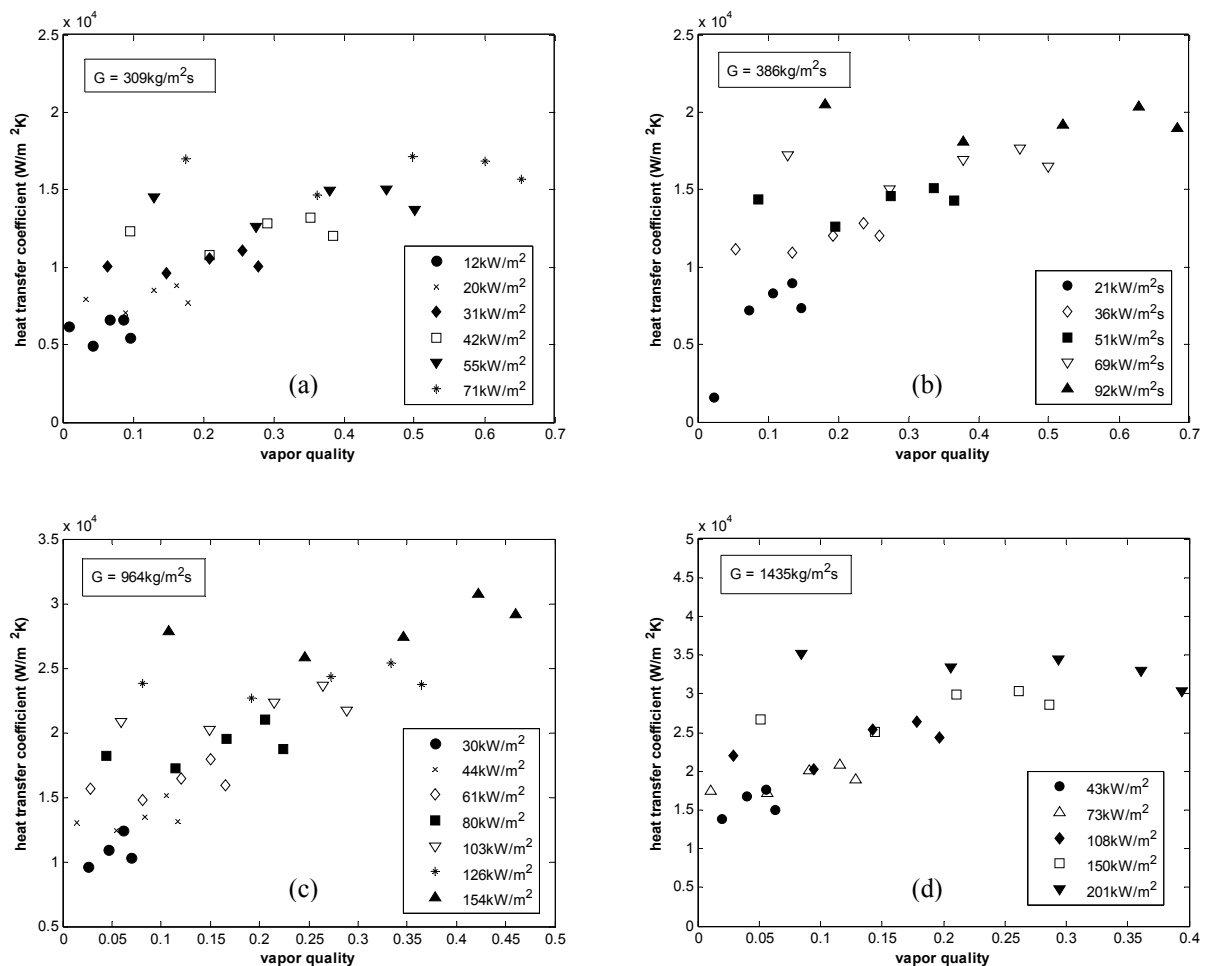


Figure 39. Experimental heat transfer coefficients versus vapor quality for saturated flow boiling of R-134a in the 510 μ m micro-channel for (a) 309, (b) 386, (c) 964, and (d) 1435kg/m²s. The flow enters the channel as a sub-cooled liquid at 29°C, and exits as a saturated two-phase fluid at 31°C.

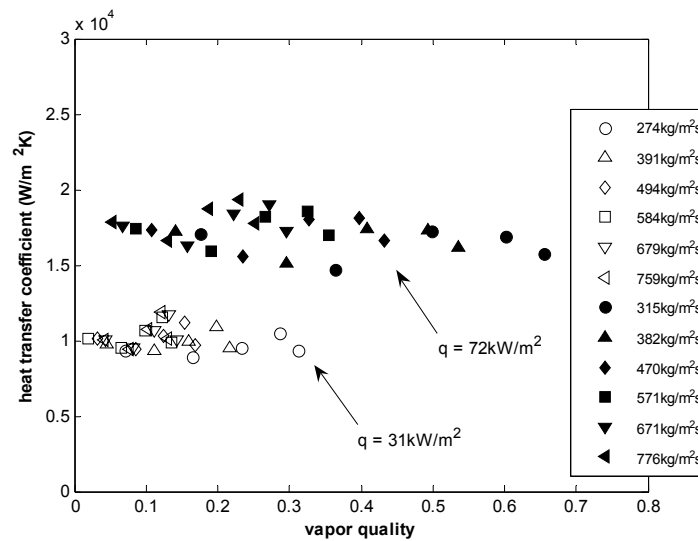


Figure 40. Experimental heat transfer coefficients for R-134a in the 510 μ m channel, over a range of mass velocities at two heat fluxes. The flow enters the channel as a sub-cooled liquid at 29°C, and exits as a saturated two-phase fluid at 31°C.

certain degree of experimental scatter, the data points at a fixed heat flux overlap, indicating a minimal effect of mass velocity.

Figure 41 illustrates the effect of inlet sub-cooling and saturation temperature on the two-phase heat transfer coefficients. The coefficients are unaltered by changes in the temperature of the sub-cooled liquid entering the evaporator (Fig. 41a), while the values of α generally benefit from higher saturation temperatures/pressures over a wide range of heat fluxes (Fig. 41b).

The observations on the heat transfer data for the 500 μ m tube are generally confirmed when testing the larger size channel ($D = 790\mu$ m). Figure 42a illustrates heat transfer coefficients for a high mass velocity test, where the main difference with respect to the smaller channel is in the downward trends towards the channel exit. When comparing the average heat transfer coefficients, reducing the tube size is seen to enhance heat transfer (as in Fig. 42b).

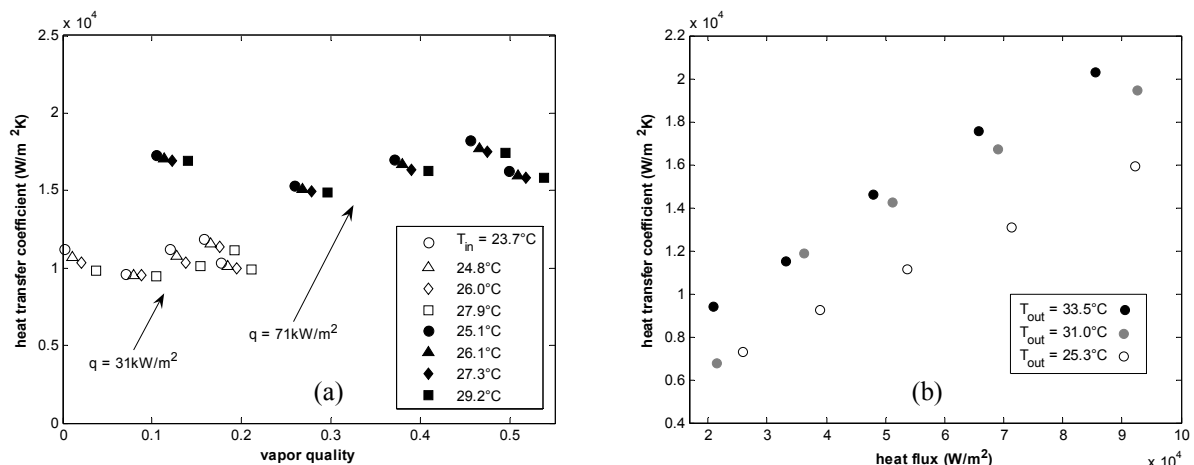


Figure 41. (a) Experimental heat transfer coefficients for R-134a at 31°C and different inlet temperatures, and (b) average heat transfer coefficients versus heat flux for three different outlet fluid temperatures. The results refer to the 510 μ m channel at a nominal mass velocity of 400 kg/m²s.

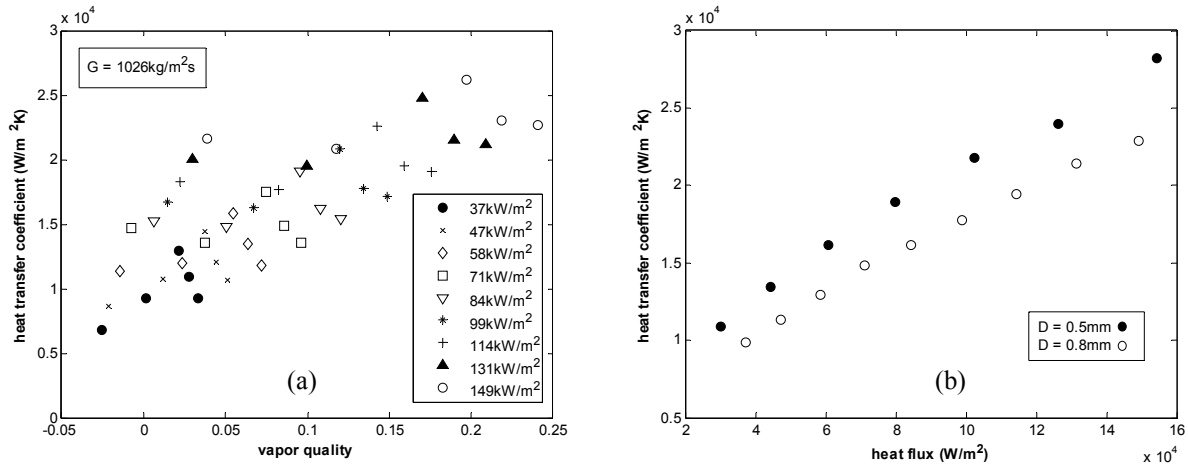


Figure 42. (a) Experimental heat transfer coefficients versus vapor quality in the 790 μm channel, and (b) average heat transfer coefficients versus heat flux for the two tube sizes. The data refer to flow boiling of R-134a with $T_{\text{out}} = 31^\circ\text{C}$ and a nominal mass velocity of 1000 $\text{kg/m}^2\text{s}$.

Shiferaw and coworkers [45] performed experiments with R-134a in 2.01mm and 4.26mm circular channels, under similar conditions to some of the data sets presented above. Figure 43 illustrates the direct comparison between the current study and Shiferaw *et al.* for a mass velocity of 300 $\text{kg/m}^2\text{s}$. Shiferaw's data for the 2.01mm tube agree in order of magnitude with the present values for the 510 μm channel at corresponding levels of heat flux, and any discrepancy may be associated to the difference in tube size. The tube diameter effect seems to be more manifest at the lower heat fluxes, disappearing at the higher values. A similar conclusion may be drawn from Fig. 43b, which compares equivalent data from Shiferaw's 4.26mm channel with current data for the 790 μm tube, although in this case the effect of channel diameter is less clear.

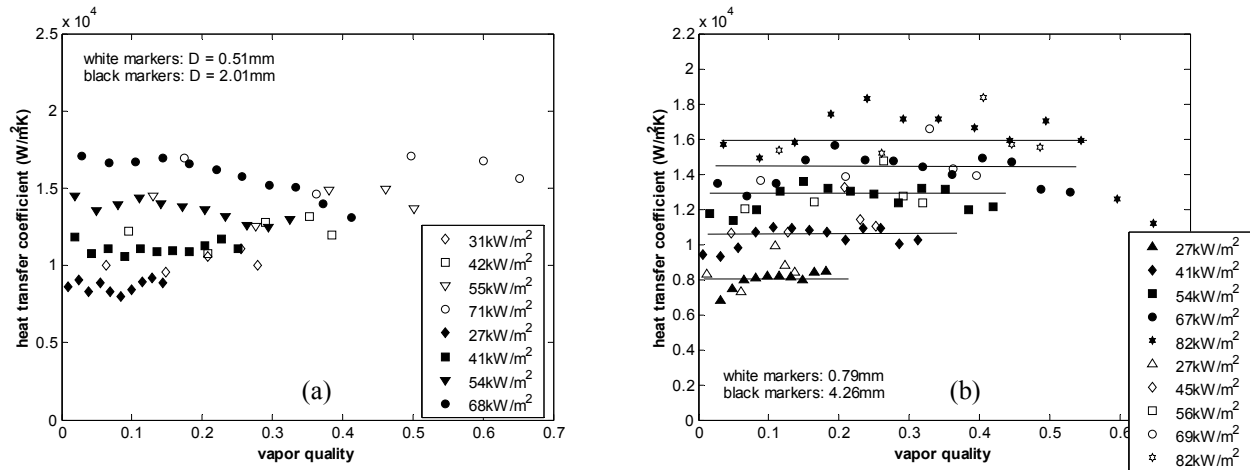


Figure 43. Comparison with present data to those of Shiferaw *et al.* [45] for R-134a. Black markers refer to the data from [45] ($G = 300 \text{ kg/m}^2\text{s}$ and 8bar), while white markers refer to the current database ($G = 309 \text{ kg/m}^2\text{s}$ and $p_{\text{out}} = 7.92 \text{ bar}$).

Two-Phase Heat Transfer for R-236fa

The results for R-236fa present many similarities to those for R-134a. As shown in Figs. 44 and 45, the heat transfer coefficients are extremely sensitive to heat flux, and reveal a limited influence of mass velocity and vapor quality. As for R-134a, the data for R-236fa show an improvement in heat transfer with saturation temperature (Fig. 45b), while no substantial change is observed when varying the degree of inlet sub-cooling. Tests for the larger channel yield similar trends in the α -x plane, although the average values of the heat transfer coefficients are again lower than the ones in the 510 μ m case (see Fig. 46). Here, however the effect of tube diameter increases with heat flux as shown in Fig. 46b.

Under the present test conditions, R-236fa distinguishes itself from R-134a mainly in the

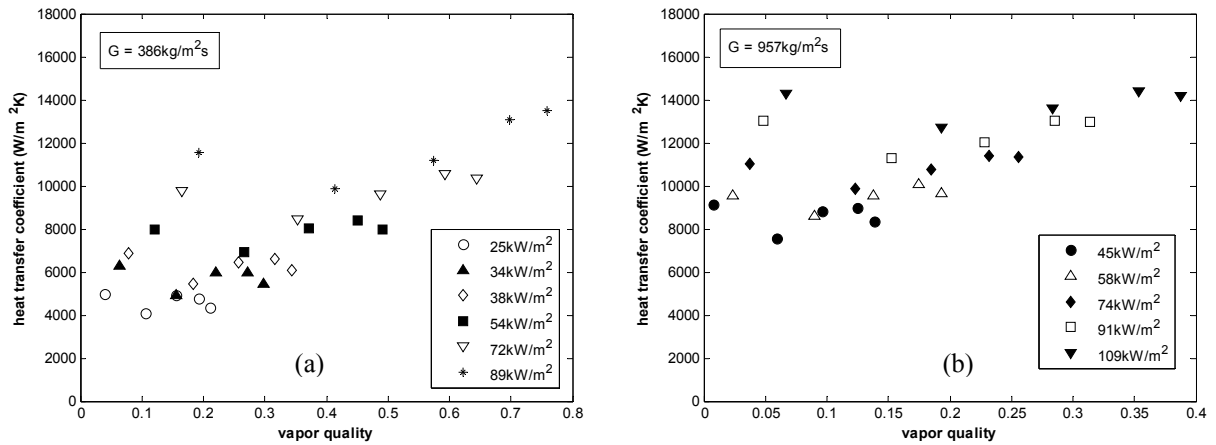


Figure 44. Experimental heat transfer coefficients versus vapor quality for flow boiling of R-236fa in the 510 μ m tube for (a) 386 and (b) 957 kg/m²s. The flow enters the channel as a sub-cooled liquid at 29°C, and exits as a saturated two-phase fluid at 31°C.

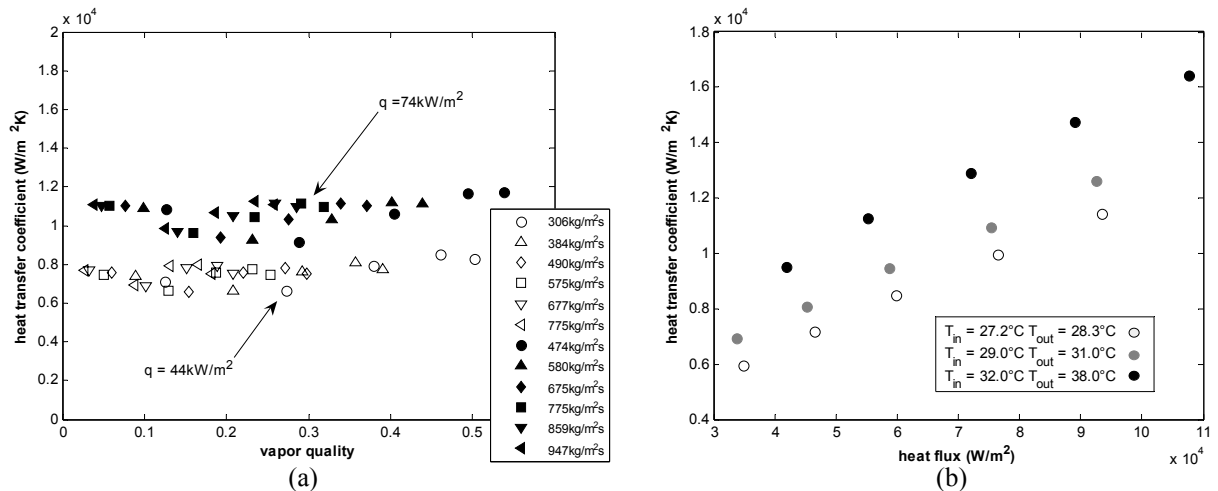


Figure 45. Experimental heat transfer coefficients for flow boiling of R-236fa in the 510 μ m channel for (a) different mass velocities with $T_{in} = 29^\circ\text{C}$ and $T_{out} = 31^\circ\text{C}$, and (b) different saturation conditions and a nominal mass velocity of 700 kg/m²s.

magnitude of the heat transfer coefficients. Figure 47 compares two sets of data, one for R-236fa while the other for R-134a, at similar test conditions. The values of α for R-134a are generally about twice those of R-236fa.

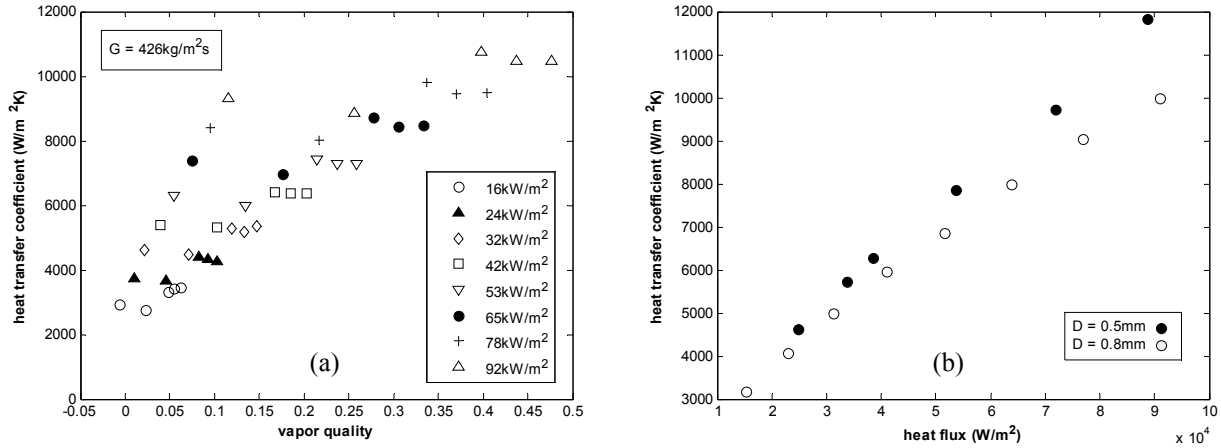


Figure 46. (a) Experimental heat transfer coefficients of R-236fa versus vapor quality in the 790μm channel, and (b) average heat transfer coefficients versus heat flux for the two tube sizes. The data refer to flow boiling with $T_{\text{out}} = 31^\circ\text{C}$ and a nominal mass velocity of $400 \text{ kg/m}^2\text{s}$.

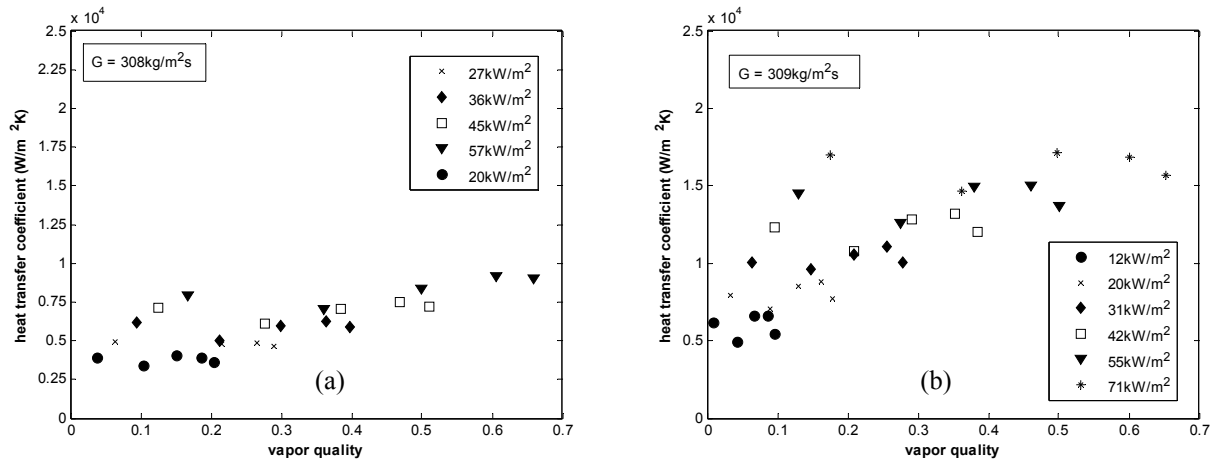


Figure 47. Figure comparing the heat transfer results for (a) R-236fa and (b) R-134a in the 510μm channel with $T_{\text{in}} = 29^\circ\text{C}$ and $T_{\text{out}} = 31^\circ\text{C}$.

Two-Phase Heat Transfer for R-245fa

The trends in the data for R-245fa present distinctive characteristics with respect to those seen for the previous two fluids. Figure 48 shows a plot for a representative set of heat transfer coefficients in the α - x plane. Unlike the results for R-134a and R-236fa, heat transfer for R-245fa appears to be sensitive to heat flux only up to intermediate vapor qualities, beyond which the data points for different values of q merge, and exhibit a monotonic increase with vapor quality. The heat transfer coefficients corresponding to the highest heat flux (110 kW/m^2) in Fig. 48 are affected by irregular

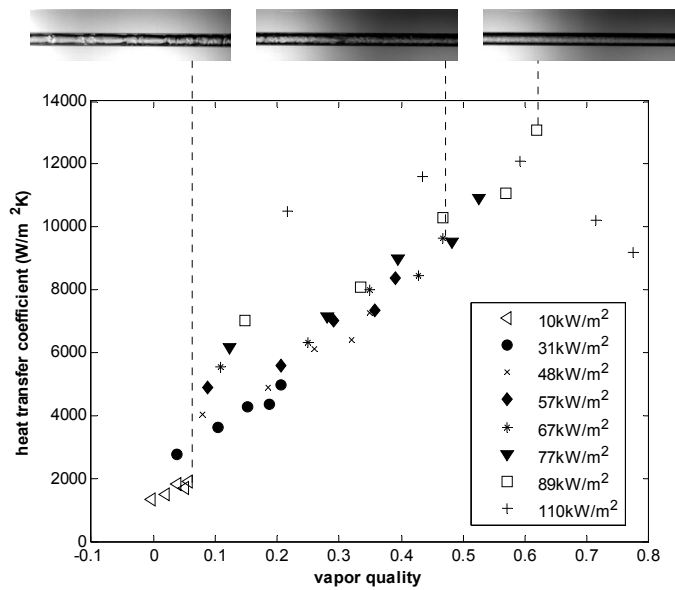


Figure 48. Experimental heat transfer coefficients for R-245fa and local flow patterns, plotted versus vapor quality for flow boiling (510 μ m channel) at a mass velocity of 400kg/m²s, with an inlet temperature of 30°C and exiting at 32°C.

spikes in the wall temperatures, as to indicate an approach to the critical heat flux condition. Figure 49 illustrates two other sets of heat transfer data for mass velocities of 300 and 800kg/m²s. Figure 49a shows similar results to the ones in Fig. 48, with the only difference in the trend of data for $q'' = 53$ kW/m², which was subjected to an oscillatory instability. The heat transfer coefficients in Fig. 49b cover a more limited range of vapor qualities, and show the dependency on heat flux at the medium-low values of x . As for R-134a and R-236fa, these heat transfer characteristics are found also for the larger tube, although in this case the coefficients drop with vapor quality in the heat flux dependent region (low x), and, as for the smaller channel, merge as the vaporization progresses (see Fig. 50).

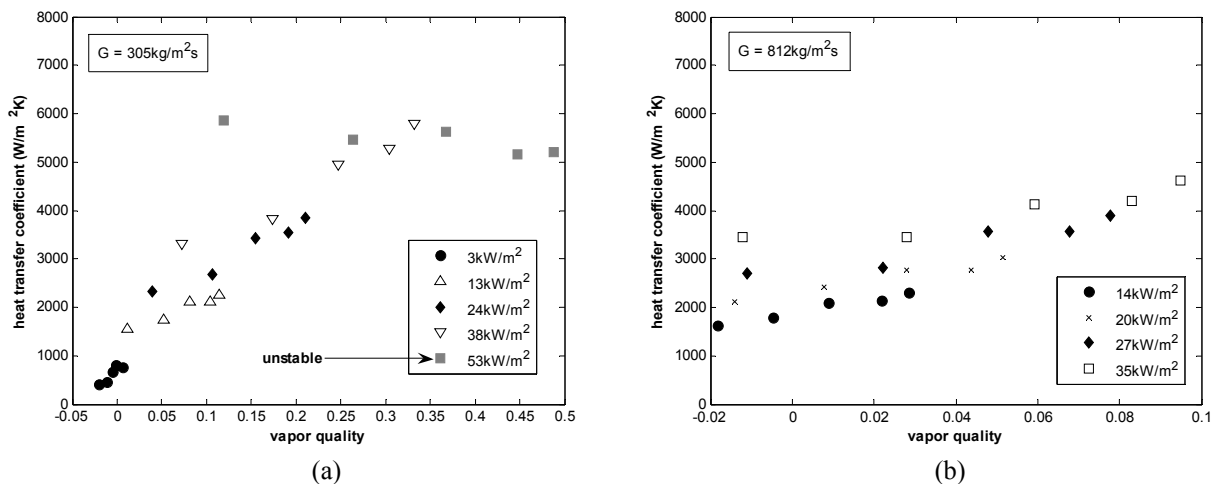


Figure 49. Experimental heat transfer coefficients versus vapor quality for flow boiling of R-245fa in the 510 μ m tube for (a) 305 and (b) 812kg/m²s. The flow enters the channel as a sub-cooled liquid at 30°C, and exits as a saturated two-phase fluid at 32°C.

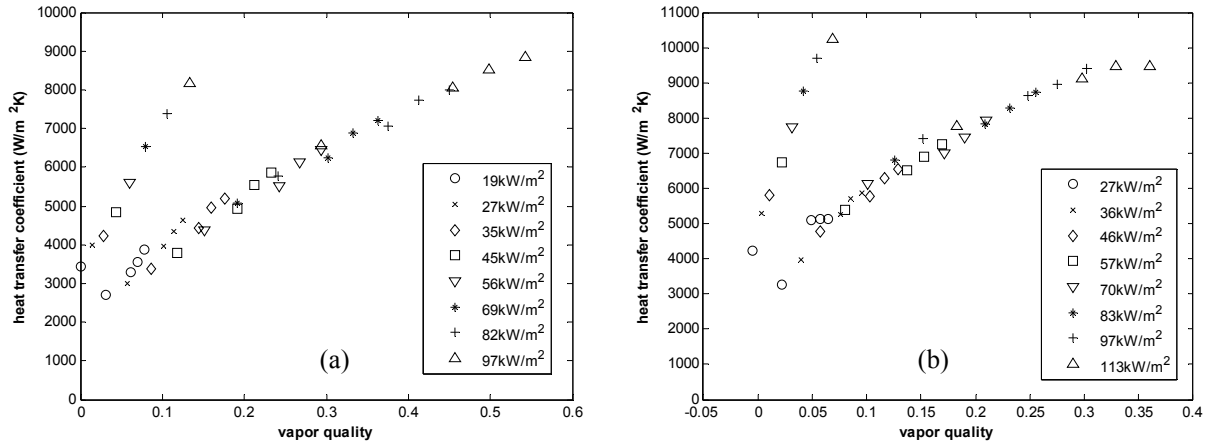


Figure 50. Experimental heat transfer coefficients versus vapor quality for flow boiling of R-245fa in the 790 μ m tube for (a) 300 and (b) 500 kg/m²s. The flow enters the channel as a sub-cooled liquid at 27°C, and exits as a saturated two-phase fluid at 31°C.

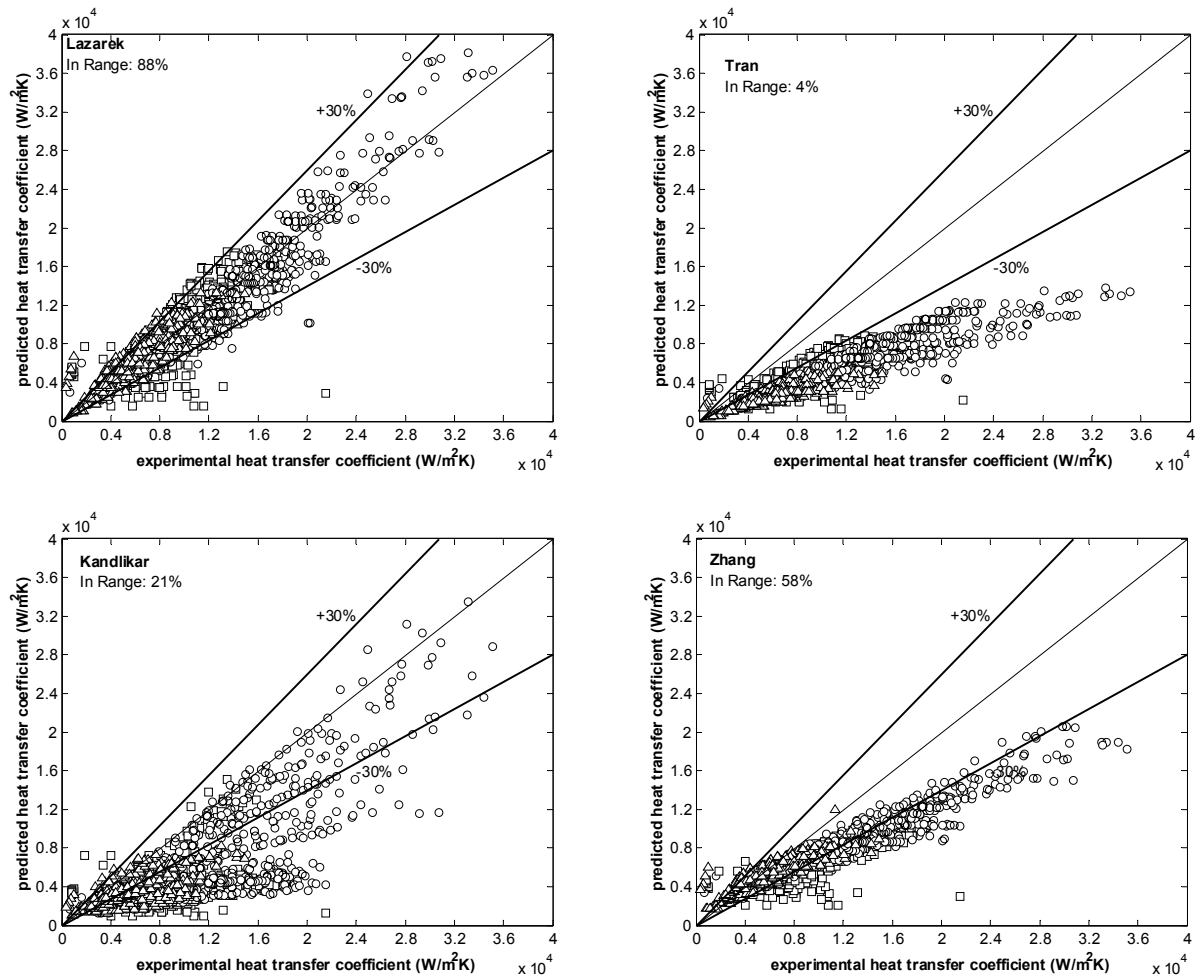


Figure 51. Predicted versus experimental heat transfer coefficients. The predicted values refer to the methods by Lazarek and Black [5], Tran *et al.* [25], Kandlikar and Balasubramanian [41], and Zhang *et al.* [42]. O - R-134a, □ - R-236fa, Δ - R-245fa.

4.4 Heat Transfer Predictions to the Experimental Data

Figures 51 and 52 present the overall comparison of the methods described in Chapter 2 with the current database. Figure 51 refers to the methods of Lazarek and Black [5], Tran *et al.* [25], Kandlikar and Balasubramanian [41], and Zhang *et al.* [42]. Lazarek and Black's correlation gives the highest success rate, with 88% of the data predicted within $\pm 30\%$ (relative to the experimental values), while the one by Tran and coworkers [25] performs the worst, with only 4% within the same error band. Although the correlation by Zhang and coworkers predicts only 58% of the data in the $\pm 30\%$ range, with a general tendency to under-predict the experimental coefficients, it is also the method with the lowest degree of dispersion. Figure 52 refers to the three-zone evaporation model of Thome and coworkers [12]. The first figure (Fig. 52a) is a comparison of the model with the entire database, while the second (Fig. 52b) considers only those data points for which the corresponding flow is in either isolated bubble (ib) mode or coalescing bubble (cb) mode (see Fig. 6 in Chapter 2), as the model is for the elongated bubble (slug) flow regime. The local flow patterns were determined using the correlations taken from [19],

$$0 < x < x_{ib/cb} \quad \text{with} \quad x_{ib/cb} = 0.763 \left(\frac{q \rho_v \sigma}{\mu_l h_{lv} G^2} \right)^{0.41} \quad (4.1)$$

for an isolated bubble flow, and

$$x_{ib/cb} \leq x < x_{cb/a} \quad \text{with} \quad x_{cb/a} = 0.00014 \left(\frac{GD}{\mu_l} \right)^{1.47} \left(\frac{G^2 D}{\rho_l \sigma} \right)^{-1.23} \quad (4.2)$$

for a coalescing bubble flow (with $x_{cb/a}$ the coalescing bubble-annular transition quality). As shown in Fig. 52, the 59% success rate increases to 77% when the data is segregated according to flow pattern, which is consistent with the fact that the model was developed for pure slug flow (the data in Fig. 52b correspond to both bubbly and elongated bubble flow).

Figure 53 shows different sets of data plotted versus the corresponding predictions of the methods described in Chapter 2, with the exception of the correlation of Tran *et al.* that gives very poor agreement with the experimental heat transfer coefficients. Lazarek and Black's correlation predicts the order of magnitude of the heat transfer data with some success, and is consistent in trend with the data for R-134a and R-236fa that show little change with vapor quality. Clearly problems

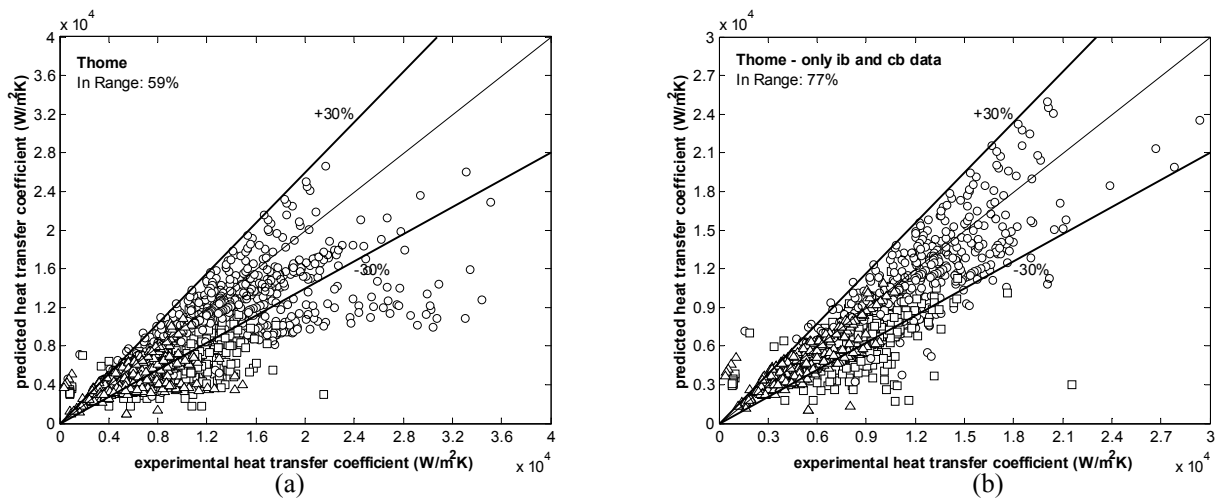


Figure 52. Three-zone model [12] predictions versus the experimental heat transfer coefficients for (a) the entire database, and (b) only data for isolated bubble and coalescing bubble flows. O - R-134a, □ - R-236fa, Δ - R-245fa.

start occurring once the data shows dependency on vapor quality, as in the case of R-245fa, and the general applicability of the correlation becomes questionable. For R-245fa the heat flux independent behavior described in the previous section develops primarily in the annular flow region, and is not captured by any of the methods.

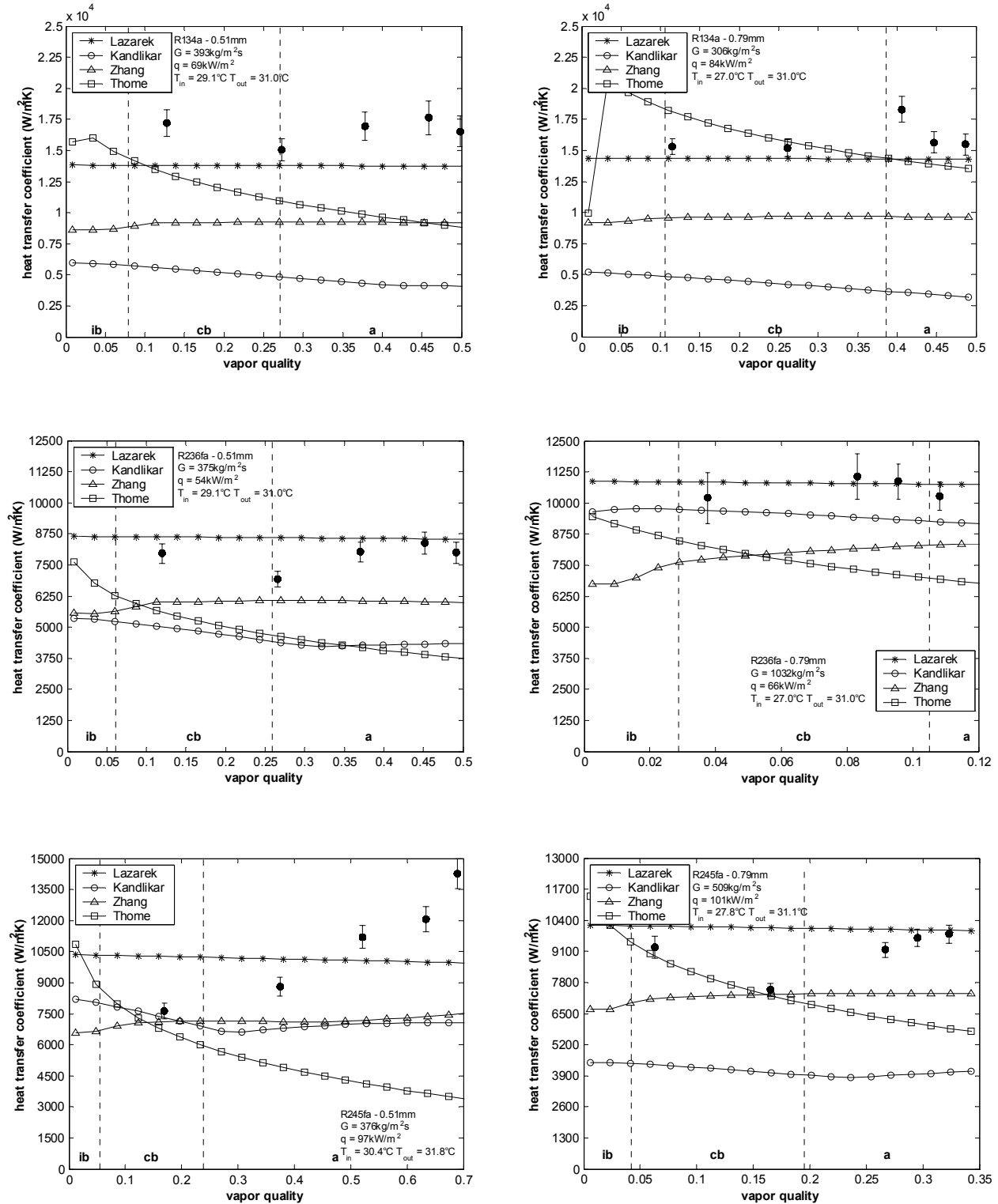


Figure 53. Comparison of individual data sets with the predictions of the methods described in Chapter 2. The plots illustrate the local flow patterns, as classified in [19] (ib – isolated bubble, cb – coalescing bubble, a – annular).

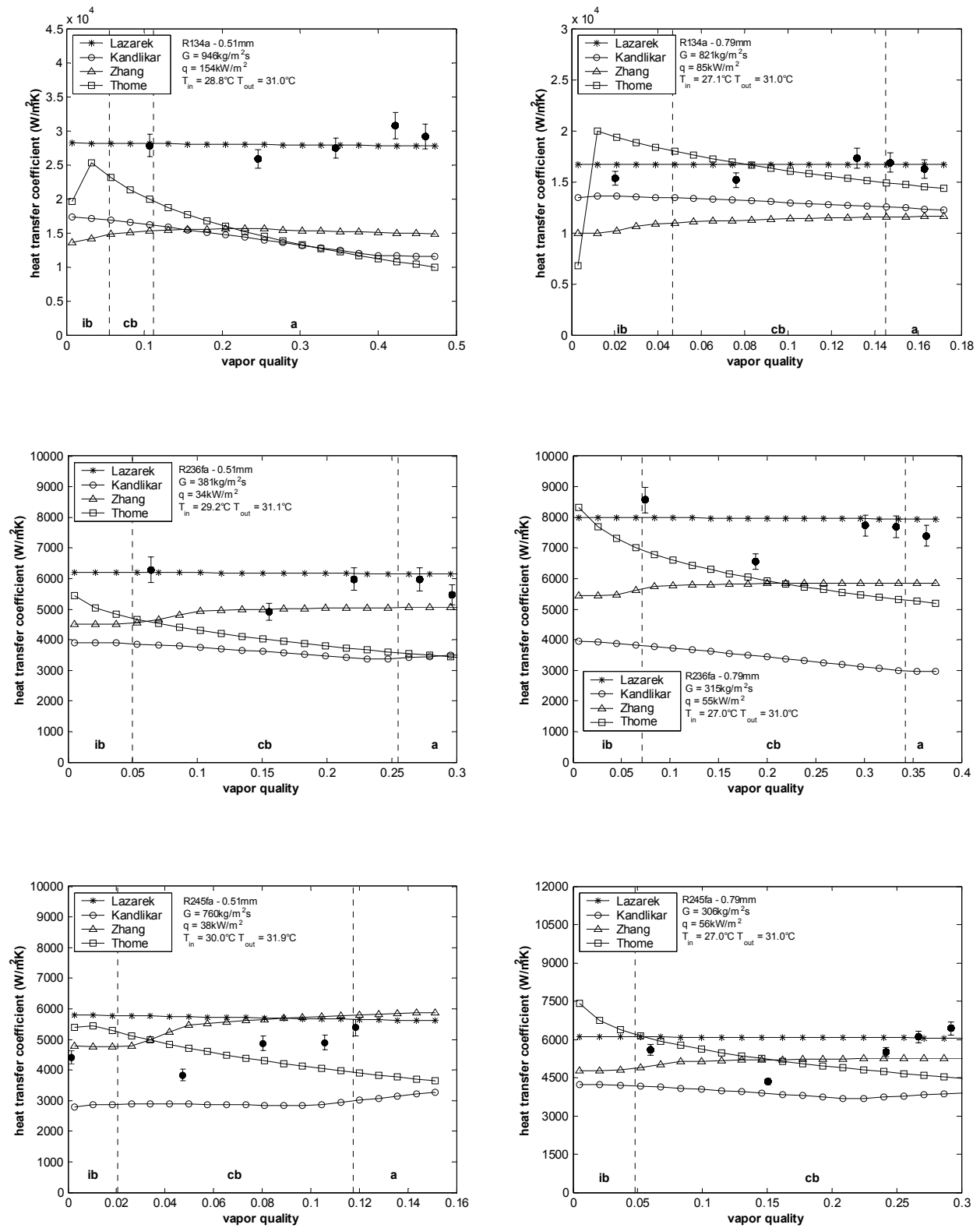


Figure 53. continued

4.5 Summary

The experiments on stable two-phase micro-channel flows for the three fluids tested have given clear indications as to the different parameters that govern the heat transfer process. While for R-134a and R-236fa the heat transfer coefficients have been shown to be strongly dependent on heat flux and fluid properties even up to high vapor qualities, when annular flow is the dominant flow mode, R-245fa has distinguished itself exhibiting two different heat transfer zones. At low vapor qualities, the heat transfer coefficients for R-245fa are heat flux dependent as in the case of the other two fluids. However, at high degrees of vaporization the heat flux dependence disappears, and the curves on the α -x plane increase monotonically with vapor quality. Among the methods for micro-channel heat transfer considered, the Lazarek-Black correlation [5] gives the best performance, predicting 88% of the database with $\pm 30\%$.

Chapter 5

Heat Transfer with Flow Instabilities

As discussed in Chapter 2, micro-channel evaporators are often affected by oscillatory instabilities. The following sections present data for unstable two-phase flows, providing details of the unstable characteristics in terms of wall and fluid temperatures, and highlighting the possible errors that may occur in the estimation of local heat transfer coefficients when their presence is neglected.

5.1 Temperature Fluctuations Associated to Compressible Volume Instabilities

Figure 54a illustrates a representative “stable” temporal profile for the outer wall temperature, with the fluctuations generally within the uncertainty band of the thermocouples. Stability is guaranteed by the presence of the valve at the entrance to the test-section (see Figs. 21 and 55), which “isolates” the boiling flow in the evaporator from any upstream compressibility (i.e., a body of gas present in the line, a flexible element at the tubing connections, or the compressibility of the liquid itself, as suggested in [14]). As the valve is opened, while maintaining fixed operating conditions by adjusting the pressures in the two vessels, the resistance to any backflow is reduced. If the conditions are such that the pressure pulse from the bubble formation process is strong enough, an oscillatory instability will propagate, with liquid being cyclically expelled into the compressible volume. In Fig. 54b for an unstable flow, the temperature fluctuation with respect to the mean is about $\pm 2.0^\circ\text{C}$, much lower than the $\pm 0.15^\circ\text{C}$ of the stable flow. Furthermore, the temperature cycle is quite repeatable in both shape and magnitude, with a frequency of about 4Hz. This type of fluctuation and frequency were also obtained using an IR camera to measure the outer wall temperature.

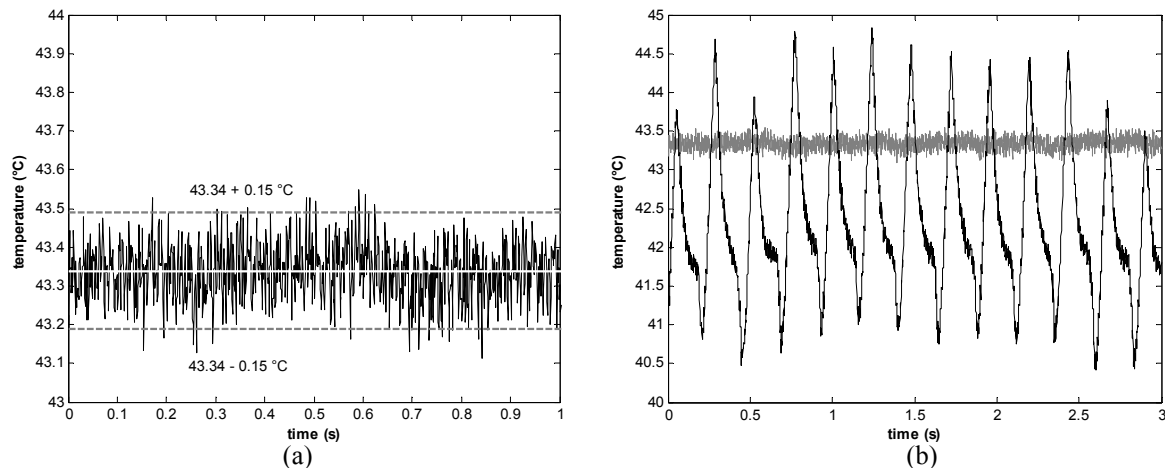


Figure 54. (a) Steady outer wall temperature during flow boiling, and (b) wall temperature during flow instability (black curve) as compared to the steady profile (shown in gray). Values refer to R-245fa in the 510 μm tube, a heat flux of 50kW/m², and mass velocities of 500kg/m²s (steady case) and 400kg/m²s (unstable case). The signal sampling rate is of 1000samples/s over 3s.

A significant fluctuation in the boiling process brings about some differences in the analysis with respect to that presented in Section 2.4 and in the Appendix, which will be addressed at the end of this section. However, the conclusions from that approach maintain their validity. In particular, a

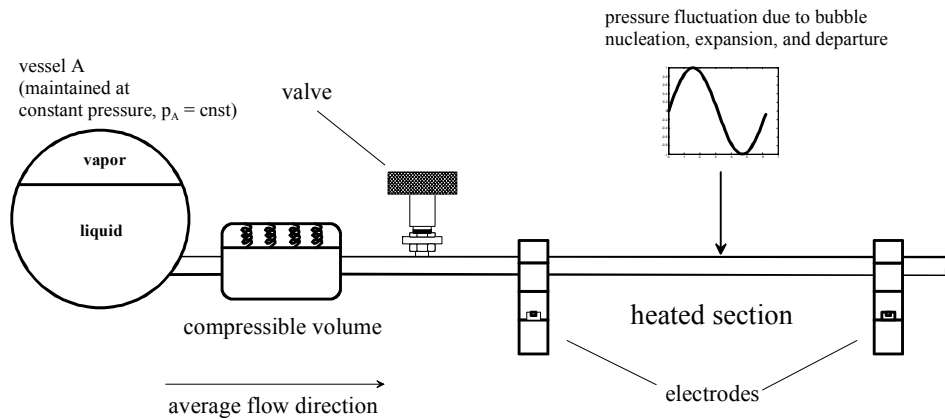


Figure 55. Schematic showing the test-section, the valve, and the upstream compressible volume, as would occur in the present test facility.

lower flow rate shifts the operating point towards the critical condition. A lower flow rate will also decrease the inertia of the heated section (by increasing the exit vapor quality), and will lead to a further reduction in the gap between the critical and operating points (see Fig. 13). In addition, a higher heat flux will displace the whole internal characteristic upward, setting the critical flow rate at a higher value.

Once the flow becomes unstable, the outer wall temperature profiles change dramatically, as was shown in Fig. 54b. The temperatures start oscillating very regularly, with amplitudes that increase with heat flux. Figure 56 illustrates the progressive rise in the intensity of the oscillation with heat flux, for an unstable flow of R-236fa. Higher heating also changes the shape of the curves. Figure 57 shows a set of results for R-245fa. The low heat flux case presents two main oscillation modes at 4.4 and 7.3Hz. As the heat flux is increased, the second mode dampens, and eventually disappears entirely at 87 kW/m^2 . Recalling the description given in Section 2.4 and Fig. 14, the underlying reasons for the periodic temperatures are (1) the local change in flow temperature associated to the pressure fluctuations due to the bubble growth, expansion, and flushing process, and (2) the cyclical variations in the heat transfer mechanisms.

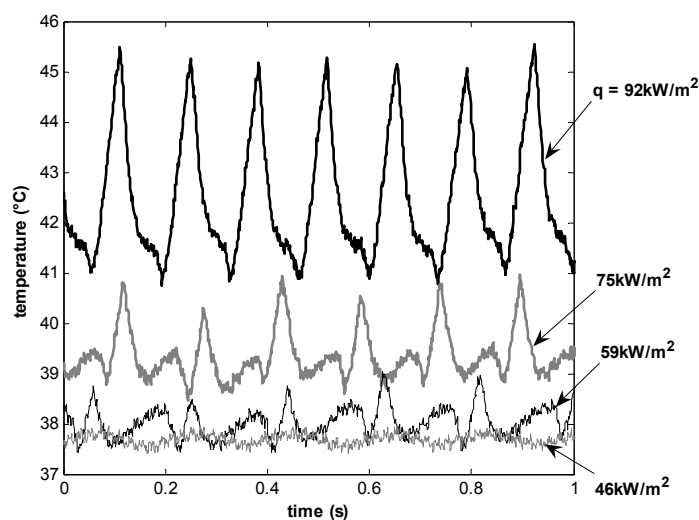


Figure 56. Wall temperature fluctuations taken 65mm downstream of the entrance to the evaporator, for an R-236fa flowing with a mass velocity of $700\text{ kg/m}^2\text{s}$.

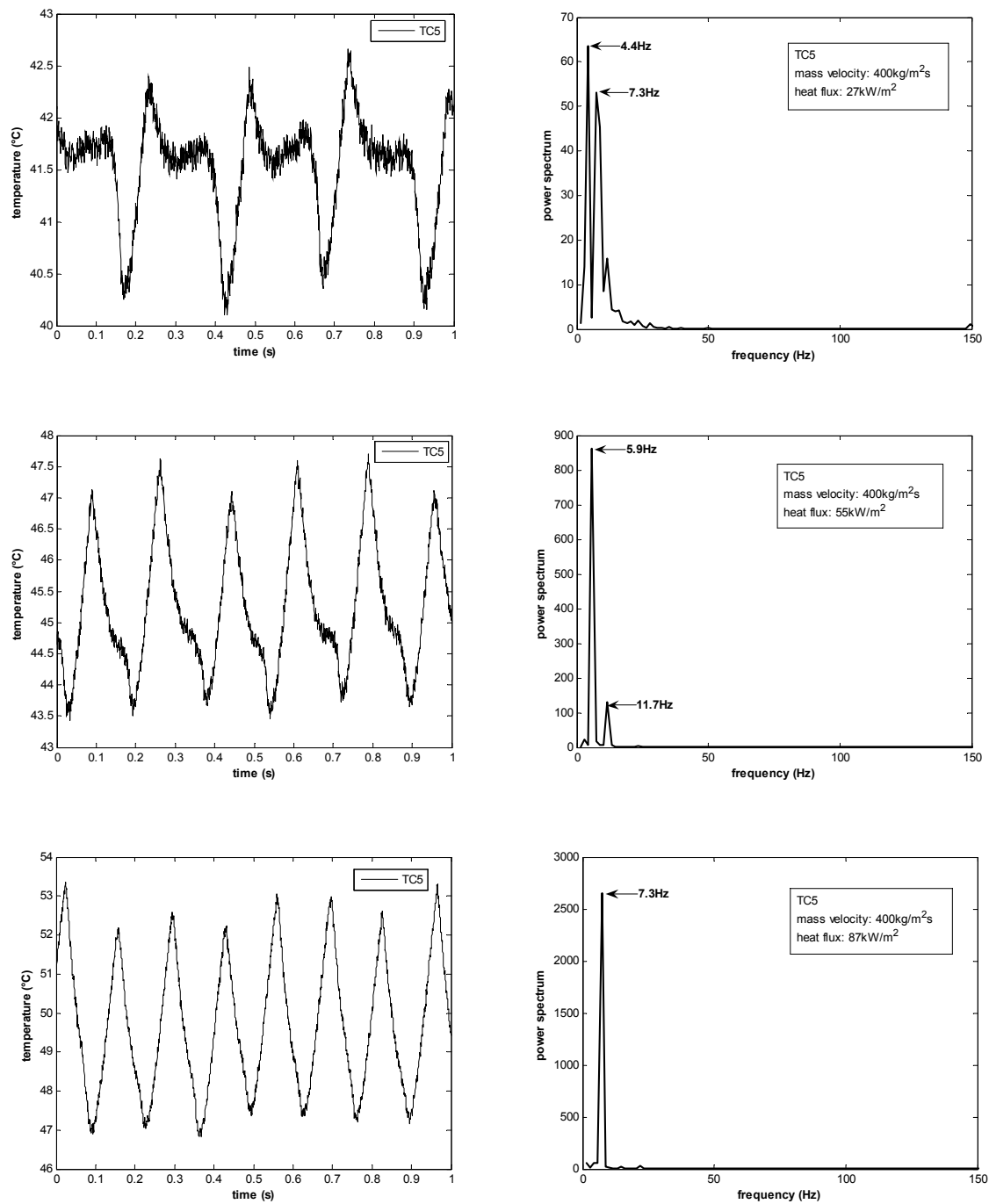


Figure 57. Wall temperature fluctuations and corresponding power spectrums for unstable flow boiling of R-245fa at different heat fluxes (510 μm tube). The temperatures refer to the last thermocouple on the heated length.

Figure 58 shows the oscillations in the temperature of the fluid exiting the evaporator, at different levels of heat flux. The temperature at the lowest heat flux presents one main mode at 4.4Hz, which is also found in the wall temperature. However, there is no presence of the second mode at 7.3Hz, which may indicate that although the change in fluid temperature contributes to the behavior of the wall temperature, the fluctuations in the local heat transfer coefficient, from pure convection of liquid, to nucleate boiling, to convective vaporization with thin film evaporation (see Fig. 14), also

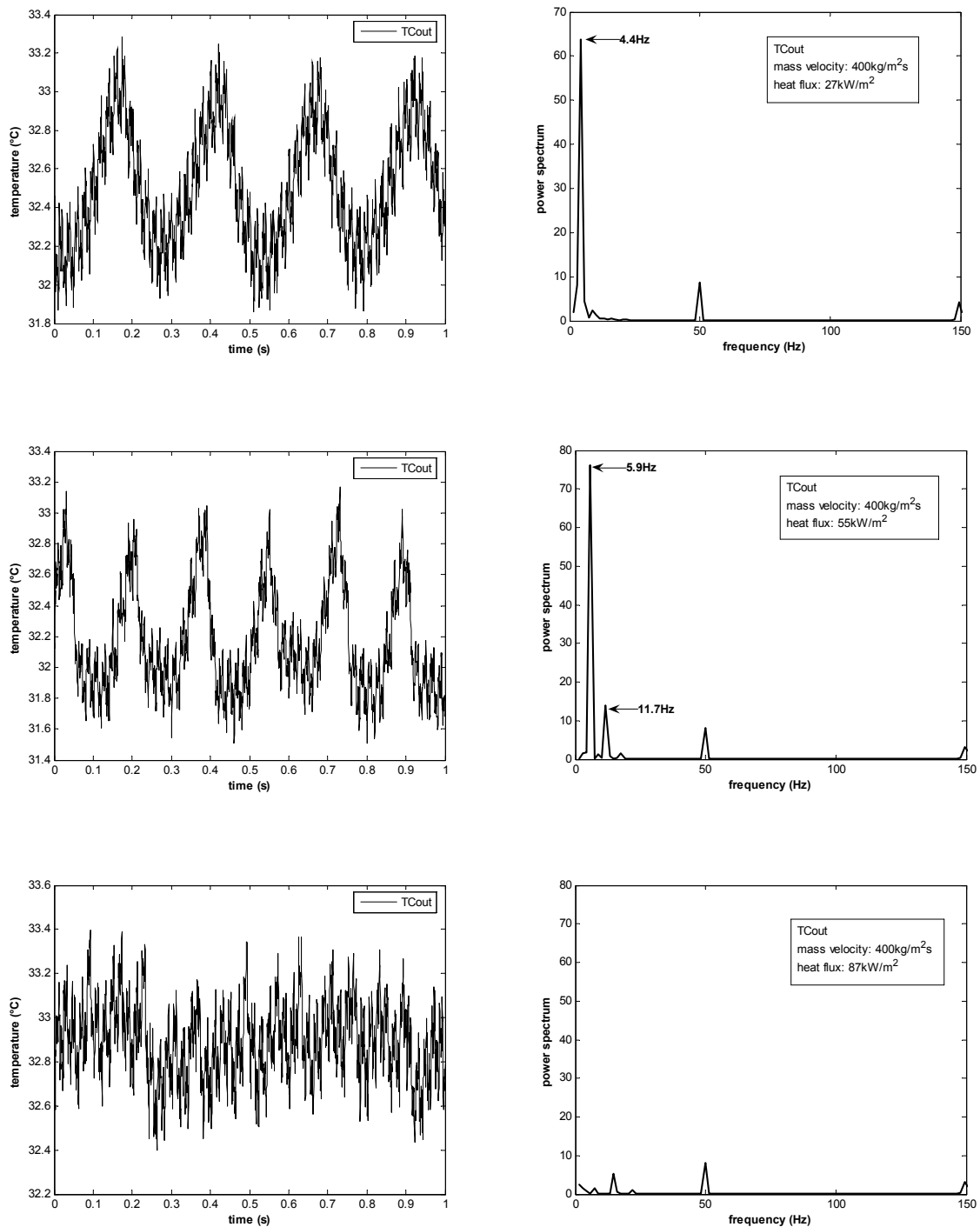


Figure 58. Fluctuations in the fluid temperature at the exit of the evaporator and corresponding power spectrums for flow boiling of R-245fa at different heat fluxes (510 μ m tube).

play an important role. This appears even clearer at the highest heat flux, where the oscillation in the fluid temperature is reduced to irregular noise, while the wall temperature fluctuates vigorously (note that the plots in Fig. 57 refer to the thermocouple closest to the exit).

The features of the temperature oscillations are also affected by the axial measurement location. Figure 59 shows the temperatures from the first and last thermocouples on the heated length for a flow of R-236fa. The amplitude of the temperature fluctuation of the first thermocouple is lower with respect to the one further downstream. While the last temperature on the heated length has one main oscillation mode at 5.4Hz, the first presents two frequencies: a main one at 2.4Hz and a secondary mode at 7.8Hz.

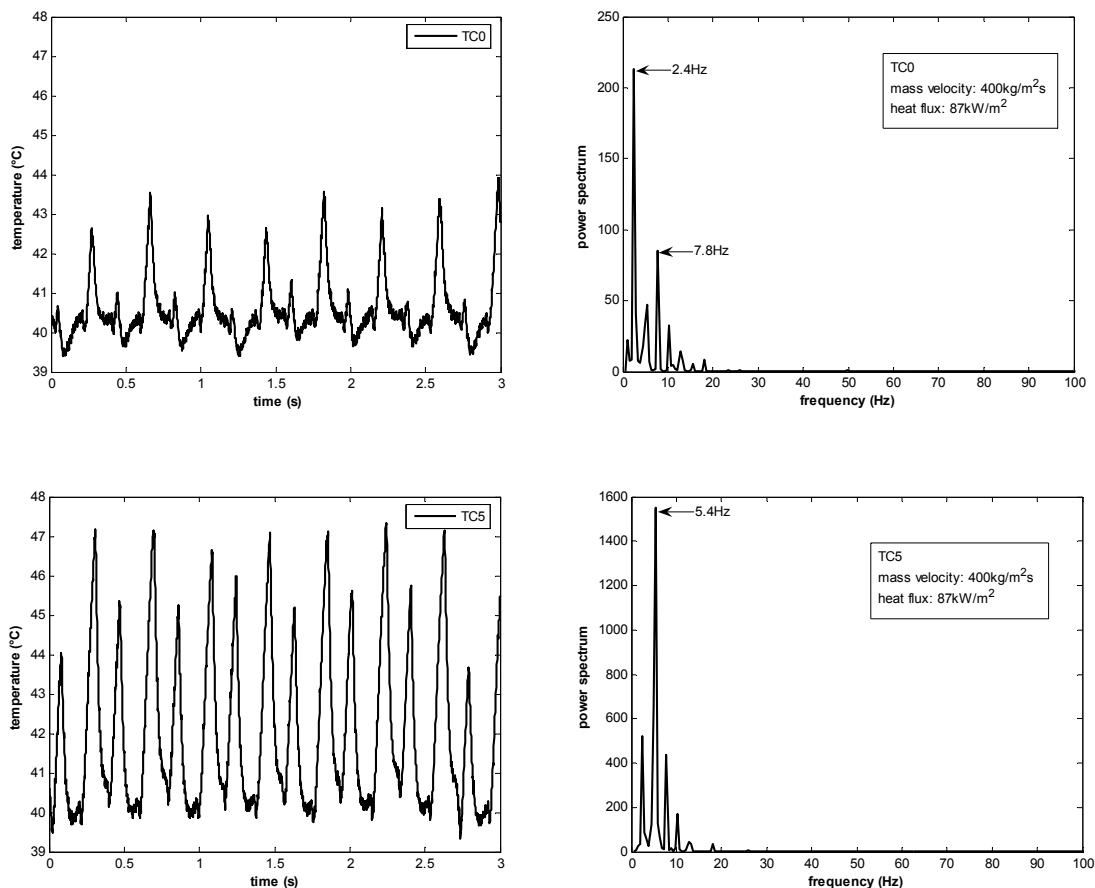


Figure 59. Wall temperature fluctuations from the first and last thermocouples (19 and 65mm from the inlet respectively) on the heated length, for unstable flow boiling of R-236fa at a heat flux of 87 kW/m^2 and an average mass velocity of $400\text{ kg/m}^2\text{s}$.

As a final note on the nature of the instability, in the analysis presented in Section 2.4 and in the Appendix, the pressure drop oscillations result from a change in the supply pressure due to a perturbation in the flow rate. The present system has instead a constant upstream pressure (the pressure in vessel A remains constant), and should thus be immune from the periodic phenomenon. However, the bubble formation process delivers cyclical pressure pulses that force the system into oscillation by displacing liquid into the compressible volume (refer to Fig. 55). Of the three fluids considered for the current study, R-245fa, the lowest pressure fluid, exhibits the highest sensitivity to the instability. This is mainly due to two reasons: (1) the compressibility of an upstream body of vapor may be enough to produce the oscillatory behavior (cfr. Eq. (2.1)), and the vapor phase of R-245fa

presents the lowest stiffness (Fig. 60 illustrates the absolute value of the vapor stiffness of each fluid, here defined as $(\partial p / \partial v)_T = -\rho^2 (\partial p / \partial \rho)_T$, for temperatures ranging from 25 to 35°C), and (2) R-245fa presents the highest two-phase pressure drop (R-245fa combines a high liquid viscosity with a low vapor density, as mentioned earlier in Chapter 4), thus its internal characteristic is shifted upward in the pressure drop versus flow rate plane, yielding a higher value for the critical flow rate.

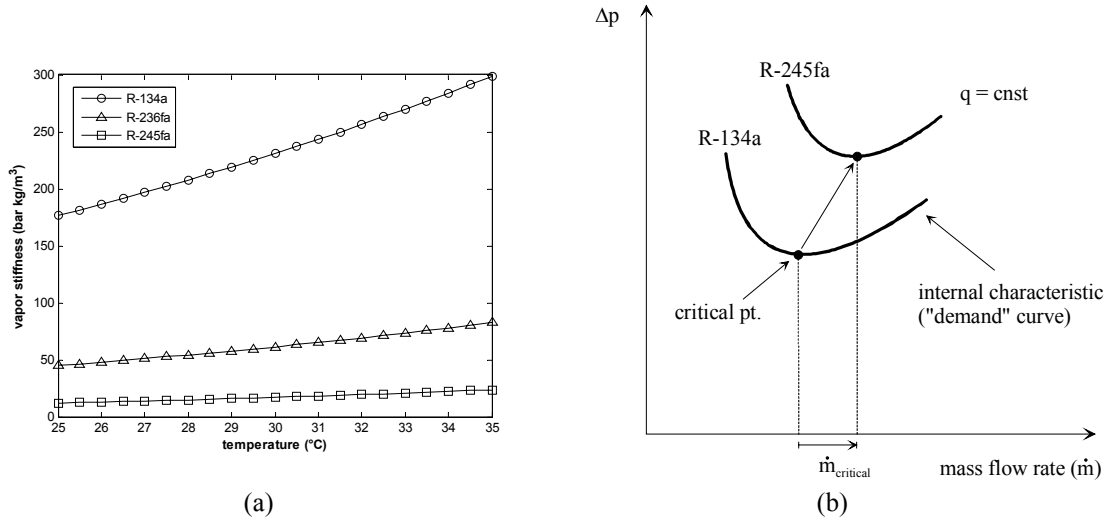


Figure 60. (a) Liquid compressibility of the three fluids tested from 25 to 35°C, and (b) the change in the internal characteristic for different fluids.

5.2 Estimating Steady Heat Transfer Coefficients from Unstable Flows

An unstable flow presents fundamentally different characteristics from the stable case. Such differences may translate into substantial error in the assessment of local heat transfer if the instability is neglected. Figure 61, for example, compares corresponding heat transfer measurements for four sets of data: one refers to a stable flow of R-245fa, while the remaining three refer to flows exposed to instabilities of different degrees. The data for the unstable cases are computed through the same assumptions as for stable flows (thermodynamic equilibrium and stability), with a time-averaged wall temperature (over a 3s period). This procedure yields only apparent heat transfer coefficients, and not the real values that would also require the actual local fluid temperature. For the run with mild oscillations (i.e. a maximum amplitude in the outer wall temperature of $\Delta T_1 \approx 0.5^\circ\text{C}$), the heat transfer coefficients behave as in the case of a stable flow. However, once the flow becomes fully unstable, the outer wall temperature fluctuations reach amplitudes of $\Delta T_1 \approx 4^\circ\text{C}$, and their mean values change, delivering completely different trends in the α - x plane. Fig. 61 shows an absolute deviation from the stable flow data of 42% at a vapor quality $x = 0.26$.

Although the largest error in the heat transfer coefficients occurs for R-245fa, R-236fa also exhibits similar differences with respect to equivalent stable flow boiling. On the other hand, R-134a requires the highest heat flux for the instabilities to propagate. Figure 62 compares sets of data showing stable versus unstable heat transfer trends for R-236fa and R-134a at a fixed heat flux and mass velocity. For the given operating conditions, the local heat transfer coefficients for R-134a from an unstable flow are essentially identical to those for stable flow, while for the two low pressure fluids this is not so.

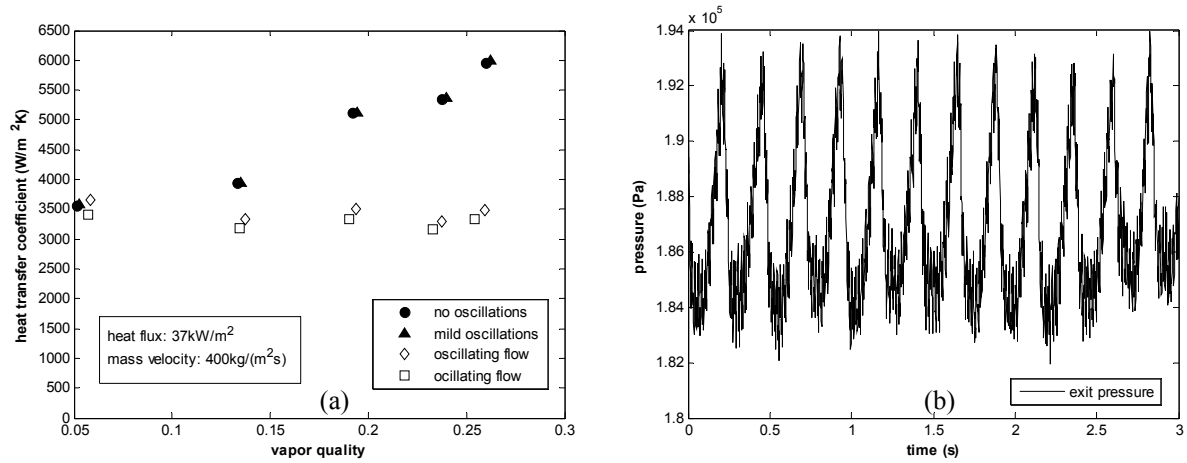


Figure 61. (a) Stable and unstable heat transfer coefficients for R-245fa with $D = 510\mu m$, $T_{in} = 30^\circ C$ and $T_{out} = 32^\circ C$, and (b) fluctuations in the pressure at the exit to the evaporator for the fully unstable flows.

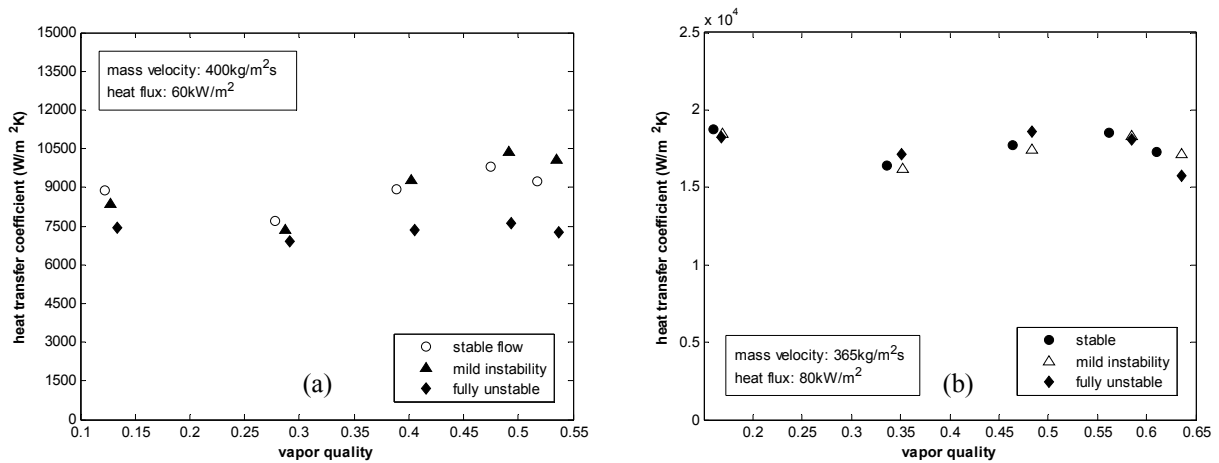


Figure 62. Heat transfer coefficients computed from stable and unstable flow data for (a) R-236fa at $30^\circ C$, and (b) R-134a at $31^\circ C$. $D = 510\mu m$ in both cases.

The apparent heat transfer data for flows affected by the oscillatory phenomenon generally show minimal influence of mass velocity, with slightly downward trends with vapor quality in the α -x plane, as shown in Fig. 63, and as was noticed in the investigation by Xu and coworkers [30]. The coefficients are often seen to increase with heat flux (see Figs. 64a and 64b), although not in all cases. From some of the data, it appears that for sufficiently high heat fluxes the heat transfer coefficients become less sensitive to q , as illustrated in Figs. 64c and 64d for R-236fa.

5.3 Summary

A flow affected by a compressible volume instability is exposed to oscillations in local pressure/temperature and heat transfer mechanisms. The global effect on the heated wall is a corresponding temperature oscillation, which combines both of these effects. Assessing local heat transfer coefficients from a flow that is subjected to instability, neglecting the fluctuations, may lead to a substantial deviation from a corresponding stable flow. It is therefore of paramount importance to distinguish between stable and oscillating two-phase flows in the measurement of flow boiling heat transfer coefficients in micro-channels, in order to avoid superposing data of two different natures in the development and validation of two-phase heat transfer models and correlations.

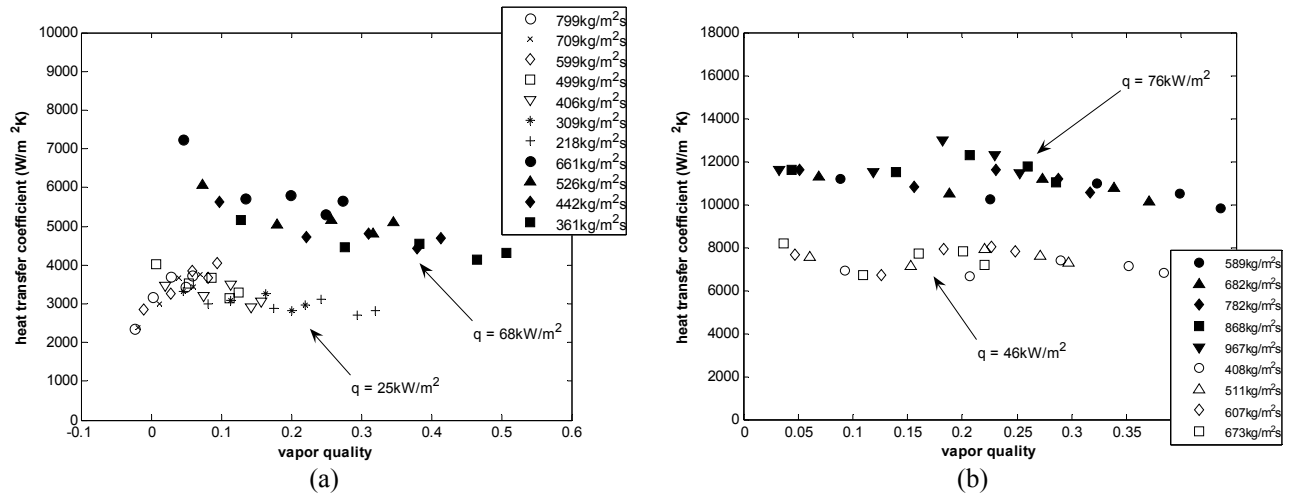


Figure 63. Heat transfer coefficients computed from unstable flow data for (a) R-245fa at 32°C, and (b) R-236fa at 31°C. The coefficients are shown for two levels of heat flux and a range of mass velocities and $D = 510\mu\text{m}$.

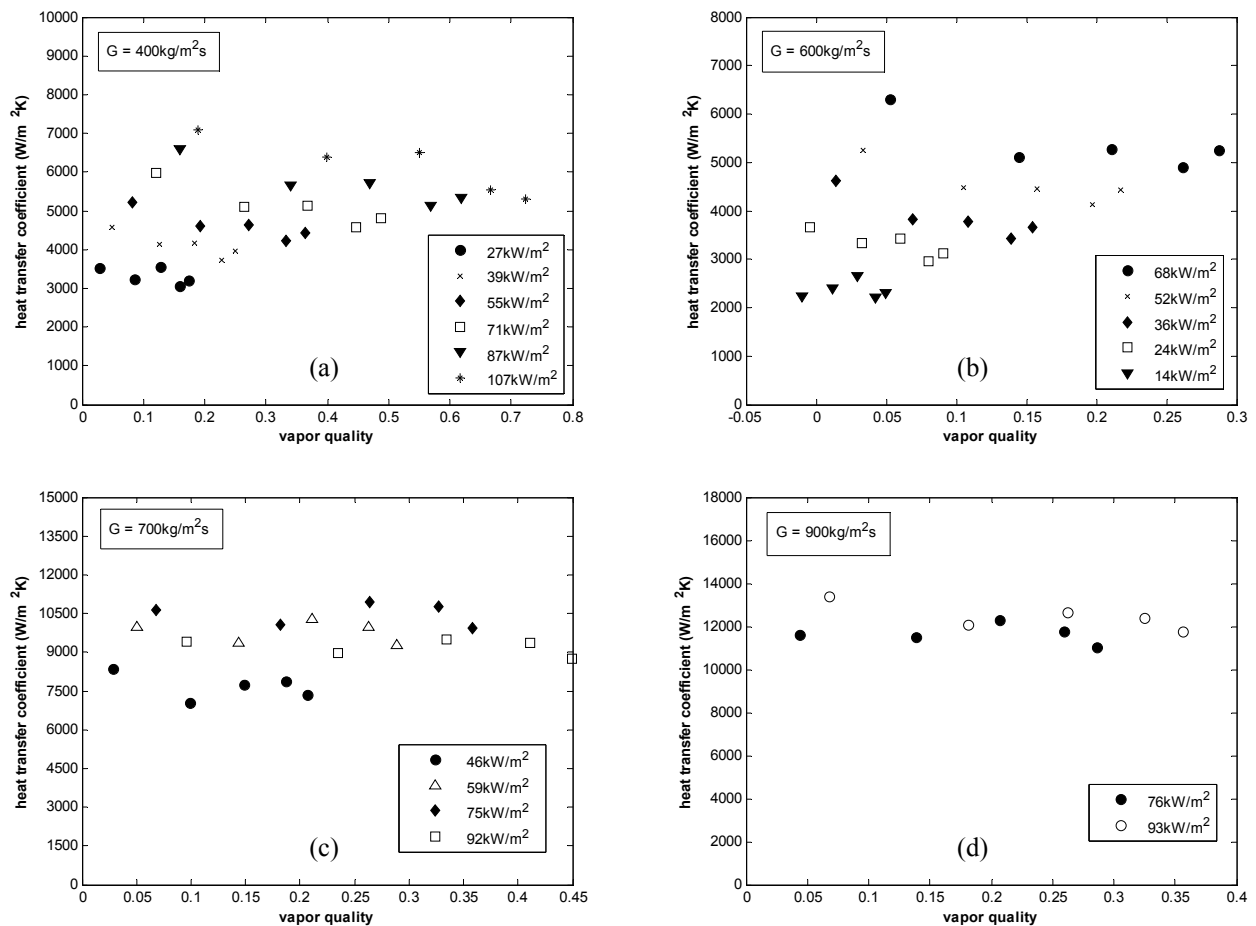


Figure 64. Heat transfer coefficients computed from unstable flow data for fixed mass velocities and different heat fluxes, $D = 510\mu\text{m}$, and (a) R-245fa at 33°C with $G = 400\text{kg/m}^2\text{s}$, (b) R-245fa at 33°C with $G = 600\text{kg/m}^2\text{s}$, (c) R-236fa at 31°C with $G = 700\text{kg/m}^2\text{s}$, and (d) R-236fa at 31°C with $G = 900\text{kg/m}^2\text{s}$.

Chapter 6

One-Dimensional Analysis of Confined Slug Flow

As discussed in Chapter 2, a micro-channel two-phase flow presents itself as a slug flow at low and intermediate vapor qualities. A slug flow may be described as the cyclical passage of a liquid slug followed by an elongated bubble (a bubble whose length is greater than the channel diameter). Thome and coworkers [12] gave a first description of the heat transfer mechanisms characteristic to a slug flow in their “three-zone model”, assuming a homogenous velocity for the two phases, Eq. (2.19), and adopting the correlations from Moriyama and Inoue, Eq. (2.24), for the liquid film surrounding the elongated bubbles (cfr. Section 2.5). The discussion that follows represents a continuation of that effort, and is aimed at further describing the dynamics of the flow process in order to determine local heat transfer characteristics. The expressions developed below rely on the following assumptions:

1. The two phases are in thermodynamic equilibrium, with no liquid superheating.
2. Bubble nucleation only occurs at the origin of the heated length, with a constant formation period, Δt .
3. The liquid flow in the thin film surrounding the bubbles is laminar, and is driven primarily by a constant interfacial shear, τ_i .
4. Heat is transferred through the liquid film only by conduction.
5. The liquid film thickness is small compared to the channel size: $\delta \ll R$.
6. The mass flow of liquid through the film is negligible with respect to the total mass flow.
7. The wall heat flux is uniform and constant.

6.1 Dynamic Thin Film Evaporation

Figure 65 illustrates an elongated bubble during its flow through a heated circular channel. An analysis over the control volume (CV) in Fig. 65 yields the following mass and energy balances for the liquid film. Applying mass conservation,

$$\frac{\partial}{\partial t} (dm_{CV}) = \dot{m} - \left(\dot{m} + \frac{\partial \dot{m}}{\partial z} dz \right) - 2\pi(R - \delta) \dot{m}_{evp}'' dz \quad (6.1)$$

with \dot{m}_{evp}'' the evaporating mass flux. Introducing the average liquid film velocity in the z direction, W , Eq. (6.1) may be restated as

$$\frac{\partial}{\partial t} \left[\frac{\delta}{R} \left(2 - \frac{\delta}{R} \right) \right] + \frac{\partial}{\partial z} \left[W \frac{\delta}{R} \left(2 - \frac{\delta}{R} \right) \right] = - \frac{2}{\rho_l R} \left(1 - \frac{\delta}{R} \right) \dot{m}_{evp}'' \quad (6.2)$$

In the same fashion, energy conservation yields

$$\frac{\partial}{\partial t} (dE_{CV}) = \dot{H} - \left(\dot{H} + \frac{\partial \dot{H}}{\partial z} dz \right) - 2\pi(R - \delta) h_v \dot{m}_{evp}'' dz + 2\pi R q dz \quad (6.3)$$

with \dot{H} the enthalpy flow rate of liquid entering the control volume, h_v the specific enthalpy of the vapor, and q the constant wall heat flux. Inserting into Eq. (6.3) the explicit forms of the enthalpy flow and the internal energy (dE_{CV}), gives

$$\frac{\partial}{\partial t} \left[\frac{\delta}{R} \left(2 - \frac{\delta}{R} \right) \right] + \frac{\partial}{\partial z} \left[W \frac{\delta}{R} \left(2 - \frac{\delta}{R} \right) \right] = - \frac{2h_v}{\rho_l h_l R} \left(1 - \frac{\delta}{R} \right) \dot{m}''_{evp} + \frac{2q}{\rho_l h_l R} \quad (6.4)$$

with h_l the specific enthalpy of the liquid. The governing equation for the film thickness is given by combining Eqs. (6.2) and (6.4):

$$\frac{\partial}{\partial t} \left[\frac{\delta}{R} \left(2 - \frac{\delta}{R} \right) \right] + \frac{\partial}{\partial z} \left[W \frac{\delta}{R} \left(2 - \frac{\delta}{R} \right) \right] = - \frac{2q}{\rho_l h_{lv} R} \quad (6.5)$$

Applying the assumption of a thin film ($\delta/R \ll 1$), Eq. (6.5) simplifies to

$$\frac{\partial \delta}{\partial t} + \frac{\partial}{\partial z} (W\delta) = - \frac{q}{\rho_l h_{lv}} \quad (6.6)$$

Assuming the flow to be driven by interfacial shear (τ_i), and neglecting inertial contributions, the momentum balance in the z direction may be expressed as

$$0 = 2\pi(R - \delta)\tau_i dz + \mu_l \frac{\partial w}{\partial r} 2\pi r dz \quad (6.7)$$

with r the radial coordinate in the liquid film, and w the local axial velocity. Equation (6.7) gives the velocity distribution in the film as

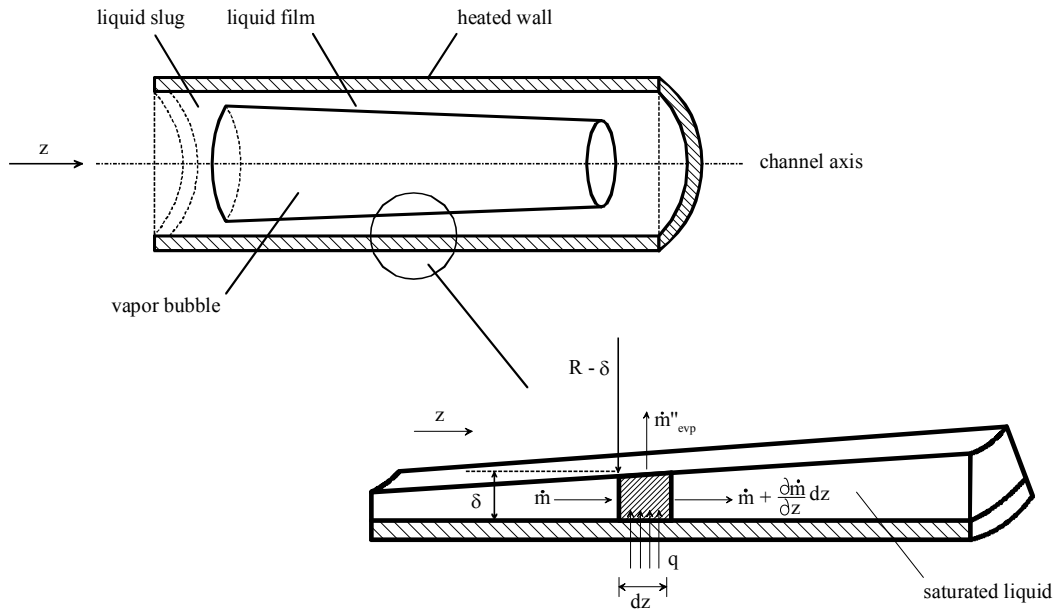


Figure 65. Schematic representation of an elongated bubble, and the control volume for the analysis of the liquid film.

$$w(r) = -\frac{1}{\mu_1}(R - \delta)\tau_i \ln\left(\frac{r}{R}\right) \quad (6.8)$$

which may be integrated over the cross-sectional area of the film to yield the mean film velocity,

$$W = \frac{1}{A} \int_A w dA' = -\frac{(R - \delta)\tau_i}{\mu_1 \pi \delta (2R - \delta)} \int_{R-\delta}^R \ln\left(\frac{r}{R}\right) 2\pi r dr \quad (6.9)$$

Performing the integral in Eq. (6.9):

$$W = \frac{\tau_i R}{\mu_1} \left[\frac{\left(1 - \frac{\delta}{R}\right)^3}{\frac{\delta}{R} \left(2 - \frac{\delta}{R}\right)} \ln\left(1 - \frac{\delta}{R}\right) + \frac{1}{2} \left(1 - \frac{\delta}{R}\right) \right] \quad (6.10)$$

Observing that for $\delta/R \ll 1$,

$$\frac{\ln\left(1 - \frac{\delta}{R}\right)}{2 - \frac{\delta}{R}} \sim -\frac{1}{2} \frac{\delta}{R} \left(1 + \frac{\delta}{R}\right) + O\left[\left(\frac{\delta}{R}\right)^3\right] \quad (6.11)$$

Eq. (6.10) simplifies to

$$W \sim \frac{\tau_i \delta}{2\mu_1} + O(\delta^2) \quad (6.12)$$

Inserting Eq. (6.12) into Eq. (6.6), and dropping the higher order terms in δ yields,

$$\frac{\partial \delta}{\partial t} + \frac{\tau_i}{\mu_1} \delta \frac{\partial \delta}{\partial z} = -\frac{q}{\rho_1 h_{lv}} \quad (6.13)$$

A particular solution to Eq. (6.13) may be sought by utilizing the solution to the homogenous (adiabatic) form of the equation,

$$\frac{\partial \delta}{\partial t} + \frac{\tau_i}{\mu_1} \delta \frac{\partial \delta}{\partial z} = 0 \quad \text{for which} \quad \delta(t, z) = \frac{\mu_1}{\tau_i} \frac{z}{t} \quad (6.14)$$

Equation (6.14) satisfies the boundary condition $\delta(t, 0) = 0$ and the condition for film depletion, $\lim_{t \rightarrow \infty} \delta(t, z) = 0$. Assuming a solution to Eq. (6.13) of the form

$$\delta(t, z) = \delta_0(t, z) + \delta_1(t) \quad (6.15)$$

with δ_0 the homogenous solution (Eq. (6.14)) and δ_1 an unknown function of time, and inserting it into the original differential equation yields:

$$\frac{\partial \delta_0}{\partial t} + \frac{\tau_i}{\mu_1} \delta_0 \frac{\partial \delta_0}{\partial z} + \frac{d\delta_1}{dt} + \frac{\tau_i}{\mu_1} \delta_1 \frac{\partial \delta_0}{\partial z} = -\frac{q}{\rho_1 h_{lv}} \quad (6.16)$$

The sum of the first two terms on the left hand side of Eq. (6.16) is equal to zero by the homogeneous equation, while the partial derivative $\partial \delta_0 / \partial z$ is known from Eq. (6.14) to be $\mu_l / (\tau_i t)$. Equation (6.16) may now be rewritten as an ordinary differential equation in δ_1 (or in δ_1/t),

$$t \frac{d}{dt} \left(\frac{\delta_1}{t} \right) = -\frac{q}{\rho_1 h_{lv}} - 2 \frac{\delta_1}{t} \quad (6.17)$$

The solution to Eq. (6.17) is

$$\delta_1(t) = -\frac{1}{2t} \left(\frac{q t^2}{\rho_1 h_{lv}} + C^2 \right) \quad (6.18)$$

where C is the integration constant. Therefore,

$$\delta(t, z) = \frac{\mu_1}{\tau_i} \frac{z}{t} - \frac{1}{2t} \left(\frac{q t^2}{\rho_1 h_{lv}} + C^2 \right) \quad (6.19)$$

Equation (6.19) shows that for any non-zero value of C , δ approaches $-\infty$ for $t \rightarrow 0$ over values of z less than $C^2 \tau_i / (2\mu_l)$, while tending to $+\infty$ over the remaining domain. To avoid this non-uniformity in the initial condition, C is set to 0, and the time-varying thickness of the liquid film may be expressed by the following equation:

$$\delta(t, z) = \frac{\mu_1}{\tau_i} \frac{z}{t} - \frac{q}{2\rho_1 h_{lv}} t \quad (6.20)$$

In the context of an evaporating elongated bubble, assuming bubble nucleation to occur at the origin of the heated length ($z = 0$) at $t = 0$, Eq. (6.20) represents the behavior of the liquid film deposited by a liquid slug during its passage through the channel. Figure 66 shows the temporal evolution of the film thickness (as from Eq. (6.20)) and the bubble nose (the vertical segments in Fig. 66) at the early stages of their development. Locally, the film thickness shrinks in time due to the combined effect of the vaporization process and the drag exerted by the vapor phase. A zero or negative value of δ is indicative of film dry-out.

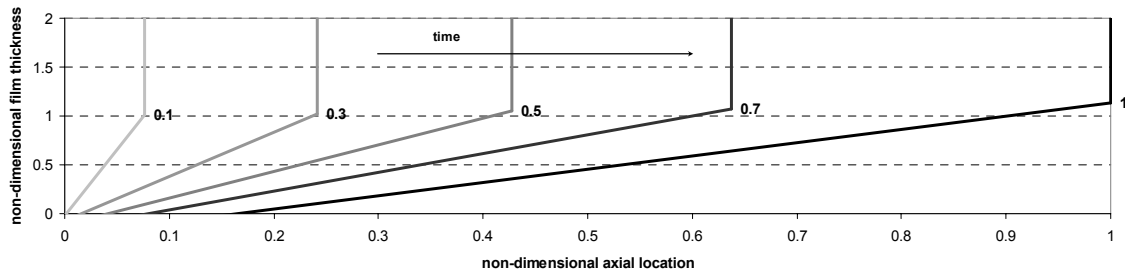


Figure 66. Temporal evolution of the liquid film and the bubble nose before bubble-slug departure (the bubble tail is not shown). The film thickness, the axial coordinate, and time are reduced respectively by the initial film thickness, the bubble-slug departure length, and the passage period.

6.2 Liquid and Vapor Velocities at the Bubble Nose

As mentioned earlier, the slug flow modeled for this analysis is a cyclical passage of liquid slugs and elongated bubbles. The present objective is to obtain a sufficiently realistic representation of the flow development, in order to extend the conclusion to the evaluation of its performance in terms of heat transfer. Equation (6.20) provides a starting point, giving an estimate of the behavior of the liquid film flowing adjacent to the bubble. The next steps will be directed towards acquiring a description, in time and in space, of the dynamic parameters of the bubble-slug pair, i.e. bubble nose speed, nose film thickness, bubble-slug lengths, etc.

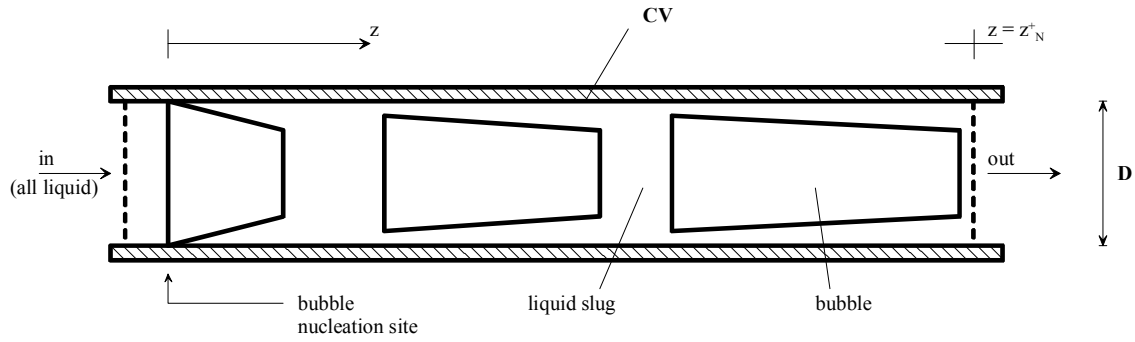


Figure 67. The control volume for the determination of the liquid slug velocity.

Consider the slug flow in the uniformly heated channel illustrated in Fig. 67. For a control volume with the left boundary in the all-liquid region prior to the heated length, and the right boundary immediately after the nose interface of a non-specified bubble (located at $z = z_N^+$, with z_N the axial coordinate of the bubble nose), mass conservation yields,

$$\frac{dm_{CV}}{dt} = G\pi R^2 - \rho_l W_{N,l}\pi R^2 \quad (6.21)$$

where G is the total flow mass velocity, R is the channel radius, and $W_{N,l}$ is the axial velocity of the liquid slug (Fig. 67). Indicating with V_l and V_v the volumes of the liquid and vapor within the control volume, then $dV_l/dt + dV_v/dt = 0$, and Eq. (6.21) becomes

$$W_{N,l} = \frac{G}{\rho_l} + \left(1 - \frac{\rho_v}{\rho_l}\right) \frac{1}{\pi R^2} \frac{dV_v}{dt} \quad (6.22)$$

which gives the slug velocity as the sum of the speed of the liquid entering the channel plus a contribution due to the phase-change expansion occurring within the control volume. An energy balance on the same control volume gives

$$\frac{dE_{CV}}{dt} = G\pi R^2 h_l - \rho_l W_{N,l}\pi R^2 h_l + 2\pi R q z_N \quad (6.23)$$

The change in internal energy of the saturated system, dE_{CV} , may be expressed in terms of the specific internal energies, u_l and u_v , or equivalently in terms of the specific enthalpies of the two phases: $dE_{CV} \equiv d(\rho_l V_l u_l + \rho_v V_v u_v) = d(\rho_l V_l h_l + \rho_v V_v h_v)$. Thus from Eq. (6.23)

$$W_{N,l} = \frac{G}{\rho_l} + \left(1 - \frac{\rho_v h_v}{\rho_l h_l}\right) \frac{1}{\pi R^2} \frac{dV_v}{dt} + \frac{q}{\rho_l h_l} \frac{2z_N}{R} \quad (6.24)$$

Combining Eqs. (6.22) and (6.24),

$$W_{N,l} = \frac{G}{\rho_l} + \frac{2q}{h_{lv}} \left(\frac{1}{\rho_v} - \frac{1}{\rho_l} \right) \frac{z_N}{R} \quad (6.25)$$

In a similar way, the speed of the vapor at the nose of the bubble may be derived considering the control volume in Fig. 67, with the outer boundary immediately before the nose interface (at $z = z_N^-$). The total flow exiting the control volume will include the liquid flow through the film thickness, and the inner-core vapor flow. The velocity of the liquid film may be taken from Eq. (6.12) as $W_{N,f} = \tau_i \delta_N / (2\mu_l)$, with δ_N being the nose film thickness. Performing a mass and energy balance as was done for the liquid slug yields the vapor velocity at the bubble nose as

$$W_{N,v} = \frac{1}{\left(1 - \frac{\delta_N}{R}\right)^2} \left[\frac{G}{\rho_l} - \frac{\tau_i R}{2\mu_l} \frac{\delta_N^2}{R^2} \left(2 - \frac{\delta_N}{R}\right) + \frac{2q}{h_{lv}} \left(\frac{1}{\rho_v} - \frac{1}{\rho_l} \right) \frac{z_N}{R} \right] \quad (6.26)$$

6.3 Bubble Nose Velocity

The motion of the interface at the bubble nose will compensate for the net flow of liquid and vapor through the control volume shown in Fig. 68. Referring to Fig. 68,

$$\frac{d}{dt} (dm_{CV}) = \rho_v W_{N,v} \pi (R - \delta_N)^2 + \rho_l W_{N,f} \pi \delta_N (2R - \delta_N) - \rho_l W_{N,l} \pi R^2 \quad (6.27)$$

The elementary mass dm_{CV} includes the contributions from the two phases as

$$dm_{CV} = \rho_v \pi (R - \delta_N)^2 dz_- + \rho_l \pi R^2 dz_+ + \rho_l \pi \delta_N (2R - \delta_N) dz_- \quad (6.28)$$

with dz_+ and dz_- the widths, included in the CV, respectively to the right and left of the nose interface (the total width of the control volume, dz , is thus $dz = dz_- + dz_+$). The time derivative of Eq. (6.28) gives

$$\frac{d}{dt} (dm_{CV}) = -(\rho_l - \rho_v) \pi (R - \delta_N)^2 \frac{d}{dt} (dz_-) = -(\rho_l - \rho_v) \pi (R - \delta_N)^2 W_N \quad (6.29)$$

having specified the velocity of the interface, W_N , as $W_N \equiv \frac{d}{dt} (dz_-) = -\frac{d}{dt} (dz_+)$. Equations (6.27) and (6.29) may be solved to yield the bubble nose speed as:

$$W_N = \frac{1}{\left(1 - \frac{\delta_N}{R}\right)^2} \left[\frac{G}{\rho_l} - \frac{\tau_i R}{2\mu_l} \frac{\delta_N^2}{R^2} \left(2 - \frac{\delta_N}{R}\right) + \frac{2q}{h_{lv}} \left(\frac{1}{\rho_v} - \frac{1}{\rho_l} \right) \frac{z_N}{R} \right] \quad (6.30)$$

which is the same expression found in Eq. (6.26) for the vapor.

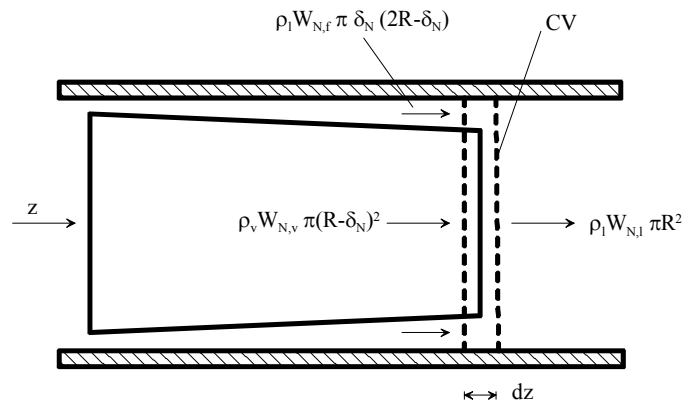


Figure 68. Control volume and mass flows for the evaluation of the bubble nose velocity.

6.5 Bubble Nose Position and Film Thickness

The expression for the position in time of the bubble nose is given by integrating Eq. (6.30), and simultaneously solving for the film thickness δ_N . For a thin film, on the other hand, this procedure simplifies considerably. For $\delta_N/R \ll 1$, and applying the assumption of negligible liquid film flow rate (see the above assumption 5), Eq. (6.30) yields (for $\rho_v \ll \rho_l$),

$$\frac{dz_N}{dt} = \frac{G}{\rho_l} + \frac{2q}{\rho_v h_{lv}} \frac{z_N}{R} \quad (6.31)$$

which, with the initial condition $z_N(0) = 0$, integrates to

$$z_N(t) = \frac{G}{\rho_l} \frac{\rho_v h_{lv} R}{2q} \left[\exp\left(\frac{2q}{\rho_v h_{lv} R} t\right) - 1 \right] \quad (6.32)$$

Inserting Eq. (6.32) into Eq. (6.20) gives the time law of the nose film thickness,

$$\delta_N(t) = \frac{G \mu_l}{\rho_l \tau_i} \frac{\rho_v h_{lv} R}{2q} \left[\frac{\exp\left(\frac{2q}{\rho_v h_{lv} R} t\right) - 1}{t} - \frac{q}{2\rho_l h_{lv}} t \right] \quad (6.33)$$

The initial film thickness results from taking the limit for $t \rightarrow 0$ of Eq. (6.33),

$$\delta_{N0} \equiv \lim_{t \rightarrow 0} \delta_N(t) = \frac{G\mu_1}{\rho_1 \tau_i} \quad (6.34)$$

The value from Eq. (6.34) represents the nose film thickness at the instant the bubble forms (see Fig. 66).

The only unknown parameter in Eqs. (6.33) and (6.34) is the interfacial shear stress, τ_i , which will be determined on an empirical basis. The interfacial shear depends on those quantities that will affect the flow field in the liquid film and in the vapor core. Among these, mass velocity and channel size are likely to play a role, as well as the fluid properties. In addition, for the adiabatic case Eqs. (6.20) and (6.33) reduce respectively to

$$\delta^{(ad)}(t, z) = \frac{\mu_l}{\tau_i} \frac{z}{t} \quad \text{and} \quad \delta_N^{(ad)} \equiv \lim_{q \rightarrow 0} \delta_N(t) = \frac{G\mu_l}{\rho_l \tau_i} \quad (6.35)$$

Having assumed a saturated liquid flow at $z = 0$, no vapor (or liquid film) is expected for an adiabatic flow. When no heating is applied, Eqs. (6.34) and (6.35) should all tend to an indefinitely large value (which under all real circumstances is equal to the channel radius), suggesting a link between the interfacial shear stress and the rate of mass transfer at the interface. As for the fluid properties, it was shown in Chapter 4 that among the three fluids tested the main differences are for surface tension, vapor density, and liquid viscosity. Having neglected the effect of interfacial curvature, and the possible development of interfacial waves, it seems reasonable to include in the correlation for τ_i only values of density and viscosity. On these grounds, the following non-dimensional equation correlates the stable flow heat transfer data presented in Chapter 4, for the isolated bubble and coalescing bubble flow modes,

$$\frac{\tau_i \rho_v}{G^2} = 1273 \left(\frac{GR}{\mu_l} \right)^{-1.17} \left(\frac{\rho_v}{\rho_l} \right)^{1.73} \left(\frac{\mu_l}{\mu_v} \right)^{1.44} \left(\frac{R}{L} \right)^{0.44} \left[1 - \exp \left(-6.83 \times 10^{-3} \frac{qL}{h_{lv} \mu_l} \right) \right] \quad (6.36)$$

The first four groups at the right hand side of Eq. (6.36) account respectively for the flow Reynolds number, fluid properties, and channel geometry. The last non-dimensional parameter represents the evaporative liquid Reynolds number. Figure 69 shows the temporal variation of the nose film thickness, as given by Eqs. (6.33) and (6.36).

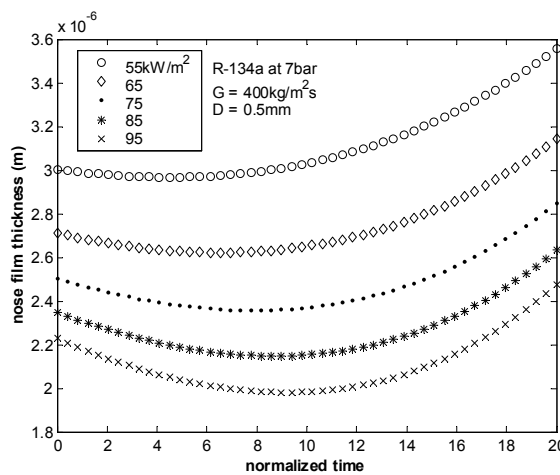


Figure 69. Nose film thickness versus time, as predicted by Eqs. (6.33) and (6.36) for a slug flow of R-134a at different levels of heat flux. Time is normalized by the bubble-slug passage period, Δt (Eq. (6.42)).

6.5 Liquid and Vapor Residence Times

A stationary observer examining the passage of a slug flow through a heated channel will experience (1) the passage of the bubble nose, (2) the flow of the liquid film surrounding the bubble, and finally (3) the passage of a slug of liquid. This sequence will repeat itself cyclically with a characteristic time period equal to the bubble nucleation period, Δt , assuming nucleation to take place at $z = 0$. The local residence times, Δt_v and Δt_l , of the two phases over one time period are given by considering the definition of vapor quality, x , at a location z along the heated length,

$$x = \frac{1}{G\pi R^2 \Delta t} \int_{\Delta t_v} \rho_v W_v \pi (R - \delta)^2 dt \quad (6.37)$$

and the energy balance,

$$2\pi R z q = G\pi R^2 x h_{lv} \quad (6.38)$$

The local velocity of the vapor phase, W_v , may be determined by the same procedure used in Section 6.3 to obtain the liquid and vapor velocities at the bubble nose, which yields

$$W_v = \frac{1}{\left(1 - \frac{\delta}{R}\right)^2} \left[\frac{G}{\rho_l} - \frac{\tau_i R}{2\mu_l} \frac{\delta^2}{R^2} \left(2 - \frac{\delta}{R}\right) + \frac{2q}{h_{lv}} \left(\frac{1}{\rho_v} - \frac{1}{\rho_l}\right) \frac{z}{R} \right] \quad (6.39)$$

Applying the thin film assumption and solving Eqs. (6.37), (6.38) and (6.39) for Δt_v gives

$$\Delta t_v(z) = \frac{\Delta t}{1 + \frac{\rho_v}{\rho_l} \frac{G h_{lv}}{2q} \frac{R}{z}} \quad (6.40)$$

having set $\rho_v \ll \rho_l$. For the residence time of the liquid slug, Δt_l ,

$$\Delta t_l(z) = \Delta t - \Delta t_v(z) = \frac{\Delta t}{1 + \frac{\rho_l}{\rho_v} \frac{2q}{G h_{lv}} \frac{z}{R}} \quad (6.41)$$

The bubble nucleation frequency is seen experimentally to increase with heat flux (see [Thome]). Figure 2b in Chapter 2 (taken from [9]) illustrated the characteristic passage frequency, f ($= 1/\Delta t$), of the bubbles exiting the heated channel, for a flow of R-134a at a mass velocity of $500 \text{ kg/m}^2\text{s}$. The frequency exhibits a strong increase with heat flux at the low heating values, while beyond 10% in exit vapor quality, it starts descending due to the onset of bubble coalescence, as pointed out in [9]. The passage period/frequency of the bubble-slug pair is thus correlated as a function of the heat flux, channel size and of fluid properties. Buckingham's π theorem yields the following non-dimensional form,

$$\frac{f \sigma}{q} = 2000 \left(\frac{\sigma^3 R^3}{q^2 \rho_v} \right)^{0.25} \quad (6.42)$$

Equations (6.32) and (6.42) give the bubble-slug pair length, L_p , at time $t > \Delta t$ as,

$$L_p(t) = z_N(t) - z_N(t - \Delta t) = \frac{G}{\rho_l} \frac{\rho_v h_{lv} R}{2q} \left[1 - \exp\left(-\frac{2q}{\rho_v h_{lv} R} \Delta t\right) \right] \exp\left(\frac{2q}{\rho_v h_{lv} R} t\right) \quad (6.43)$$

while for $0 < t \leq \Delta t$,

$$L_p(t) = z_N(t) = \frac{G}{\rho_l} \frac{\rho_v h_{lv} R}{2q} \left[\exp\left(\frac{2q}{\rho_v h_{lv} R} t\right) - 1 \right] \quad (6.44)$$

Figure 70 shows the position in time of the bubble-slug pair. As the evaporation progresses, the length increases exponentially as described by Eqs. (6.43) and (6.44).

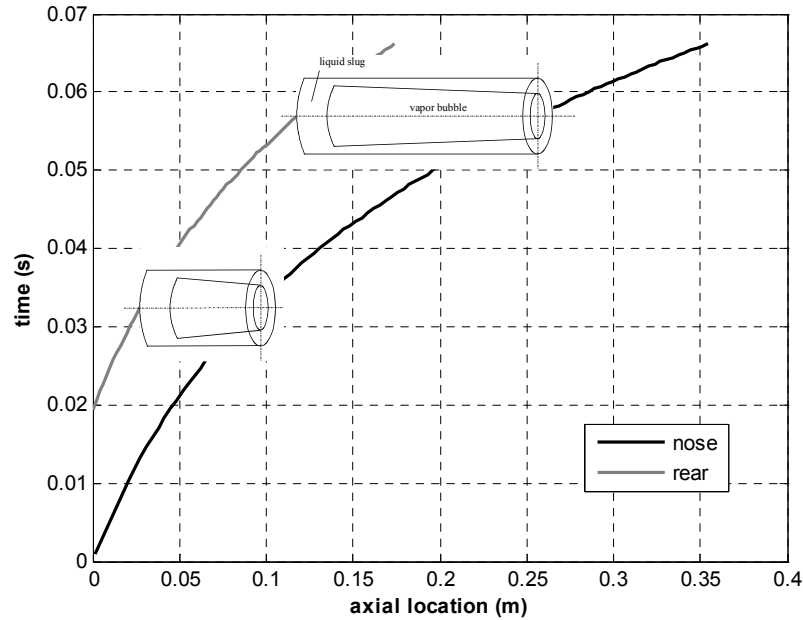


Figure 70. Bubble-slug nose and rear positions in time for R-134a in a 500 μ m channel, flowing with a mass velocity of 400kg/m²s and exposed to a wall heat flux of 25kW/m².

6.6 Local Heat Transfer Coefficients

The periodic nature of a slug flow will induce a cyclical variation in the local heat transfer coefficient. Assuming conductive heat transfer through the liquid film, the time-averaged heat transfer coefficient, α_v , over the residence of the elongated bubble is thus

$$\alpha_v(z) = \frac{1}{\Delta t_v} \int_{\Delta t_v} -\frac{k_l}{R} \frac{dt}{\ln\left(1 - \frac{\delta}{R}\right)} \quad (6.45)$$

For a thin film Eq. (6.45) reduces to

$$\alpha_v(z) \sim \frac{1}{\Delta t_v} \int_{t_N}^{t_T} \frac{k_l}{\delta} dt \quad (6.46)$$

where t_N and t_T are the times taken by the bubble nose and the bubble tail to reach location z . t_N is given by inverting Eq. (6.32),

$$t_N(z) = \frac{\rho_v h_{lv} R}{2q} \ln \left(1 + \frac{\rho_l}{\rho_v} \frac{2q}{G h_{lv}} \frac{z}{R} \right) \quad (6.47)$$

while t_T is simply, $t_T = t_N + \Delta t_v$. From the integral in Eq. (6.46), using Eq. (6.20) for δ ,

$$\alpha_v(z) = \frac{1}{\Delta t_v} \frac{\rho_l h_{lv} k_l}{q} \ln \left(\frac{1 - \frac{q}{2\rho_l h_{lv}} \frac{\tau_i}{\mu_l} \frac{t_N^2}{z}}{1 - \frac{q}{2\rho_l h_{lv}} \frac{\tau_i}{\mu_l} \frac{t_T^2}{z}} \right) \quad (6.48)$$

For the passage of the liquid slug, conventional single-phase flow theory yields a constant Nusselt number for a laminar flow, while for a turbulent flow of liquid the Dittus-Boelter correlation is deemed acceptable. Equation (6.25) shows that the local velocity of the liquid slug will increase during its passage due to the expansion from the evaporation process. The time-averaged velocity of the slug is given by the following mass balance

$$1 - x = \frac{1}{G \Delta t} \int_{\Delta t_1} \rho_l W_l dt = \frac{\rho_l \bar{W}_l \Delta t_1}{G \Delta t} \quad \text{thus} \quad \bar{W}_l = \frac{G(1-x)}{\rho_l} \frac{\Delta t}{\Delta t_1} \quad (6.49)$$

which then gives the Reynolds number of the slug as $Re_l = (\rho_l \bar{W}_l D) / \mu_l$. Interpolating the values of the Nusselt numbers for laminar and turbulent flows as was done in [12] to avoid jumps in Nu with Re_l , the time averaged value of the heat transfer coefficient for the liquid slug is (see Eq. (2.27))

$$\alpha_l(z) = \frac{k_l}{D} \left(Nu_{lam}^4 + Nu_{turb}^4 \right)^{1/4} \quad (6.50)$$

with $Nu_{lam} = 4.36$ and $Nu_{turb} = 0.023 Re_l^{0.8} Pr_l^{0.4}$. Equations (6.48) and (6.50) give the local time-averaged heat transfer coefficient as

$$\alpha(z) = \frac{1}{\Delta t} [\alpha_v(z) \Delta t_v(z) + \alpha_l(z) \Delta t_l(z)] \quad (6.51)$$

Figure 71 shows the predicted heat transfer coefficients for R-134a at 7bar, in a 500 μ m micro-channel, flowing at a mass velocity of 400kg/m²s. The values are plotted over a range of heat fluxes, and for vapor qualities where bubbly and slug flows are expected. At low heat fluxes the coefficients exhibit little change with vapor quality. As the heat flux rises, the slopes in the α - x plane become progressively steeper, with a more pronounced decrease in α with x . Figure 71 shows the change in the local heat transfer coefficient with heat flux. At a fixed vapor quality, the heat transfer coefficients behave asymptotically, reaching an upper limit at the highest values of q .

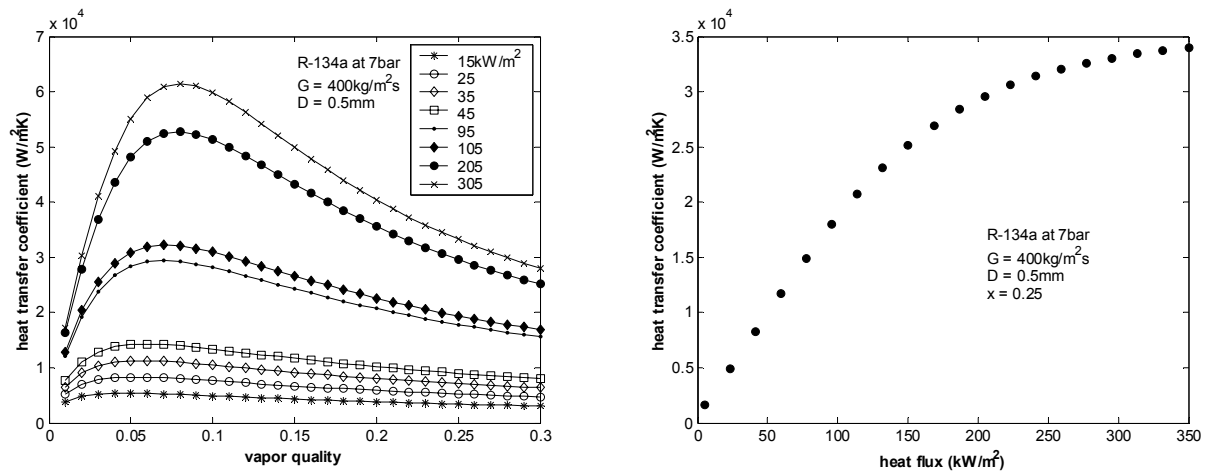


Figure 71. Predicted heat transfer coefficients for R-134a at 7bar, flowing with a mass velocity of 400kg/m²s in a 500μm channel.

The explanations behind these different trends lie in the effects of film thickness, liquid-vapor residence times, and liquid slug Nusselt numbers (see Eq. (6.51)), and must be analyzed individually. For the case of R-134a (see Fig. 72) at the conditions mentioned above, experiencing a heat flux of 35kW/m², the high vapor quality heat transfer coefficients are governed by conduction in the liquid film, since the residence time of the vapor phase is much higher than that of the liquid, and the values of α_v and α_l are of the same order. At the medium-low vapor qualities both mechanisms (liquid film conduction plus convection through the slugs) come into play. The descent in α_v that occurs over most of the vapor quality range, determines the negative slope in the total heat transfer coefficient (Figs. 71 and 72), and is due primarily to the increase in the time-averaged film thickness with z .

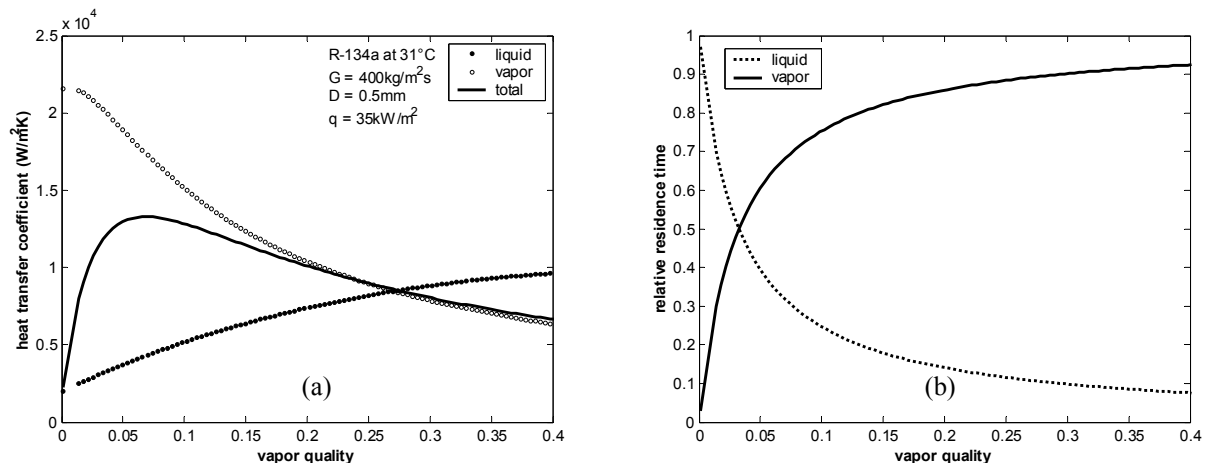


Figure 72. (a) Liquid, vapor and total heat transfer coefficient predictions for a slug flow of R-134a, and (b) the relative residence times of the two phases.

Figure 73 illustrates heat transfer coefficient predictions for R-236fa and R-245fa. In both cases the heat transfer coefficients have a similar behavior as those of R-134a. However, the magnitudes of the coefficients for R-245fa are the lowest, while those for R-236fa are at an intermediate level with respect to those for the other two fluids. The effect of fluid properties is best seen in Fig. 74a, which shows the average heat transfer coefficient (averaged along the channel length) for a single fluid, R-134a, at different saturation temperatures. The interfacial shear increases with T_{sat} , delivering thinner liquid films and higher heat transfer coefficients. Similarly, (see Fig. 74b) a reduction in the channel size also yields thinner films and higher values of α .

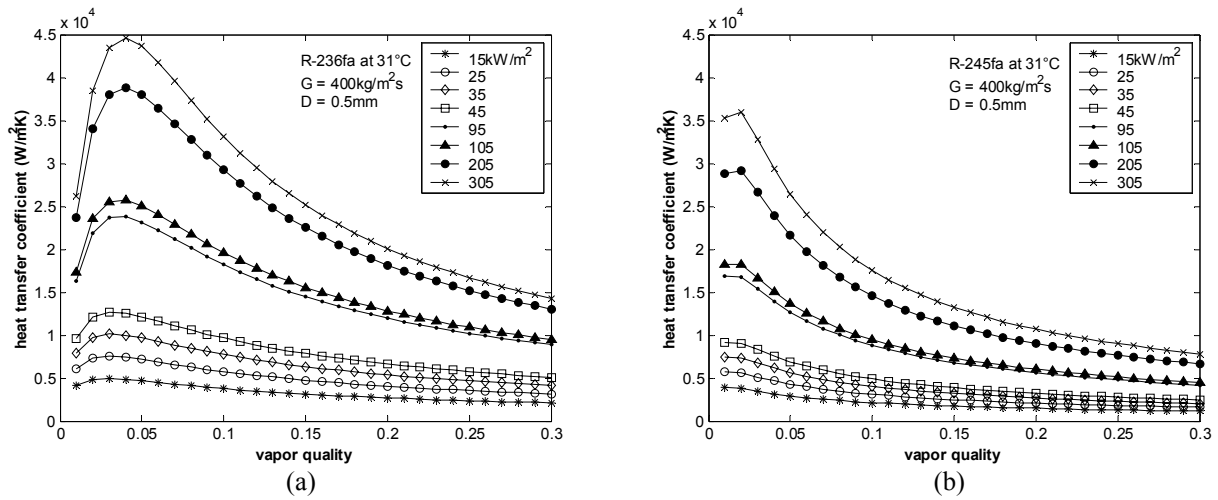


Figure 73. Heat transfer coefficients versus vapor quality over a range of heat fluxes for (a) R-236fa and (b) R-245fa at 31°C , flowing with a mass velocity of $400 \text{ kg/m}^2\text{s}$, in a $500 \mu\text{m}$ channel.

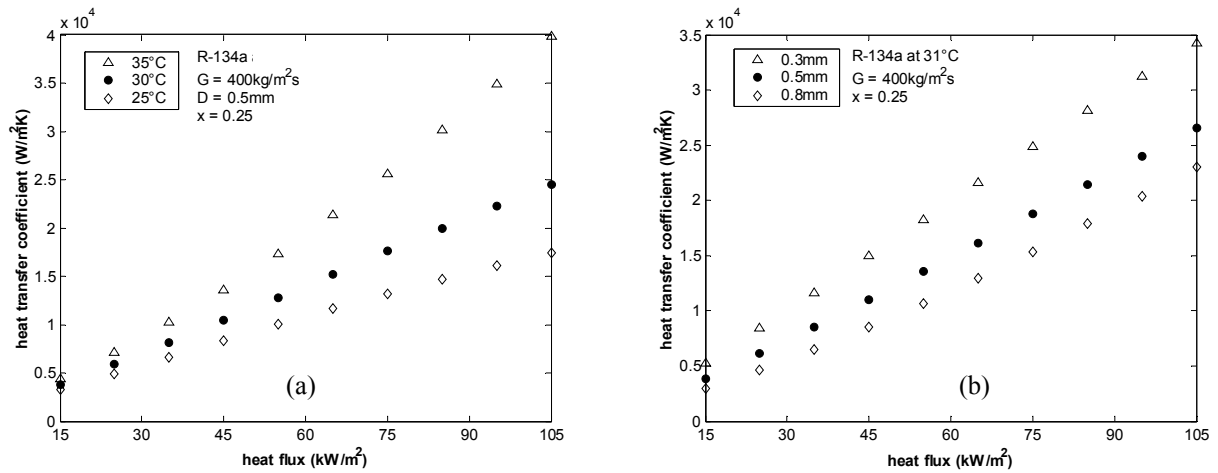


Figure 74. (a) Average heat transfer coefficients for R-134a at different saturation temperatures, and (b) average heat transfer coefficients for R-245fa in different diameter channels.

Figure 75 shows the change in the heat transfer coefficients with mass velocity. As confirmed experimentally, heat transfer is much less sensitive to mass velocity than to heat flux. Figure 75 does however exhibit a slight descent in α with G , which is again related to the development of the liquid film. From Eqs. (6.33) and (6.36), the bubble nose film thickness increases with mass velocity as $\delta_N \propto G^{0.17}$. A change in mass velocity, saturation temperature, or channel size modifies the heat transfer

coefficient of the liquid slug mainly at the higher vapor qualities (at higher degrees of turbulence), when, however, heat transfer is governed by thin film evaporation ($\Delta t_l \ll \Delta t_v$).

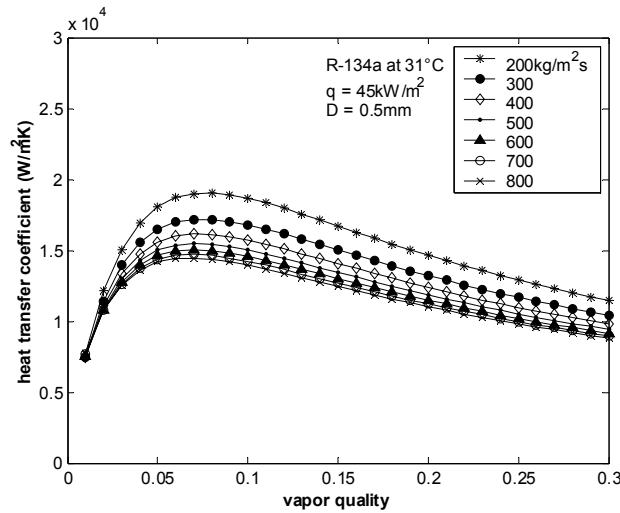


Figure 75. R-236fa heat transfer coefficients versus vapor quality, for different mass velocities.

6.7 Heat Transfer Predictions to the Experimental Data

Figures 76 and 77 illustrate a selection of individual sets of data, comparing them to the predicted heat transfer coefficients. Although partial success is achieved in the isolated bubble and coalescing bubble modes, with the predictions reproducing the general trends found in the experimental data (including the enhancement obtained through a reduction in channel size), the difference between the experimental results and the predictions is pronounced near the transition to annular flow (at the high-end vapor qualities of the ‘cb’ zones in Figs. 76 and 77). The simplifying assumptions made in order to solve the governing equations are the main reasons for the model shortcomings. For example, setting the interfacial shear to a constant value over the bubble length is certainly questionable. Furthermore, the change in pressure along the channel axis should be accounted for in the determination of the behavior of the thin film and the dynamics of the liquid slugs. The rounded bubble shapes that are observed experimentally, imply a higher pressure in the bubble with respect to the nearby liquid, and will induce a local difference in the properties of the liquid film with respect to those of the liquid slugs (which may also be superheated). The bubble nucleation scheme is another likely cause for error, since there is no apparent reason to assume only one nucleation site. Flow visualizations (see [17]) have shown numerous sites, with bubbles at times sliding along the channel wall before detachment. Finally, in a “coalescing bubble” flow mode, bubble coalescence will also affect the shape of the liquid film and thus the heat transfer coefficients.

Figure 78 compares the predictions to the data collected for the different fluids, and refers only to data classified as isolated bubble or coalescing bubble as defined in [19]. The predicted coefficients are computed at the local flow pressure. The best results are for R-134a, with 79% of the experimental values in the $\pm 30\%$ band. The success rate reduces to 60% for R-236fa, and reaches only 55% for R-245fa. The cumulative success rate is of 66% in the $\pm 30\%$ error band.

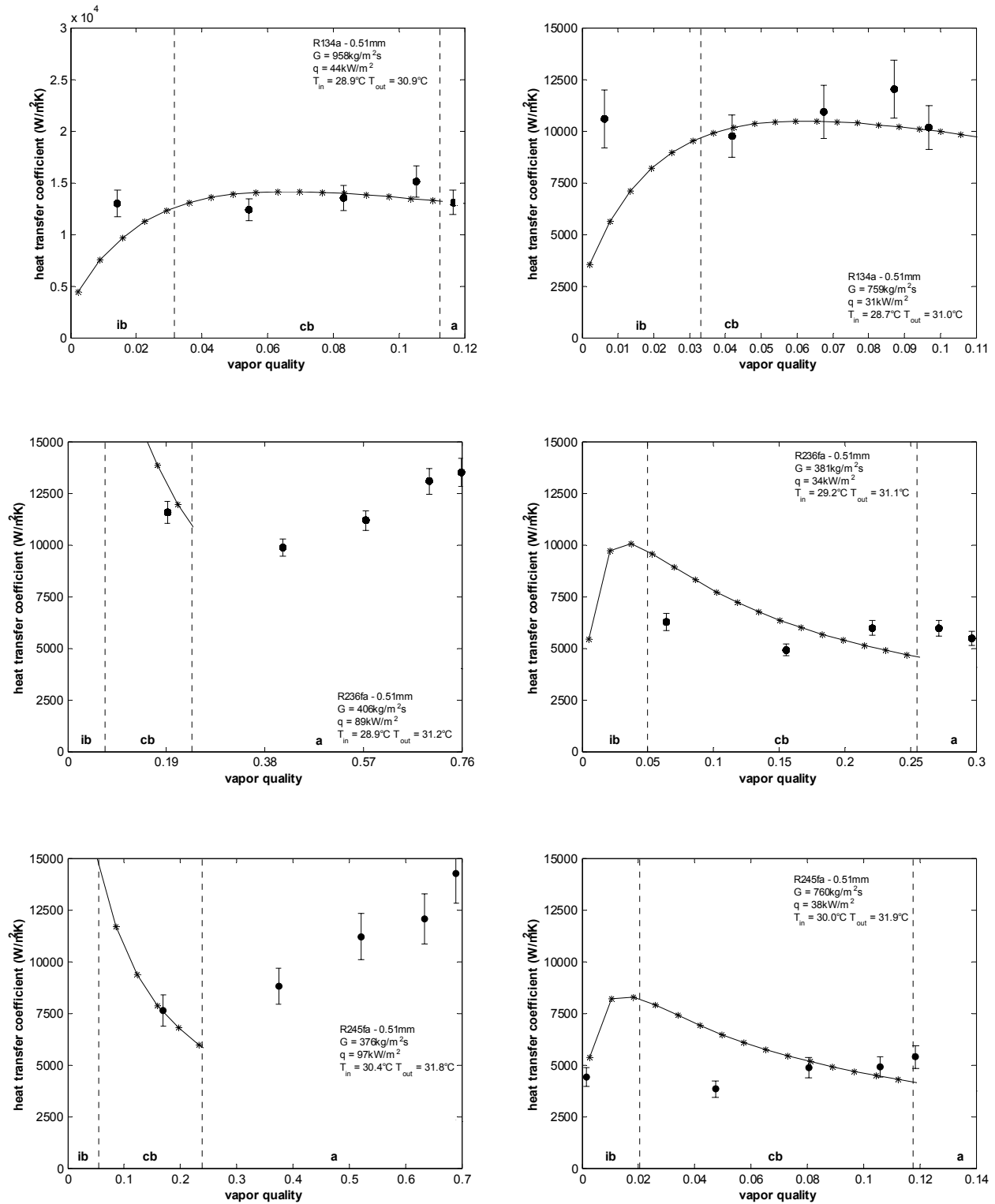


Figure 76. Heat transfer predictions compared to the experimental data for the 510 μm channel (ib – isolated bubble, cb – coalescing bubble, a – annular).

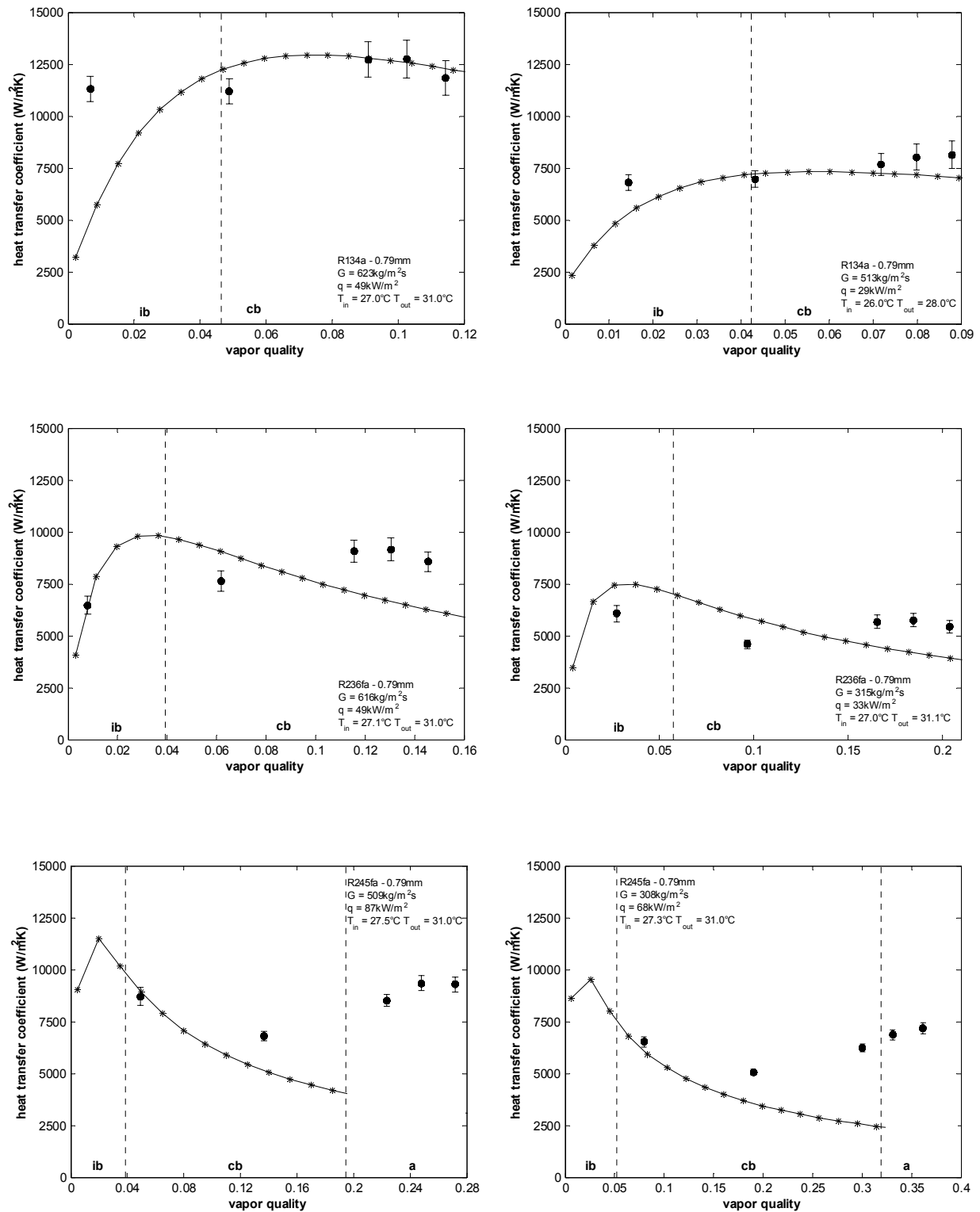


Figure 77. Heat transfer predictions compared to the experimental data for the 790 μm channel (ib – isolated bubble, cb – coalescing bubble, a – annular).

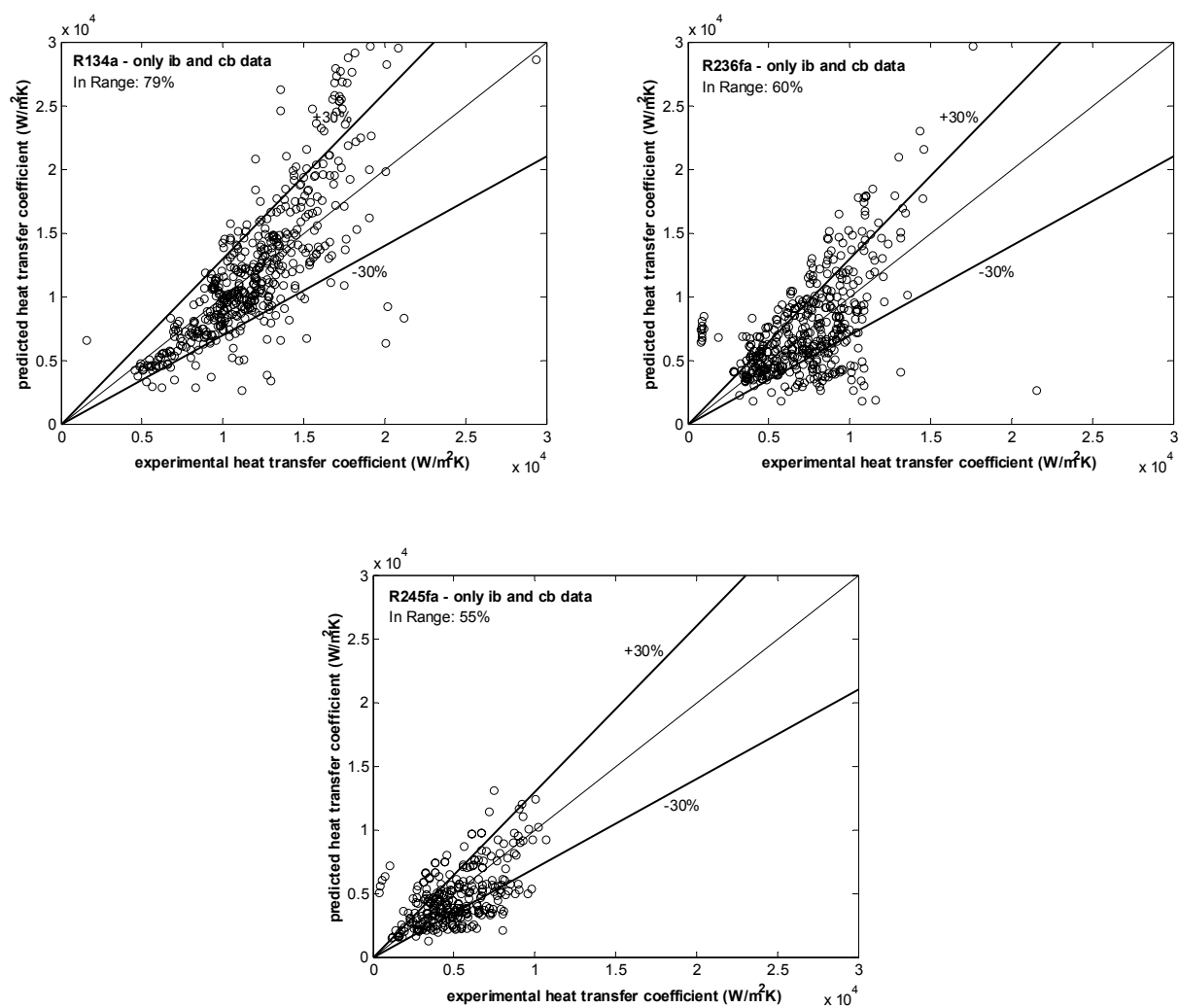


Figure 78. Comparison with of heat transfer predictions with the experimental data for isolated bubble and coalescing bubble flows.

Chapter 7

Conclusions

The flow boiling experiments performed in the current study have shown distinct heat transfer characteristics for stable and unstable two-phase micro-channel flows. The stable flow-boiling data have expressed the sensitivity of the heat transfer coefficients to the operating conditions, as well as to fluid properties. In particular, while the coefficients for R-134a and R-236fa have been shown to be mainly functions of heat flux and saturation conditions, R-245fa presents two different heat transfer zones: (1) at low and intermediate vapor qualities, where the flow experiences bubbly, slug, and churn flows, the low-pressure refrigerant behaves in the same way as the other two fluids; (2) at higher values of x , where the flow is mainly annular, its two-phase heat transfer coefficients are heat flux independent, and increase with quality.

The common heat transfer characteristics expressed by the three fluids have been analyzed from the point of view of a pure slug flow, which is the second dominant mode after annular flow for flow boiling in micro-channels. The current analysis reproduces to a certain extent the trends in the data, with the computed heat transfer coefficients increasing with heat flux and saturation temperature, decreasing with channel size, and remaining almost invariant with vapor quality at medium levels of heat flux. At higher degrees of heating, the predicted slopes of the curves in the α - x plane become progressively more negative, as confirmed experimentally. The suggested reason for these different behaviors lies in the development of the liquid film surrounding the elongated bubbles, with its local thickness governed by the extent of the vaporization process, and the magnitude of the drag force exchanged by the two phases. This last parameter assumes great importance in the estimation of α , and its value is extremely difficult to predict. An empirical correlation of the interfacial shear from the heat transfer data relates it not only to fluid properties and to the flow Reynolds number, but also to the rate of mass transfer at the interface, which is directly proportional to heat flux. The application of this form makes a pure slug flow consistent with both flow visualizations and heat transfer measurements. However, for high vapor quality annular flows, the question remains as to what justifies the differences mentioned above.

The sensitivity of evaporating micro-channel flows to compressible volume-type, dynamic instabilities has also been investigated experimentally. With respect to the stable case, which is associated to a high frequency bubble passage phenomenon that develops into annular flow, an unstable flow is often associated to low frequency-high amplitude oscillations in both flow and wall temperature, with cyclical ejection of liquid from the inlet of the evaporator. The different behaviors of unstable and stable flows are clearly visible from measured wall temperatures, and neglecting their presence in the data reduction process will yield substantial discrepancies in the results for those fluids, such as R-245fa, that in stable mode exhibit a change in heat transfer at the transition to annular flow.

As a final note on the design schemes for micro-channel evaporators, the current heat transfer prediction methods are either purely empirical, as in the case of the Lazarek-Black correlation [5], or are modified macro-scale correlations (Kandlikar-Balasubramanian [41] and Zhang *et al.* [42]) that identify in the laminar state of the liquid flow the main difference from conventional systems. For the present study, Lazarek and Black's expression proved remarkably successful in predicting the two-phase database, capturing the strong dependence of heat transfer on heat flux. The present analysis for slug flow, which extends from the three-zone model of Thome and coworkers [12], is an effort aimed at highlighting some of the most important physical aspects of these two-phase flows. This approach maintains the ambition to provide a reliable description of heat transfer in its applicable range of vapor

qualities, and represents the starting point for the description of churn flow, and of confined annular flow.

Appendix

Mathematical Description of a Compressible Volume Oscillatory Instability

Maulbetsch and Griffith [36] gave a mathematical description of compressible volume oscillatory instabilities. Their model, shown schematically in Fig. A-1, is based on the following assumptions:

1. The external system is characterized by the inlet and exit pressures seen by the heat exchanger. The exit pressure is considered to be constant, while the inlet pressure varies as an arbitrary function of the total flow rate; i.e. $p_{in} = p_{in}(Q)$.
2. The energy storage mechanism is assumed to be that of a compressible volume upstream of the test section.
3. The pressure drop across the heat exchanger section, $\Delta p_1(Q)$, includes all of the steady-state pressure drops between the compressible volume and the downstream, constant pressure plenum; i.e., the heated section as well as any valve, piping, sudden contractions and expansions, etc.
4. The model includes the effects of inertia in the test-section and in the fluid entering the compressible volume.
5. The flow resistance between the entrance plenum and the compressible volume is characterized by a “square-law” resistance ($\Delta p = KQ^2$).

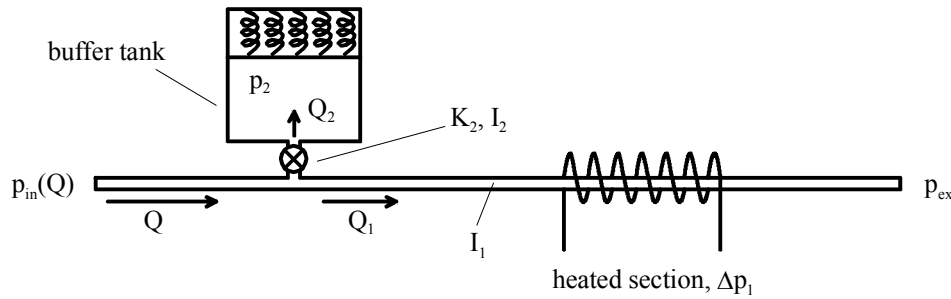


Figure A-1. Schematic of the model for the analysis of oscillatory instabilities, where subscript 1 refers to the flow through the heated length, while subscript 2 refers to the flow into the compressible volume.

The equations of motion are described below.

Flow through the Test-Section (Q_1)

The flow through the test-section is given by

$$p_{in} - p_{ex} = \Delta p_1(Q_1) + \left(\frac{\rho L}{A} \right) \frac{dQ_1}{dt} \quad (A.1)$$

Since p_{in} is a function of the total flow to the heat exchanger, this may be rewritten in terms of the inertial I_1 as

$$p_{in}(Q) - p_{ex} = \Delta p_1(Q_1) + I_1 \frac{dQ_1}{dt} \quad (A.2)$$

Flow to the Compressible Volume

The flow to the compressible volume is given by

$$p_{in}(Q) - p_2 = K_2 Q_2^2 + I_2 \frac{dQ_2}{dt}. \quad (A.3)$$

Definition of Inertia

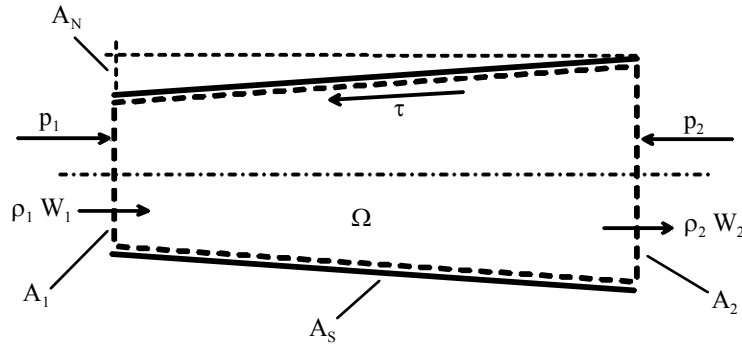


Figure A-2. Control volume for the definition of inertia.

The inertia terms are evaluated in the following way. If Newton's Second Law is applied to a control volume around a fluid flowing in a pipe, as in Fig. A-2, the resultant equation is

$$p_1 A_1 - p_2 A_2 + \int_0^L p dA_N - \tau A_S = \iiint_{\Omega} \frac{\partial}{\partial t} (\rho w) dV + (\rho A W^2)_2 - (\rho A W^2)_1 \quad (A.4)$$

For a constant area pipe, $A_1 = A_2$ and $A_N = 0$. Therefore, Eq. (A.4) reduces to

$$p_1 - p_2 - \left(\tau \frac{A_S}{A_1} + \rho_2 W_2^2 - \rho_1 W_1^2 \right) = \frac{1}{A_1} \iiint_{\Omega} \frac{\partial}{\partial t} (\rho w) dV \quad (A.5)$$

For nearly incompressible flow, $\rho = \text{constant}$ and $W_1 = W_2$. Hence,

$$p_1 - p_2 = \tau \frac{A_S}{A_1} + \frac{\rho}{A_1} \frac{d}{dt} (W A_1 L) \quad (A.6)$$

Defining $Q = WA$,

$$p_1 - p_2 = \tau \frac{A_s}{A_1} + \frac{\rho L}{A_1} \frac{dQ}{dt} \quad (\text{A.7})$$

In the steady-state $\tau A_s/A_1$ may be characterized as $\Delta p(Q)$ and

$$I \equiv \frac{\rho L}{A_1}$$

Pressure in Compressible Volume

As previously stated, the energy storage mechanism is characterized by a compressible volume upstream of the test-section. Therefore, if the initial pressure and volume are given by p_0 and V_0 , the pressure at any time may be expressed as

$$p_2 = p_0 + \left(\frac{dp}{dV} \right)_0 \Delta V \quad (\text{A.8})$$

The instantaneous volume may be computed by integrating the volume flow into the compressible volume over time; thus

$$\Delta V = - \int_0^t Q_2 dt \quad (\text{A.9})$$

Combining Eqs. (A.8) and (A.9) gives an expression for the pressure in the compressible volume at any time t , i.e.

$$p_2 = p_0 - \left(\frac{dp}{dV} \right)_0 \int_0^t Q_2 dt. \quad (\text{A.10})$$

Continuity Considerations

The continuity equation for the system, assuming an incompressible fluid is given simply by

$$Q = Q_1 + Q_2 \quad (\text{A.11})$$

Steady-State

The equations describing the steady-state behavior of the system are:

$$\begin{aligned} p_{in}(Q) - p_{ex} &= \Delta p_1(Q) \\ p_{in}(Q) - p_2 &= K_2 Q_2^2 \end{aligned} \quad (\text{A.12})$$

$$Q_2 = 0 \quad Q = Q_1 \quad p_2 = p_0$$

Manipulation of the preceding equations yields the following description of the system:

$$p_{in}(Q) - p_{ex} = \Delta p_1(Q_1) + I_1 \frac{dQ_1}{dt} \quad (A.13)$$

$$p_{in}(Q) - p_0 + \left(\frac{dp}{dV} \right)_0 \int_0^t Q_2 dt = K_2 Q_2^2 + I_2 \frac{dQ_2}{dt} \quad (A.14)$$

Small Perturbation Solution

The equations may now be written for small perturbations around a steady-state flow:

$$Q = Q_0 + \Delta Q \quad \text{and} \quad Q_1 = Q_0 + \Delta Q_1 \quad (A.15)$$

From Eq. (A.11), this becomes

$$Q_2 = \Delta Q - \Delta Q_1 \quad (A.16)$$

In conjunction with the small perturbation assumption, Eq. (A.10) may be written as

$$p_2 = p_0 - \left(\frac{dp}{dV} \right)_0 \int_0^t (\Delta Q - \Delta Q_1) dt \quad (A.17)$$

Equations (A.13) and (A.14) now become

$$p_{in}(Q_0) + \frac{dp_{in}}{dQ} \Delta Q - p_{ex} = \Delta p_1(Q_0) + \frac{d(\Delta p_1)}{dQ} \Delta Q_1 + I_1 \frac{d}{dt} (Q_0 + \Delta Q_1) \quad (A.18)$$

$$p_{in}(Q_0) + \frac{dp_{in}}{dQ} \Delta Q - p_0 + \left(\frac{dp}{dV} \right)_0 \int_0^t Q_2 dt = K_2 Q_2^2 + I_2 \frac{dQ_2}{dt} \quad (A.19)$$

Subtracting out the steady-state terms and retaining only the first power terms ΔQ , ΔQ_1 , and Q_2 yields,

$$\frac{dp_{in}}{dQ} \Delta Q = \frac{d(\Delta p_1)}{dQ} \Delta Q_1 + I_1 \frac{d}{dt} (\Delta Q_1) \quad (A.20)$$

$$\frac{dp_{in}}{dQ} \Delta Q + \left(\frac{dp}{dV} \right)_0 \int_0^t (\Delta Q - \Delta Q_1) dt = I_2 \frac{dQ_2}{dt} \quad (A.21)$$

Eliminating Q_2 through the use of Eq. (A.16) gives

$$\frac{dp_{in}}{dQ} \Delta Q = \frac{d(\Delta p_1)}{dQ} \Delta Q_1 + I_1 \frac{d}{dt} (\Delta Q_1) \quad (A.22)$$

$$\frac{dp_{in}}{dQ} \Delta Q + \left(\frac{dp}{dV} \right)_0 \left(\int_0^t \Delta Q dt - \int_0^t \Delta Q_1 dt \right) = I_2 \left[\frac{d}{dt} (\Delta Q) - \frac{d}{dt} (\Delta Q_1) \right] \quad (A.23)$$

Performing a Laplace transform on this system of equations where

$$\Delta\tilde{Q} \equiv L(\Delta Q) \equiv \int_0^\infty \exp(-s t) \Delta Q dt \quad \text{and} \quad \Delta\tilde{Q}_1 \equiv L(\Delta Q_1) \equiv \int_0^\infty \exp(-s t) \Delta Q_1 dt$$

the following set of transformed equations is obtained:

$$\frac{dp_{in}}{dQ} \Delta\tilde{Q} = \frac{d(\Delta p_1)}{dQ} \Delta\tilde{Q}_1 + I_1 s \Delta\tilde{Q}_1 \quad (\text{A.24})$$

$$\frac{dp_{in}}{dQ} \Delta\tilde{Q} + \left(\frac{dp}{dV} \right)_0 \frac{1}{s} (\Delta\tilde{Q} - \Delta\tilde{Q}_1) = I_2 s (\Delta\tilde{Q} - \Delta\tilde{Q}_1) \quad (\text{A.25})$$

Eliminating $\Delta\tilde{Q}$ leads to the following characteristic polynomial equation in the Laplace variable, s :

$$\frac{dp_{in}}{dQ} \left[\frac{\frac{d(\Delta p_1)}{dQ} + s I_1}{\frac{dp_{in}}{dQ}} \right] + \left(\frac{dp}{dV} \right)_0 \frac{1}{s} \left[\frac{\frac{d(\Delta p_1)}{dQ} + s I_1}{\frac{dp_{in}}{dQ}} - 1 \right] = I_2 s \left[\frac{\frac{d(\Delta p_1)}{dQ} + s I_1}{\frac{dp_{in}}{dQ}} - 1 \right] \quad (\text{A.26})$$

Rearranging yields

$$\begin{aligned} s^3 \left[\frac{I_1 I_2}{\frac{dp_{in}}{dQ}} \right] + s^2 \left[I_2 \left(\frac{\frac{d(\Delta p_1)}{dQ} + s I_1}{\frac{dp_{in}}{dQ}} - 1 \right) - I_2 \right] + s \left[-\frac{d(\Delta p_1)}{dQ} - \left(\frac{dp}{dV} \right)_0 \frac{I_1}{\frac{dp_{in}}{dQ}} \right] + \\ + \left[-\left(\frac{dp}{dV} \right)_0 \left(\frac{\frac{d(\Delta p_1)}{dQ}}{\frac{dp_{in}}{dQ}} - 1 \right) \right] = 0 \end{aligned} \quad (\text{A.27})$$

The case for marginal stability may be investigated in the following way. For a third order expression of the form

$$as^3 + bs^2 + cs + d = 0$$

marginal stability will result when $s = i\omega$. This yields

$$-a i \omega^3 - b \omega^2 + c i \omega + d = 0$$

and implies the conditions that

$$\omega^2 = \frac{d}{b} \quad \text{and} \quad \frac{c}{a} = \frac{d}{b}$$

Setting $c/a = d/b$ determines the value of $d(\Delta p_1)/dQ$ which will result in a marginally stable system for any arbitrary external characteristic, dp_{in}/dQ . Performing this operation results in,

$$\frac{d(\Delta p_1)}{dQ} = \frac{\frac{dp_{in}}{dQ}(I_1 + I_2) \pm \sqrt{\left(\frac{dp_{in}}{dQ}\right)^2 (I_1 + I_2)^2 + 4I_1^2 I_2 \left(\frac{dp}{dV}\right)_0}}{2I_2} \quad (A.28)$$

Of the two solutions only the + sign solution is of interest, since it will always occur first in any real system. With this result, the frequency is given by

$$\omega^2 = \frac{d}{b} = \frac{1}{2I_1 I_2^2} \left[-\left(\frac{dp_{in}}{dQ}\right)^2 (I_1 + I_2)^2 + \right. \\ \left. -\left(\frac{dp_{in}}{dQ}\right) \sqrt{\left(\frac{dp_{in}}{dQ}\right)^2 (I_1 + I_2)^2 + 4I_1^2 I_2 \left(\frac{dp}{dV}\right)_0} - 2I_1 I_2 \left(\frac{dp}{dV}\right)_0 \right] \quad (A.29)$$

Cited Literature

- [1] Suo, M., and Griffith, P., Two-Phase Flow in Capillary Tubes, *J. Basic Eng.*, vol. 86, pp. 576-582, 1964.
- [2] Kew, P. A., and Cornwell, K., Correlations for the Prediction of Boiling Heat Transfer in Small-Diameter Channels, *Applied Thermal Engineering*, vol. 17, pp. 705-715, 1997.
- [3] Brauner, N., and Moalem-Maron, D., Identification of the Range of Small Diameter Conduits, Regarding Two-Phase Flow Pattern Transition, *Int. Comm. Heat and Mass Transfer*, vol. 19, pp. 29-39, 1992.
- [4] Ribatski, G., Wojtan, L., and Thome, J. R., An Analysis of Experimental Data and Prediction Methods for Two-Phase Frictional Pressure Drop and Flow Boiling Heat Transfer in Micro-Scale Channels, *Experimental Thermal and Fluid Science*, vol. 31, pp. 1-19, 2006.
- [5] Lazarek, G. M., and Black, S. H., Evaporative Heat Transfer, Pressure Drop and Critical Heat Flux in a Small Vertical Tube with R-113, *Int. J. Heat and Mass Transfer*, vol. 25 (7), pp. 945-960, 1982.
- [6] Agostini, B., and Thome, J. R., Comparison of an Extended Database for Flow Boiling heat transfer Coefficients in Multi-Microchannel Elements with the Three-Zone Model, *ECI Heat Transfer and Fluid Flow in Microscale*, Castelvechio Pascoli, Italy, Sept. 25-30, 2005.
- [7] Tripplett, K. A., Ghiaasiaan, S. M., Abdel-Khalik, S. I., and Sadowski, D. L., Gas-Liquid Two-Phase Flow in Micro-Channels Part I: Two-Phase Flow Patterns, *Int. J. Multiphase Flow*, vol. 25, pp. 377-394, 1999.
- [8] Serizawa, A., Feng, Z., and Kawara, Z., Two-Phase Flow in Microchannels, *Experimental Thermal and Fluid Science*, vol. 26, pp. 703-714, 2002.
- [9] Revellin, R., Dupont, V., Thome, J.R. and Zun, I., Characterization of Diabatic Two-Phase Flows in Micro-Channels: Flow Parameter Results for R-134a in a 0.5mm Channel, *Int. J. Multiphase Flow*, vol. 32, pp. 755-774, 2006.
- [10] Cornwell, K., and Kew, P. A., Boiling in Small Parallel Channels, *Energy Efficiency in Process Technology*, Elsevier Applied Science, London, pp. 624-638, 1993.
- [11] Jacobi, A. M., and Thome, J. R., Heat Transfer Model for Evaporation of Elongated Bubble Flows in Microchannels, *Journal of Heat Transfer*, vol. 124, pp. 1131-1136, 2002.
- [12] Thome, J. R., Dupont, V., and Jacobi, A. M., Heat Transfer Model for Evaporation in Microchannels. Part I: presentation of the model, *Int. J. Heat and Mass Transfer*, vol. 47, pp. 3375-3385, 2004.
- [13] Kandlikar, S. G., Heat Transfer Mechanisms During Flow Boiling in Microchannels, *Journal of Heat Transfer*, vol. 126, pp. 8-16, 2004.
- [14] Bergles, A. E., and Kandlikar, S. G., On the Nature of Critical Heat Flux in Microchannels, *Journal of Heat Transfer*, vol. 127, pp. 101-107, 2005.

-
- [15] Liu, D., Lee, P. S., and Garimella, S. V., Prediction of the Onset of Nucleate Boiling in Micro-Channel Flow, *Int. J. Heat and Mass Transfer*, vol. 48, pp. 5134-5149, 2005.
- [16] Kandlikar, S. G., Nucleation Characteristics and Stability Considerations During Flow Boiling in Micro-Channels, *Experimental Thermal and Fluid Science*, vol. 30, pp. 441-447, 2006.
- [17] Lee, P. C., Tseng, F. G., and Pan C., Bubble Dynamics in Micro-Channels. Part I: Single Micro-Channel, *Int. J. Heat and Mass Transfer*, vol. 47, pp. 5575-5589, 2004.
- [18] Li, J., and Peterson, G. P., Boiling Nucleation and Two-Phase Flow Patterns in Forced Liquid Flow in Micro-Channels, *Int. J. Heat and Mass Transfer*, vol. 48, pp. 4797-4810, 2005.
- [19] Revellin, R., and Thome, J.R., New Diabatic Flow Pattern Map for Evaporating Flows in Microchannels, *13th International Heat Transfer Conference*, Sydney, August 14-18, 2006.
- [20] Chung P.M.-Y., and Kawaji M., The Effect of Channel Diameter on Adiabatic Two-Phase Flow Characteristics in Micro-Channels, *Int. J. Multiphase Flow*, vol. 30, pp. 735-761, 2004.
- [21] Zhao, T. S., and Bi, Q. C., Co-Current Air-Water Two-Phase Flow Patterns in Vertical Triangular Micro-Channels, *Int. J. Multiphase Flow*, vol. 27, pp. 765-782, 2001.
- [22] Cubaud T., and Chih-Ming, H., Transport of Bubbles in Square Micro-Channels, *Physics of Fluids*, vol. 16 (12), pp. 4575-4585, 2004.
- [23] Lin, S, Kew, P. A., and Cornwell, K., Two-Phase Heat Transfer to a Refrigerant in a 1mm Diameter Tube, *Int. J. Refrigeration*, vol. 24, pp. 51-56, 2001.
- [24] Owhaib, W., Palm, B., and Martín-Callizo C., Flow Boiling Visualizations in a Vertical Circular Mini-Channel at High Vapor Quality, *Experimental Thermal and Fluid Science*, vol. 30, pp. 755-763, 2006.
- [25] Tran, T. N., Wambsganss, M. W., and France, D. M., Small Circular- and Rectangular-Channel Boiling with Two Refrigerants, *Int. J. Multiphase Flow*, vol. 22, no. 3, pp. 485-498, 1996.
- [26] Bao, Z. Y., Fletcher, D. F., and Haynes, B. S., Flow Boiling Heat Transfer of Freon R11 and HCFC123 in Narrow Passages, *Int. J. Heat and Mass Transfer*, vol. 43, pp. 3347-3358, 2000.
- [27] Lihong, W., Min, C., and Groll, M., Experimental Study of Flow Boiling Heat Transfer in Mini-Tube, *ICMM2005*, 2005.
- [28] Saitoh, S., Daiguji, H., and Hihara, E., Effect of Tube Diameter on Boiling Heat Transfer of R-134a in Horizontal Small-Diameter Tubes, *Int. J. Heat and Mass Transfer*, vol. 48, pp. 4973-4984, 2005.
- [29] Sumith, B., Kaminaga, F., and Matsumura, K., Saturated Flow Boiling of Water in a Vertical Small Diameter Tube, *Experimental Thermal and Fluid Science*, vol. 27, pp. 789-801, 2003.
- [30] Xu, J., Shen, S., Gan, Y., Li, Y., Zhang, W., and Su, Q., Transient Flow Pattern Based Microscale Boiling Heat Transfer Mechanisms, *J. Micromech. Microeng.*, vol. 15, pp. 1344-1361, 2005.

-
- [31] Yan, Y., and Lin, T., Evaporation Heat Transfer and Pressure Drop of Refrigerant R-134a in a Small Pipe, *Int. J. Heat and Mass Transfer*, vol. 41, pp. 4183-4194, 1998.
- [32] Lee, J., and Mudawar, I., Two-Phase Flow in High-Heat-Flux Microchannel for Refrigeration Cooling Applications: Part II – Heat Transfer Characteristics, *Int. J. Heat and Mass Transfer*, vol. 48, pp. 941-955, 2005.
- [33] Agostini, B., and Bontemps, A., Vertical Flow Boiling of Refrigerant R134a in Small Channels, *Int. J. Heat and Fluid Flow*, vol. 26, pp. 296-306, 2005.
- [34] Pettersen, J., Flow Vaporization of CO₂ in Microchannel Tubes, *Experimental Thermal and Fluid Science*, vol. 28, pp. 111-121, 2004.
- [35] Qu, W., and Mudawar, I., Measurement and Correlation of Critical Heat Flux in Two-Phase Micro-channel Heat Sinks, *Int. J. Heat and Mass Transfer*, vol. 47, pp. 2045-2059, 2004.
- [36] Maulbetsch, J. S., and Griffith, P., A Study of System-Induced Instabilities in Forced-Convection Flows with Subcooled Boiling, Air Force Contract AF 49(638)-1468, Report No. 5382-35, April 1965.
- [37] Hetsroni, G., Mosyak, A., Pogrebnyak, E., and Segal, Z., Explosive Boiling of Water in Parallel Micro-Channels, *Int. J. Multiphase Flow*, vol. 31, pp. 371-392, 2005.
- [38] Kenning, D. B. R., and Yan, Y., Saturated Flow Boiling of Water in a Narrow Channel: Experimental Investigation of Local Phenomena, *Trans IChem*, vol. 79, part A, pp. 425-436, 2001.
- [39] Brutin, D., Topin, F., and Tadrist, L., Experimental Study of Unsteady Convective Boiling in Heated Minichannels, *Int. J. Heat and Mass Transfer*, vol. 46, pp. 2957-2965, 2003.
- [40] Cortina Díaz, M., and Schmidt, J., Experimental Investigation of Transient Boiling Heat Transfer in Micro-Channels, *Int. J. Heat and Fluid Flow*, vol. 28, pp. 95-102, 2007.
- [41] Kandlikar, S. G., and Balasubramanian, P., An Extension of the Flow Boiling Correlation to Transition, Laminar, and Deep Laminar Flows in Mini-Channels and Micro-Channels, *Heat Transfer Engineering*, vol. 25 (3), pp. 86-93, 2004.
- [42] Zhang, W., Hibiki, T., and Mishima, K., Correlation for Flow Boiling Heat Transfer in Mini-Channels, *Int. J. Heat and Mass Transfer*, vol. 47, pp. 5749-5763, 2004.
- [43] Churchill, W. C., and Chu, H. H. S., Correlating Equations for Laminar and Turbulent Free Convection from a Horizontal Cylinder, *Int. J. Heat and Mass Transfer*, vol. 18, pp. 1049-1053, 1975.
- [44] Celata, G. P., Preface to the Special Issue dedicated to the ECI International Conference on Heat Transfer and Fluid Flow in Microscale, *Experimental Thermal and Fluid Science*, Castelveccchio Pascoli, Italy, 25-30 September 2005.
- [45] Shiferaw, D., Huo, X., Karayiannis, T. G., Kenning, D. B. R., Examination of Heat Transfer Correlations and a Model for Flow Boiling of R-134a in Small Diameter Tubes, *Int. J. Heat and Mass Transfer* (2007), doi:10.1016/j.ijheatmasstransfer.2007.07.002.

Vitae

Personal Information

Name: **Lorenzo CONSOLINI**
Date of Birth: 22-01-1976
Birthplace: Rome, Italy
Nationality: Italy - USA

Education

Laurea di Dottore in Ingegneria Meccanica. Università degli Studi di Roma "Tor Vergata". Rome, Italy.

MS in Mechanical Engineering. University of Illinois at Chicago. Chicago (IL), USA.

Master in Thermal Science and Fluid Mechanics. Università degli Studi di Roma "Tor Vergata". Rome, Italy.

PhD in Mechanical Engineering. École Polytechnique Fédérale de Lausanne. Lausanne, Switzerland.

Work Experience

Doctoral Research Assistant. Heat and Mass Transfer Laboratory. École Polytechnique Fédérale de Lausanne. Lausanne, Switzerland.

Graduate Research Assistant. University of Illinois at Chicago. Chicago (IL), USA.

Internship. General Electric Aircraft Engines. Evendale (OH), USA.

Publications

Consolini L., Aggarwal S.K., and Murad S., A molecular dynamics simulation of droplet evaporation, *International Journal of Heat and Mass Transfer*, vol. 46(17), pp. 3179-3188, 2003.

Consolini L., Robinson D., and Thome J.R., Void fraction and two-phase pressure drops for evaporating flow over horizontal tube bundles, *Heat Transfer Engineering*, vol. 27(3), pp. 5-21, 2006.

Consolini L., Ribatski G., Zhang W., Xu J., and Thome J.R., Heat transfer in confined forced flow boiling, *Heat Transfer Engineering*, vol. 28(9), 2007.

Ribatski G., Zhang W., Consolini L., Xu J., and Thome J.R., On the prediction of heat transfer in micro-scale flow boiling, *Heat Transfer Engineering*, vol. 28(9), 2007.